WARSAW UNIVERSITY OF TECHNOLOGY

DISCIPLINE OF SCIENCE NATURAL SCIENCES
FIELD OF SCIENCE PHYSICAL SCIENCES

Ph.D. Thesis

Aniela Czudek, M.Sc.

Impact of alkali element doping on the electrical characteristics of Cu(In,Ga)Se_2 solar cells and thin films

Supervisor
Professor Małgorzata Igalson, Ph.D.
Co-supervisor
Aleksander Urbaniak, Ph.D.

WARSAW 2023

Acknowledgements

This work would not be possible without the help of many people – in fact, too many to fit in the limited space of acknowledgements.

I would like to thank my supervisor, professor Małgorzata Igalson, for the scientific guidance and many lengthy and sometimes heated scientific discussions. It was an honor and pleasure to work together. I would also like to thank for the patience and pushing me forward when I was doubting my abilities.

I would like to thank dr. Aleksander Urbaniak for his help with the intricacies of the measurement techniques and setups, and for keeping the atmosphere in the lab open and welcoming. The same goes to the rest of our group – Kuba, Marek, Konrad, Paweł, Jerzy, Przemek D., Ania, and everyone else who over the years dropped by the 3rd floor. Professor Marzantowicz and dr. Możaryn should also be mentioned here for their support in the everyday academic life.

Special thanks are directed to professor Roland Wuerz and (now dr.) Alexander Eslam from the Zentrum für Solarenergie und Wasserstoffforschung in Stuttgart. The contents of this work were made as a part of joint Alka-CIGS project, and all of the devices shown here, as well as SIMS measurements were prepared by them and their group. I look fondly to the many discussions we had during the project, even though most of those unfortunately had to be online.

Finally I want to thank the people close to me, who were there for me during these 5.5 years – my Mother, for raising me to be the person I am now and, together with my Father, showing me the beauty of nature and science when I was still a child. My partner Janek, for his kindness and patience and my friends: Przemek, Mariola, Bruno, Konrad, Damian…

Thank you

Streszczenie

Ogniwa fotowoltaiczne oparte o $Cu(In,Ga)Se_2$ są jednymi z najpopularniejszych cienkowarstwowych ogniw fotowoltaicznych od czasu ich wynalezienia w latach siedemdziesiątych XX w. i wprowadzenia na rynek przez Arco Solar w 1998 roku. Jeden z głównych skoków w ich rozwojów miał miejsce we wczesnych latach dziewięćdziesiątych, gdy tanie szkło sodowe zostało użyte zamiast podłoży opartych o szkło borokrzemianowe. Dyfuzja sodu z podłoża wpłynęła na poprawę sprawności, przede wszystkim poprzez zwiększenie napięcia otwartego obwodu V_{OC} i współczynnika wypełnienia FF. Od tego czasu także inne metale alkaliczne, takie jak potas, rubid czy cez są z sukcesem wykorzystywane do poprawiania sprawności ogniw CIGS. Mimo tego, iż wszystkie obecnie dostępne na rynku ogniwa CIGS są domieszkowane sodem, dokładny mechanizm jego działania nadal jest dyskutowany. Jak dotąd większość badań eksperymentalnych była skoncentrowana na porównaniu ogniw i cienkich warstw pozbawionych domieszek oraz z ich dodatkiem, czasami z użyciem różnych metali alkalicznych albo metod ich wprowadzania do absorbera. Bardzo niewiele danych literaturowych jest związana z badaniem wpływu koncentracji domieszek na parametry ogniw. Aby lepiej zrozumieć mechanizm wpływu domieszkowania metalami alkalicznymi warto jest przyjrzeć się możliwie szerokiemu zakresowi koncentracji sodu/potasu na różnego rodzaju próbkach, wliczając w to zarówno ogniwa jak i cienkie warstwy.

Kolejnym ciekawym aspektem ogniw CIGS jest metatrwałe fotoprzewodnictwo (PPC) – zwiększenie przewodności oraz gęstości swobodnych nośników (i w konsekwencji, sprawności) po oświetleniu, które pozostaje także o wyłączeniu źródła światła, o ile temperatura jest wystarczająco niska. Znowu, ten efekt był w większości badany co najwyżej na parach bez- oraz z domieszką metali alkalicznych.

W tej pracy przedstawione jest przekrojowe badanie wpływu koncentracji sodu oraz potasu na zrelaksowane oraz metastabilne parametry pojemnościowe oraz elektryczne próbek CIGS. Głównymi próbkami w tej pracy były cienkie warstwy oraz kompletne ogniwa wytworzone za pomocą jednoetapowego procesu naparowywania, charakteryzujące się jednorodną morfologią oraz stechiometrią. Dla głębszego wglądu w mechanizmy domieszkowania zbadane zostały także warstwy oraz ogniwa o większych ziarnach sporządzone przy pomocy trójetapowego procesu, stosowanego powszechnie w przemyśle. Domieszkowanie sodem i potasem zostało przeprowadzone za pomocą post-deposition treatment (PDT), aby ograniczyć wpływ

domieszek na morfologię próbek[1]. Koncentracja sodu i potasu była regulowana za pomocą doboru temperatury wygrzewania. Na cienkich warstwach przeprowadzone zostały pomiary przewodności w funkcji temperatury w stanie zrelaksowanym oraz metastabilnym. W ogniwach koncentracja swobodnych nośników została wyznaczona za pomocą Drive Level Capacitance Profiling, także w dwóch stanach. Porównanie pomiędzy wynikami dla ogniw oraz cienkich warstw pozwala na odróżnienie efektów związanych z interfejsami oraz z absorberem.

W cienkich warstwach, dodatek sodu skutkuje zależnym od jego koncentracji zwiększeniem przewodności oraz zmniejszeniem energii aktywacji zbocza σ(T). Potas powoduje niemalże takie same zmiany, tylko mniej więcej 4x więcej potasu niż sodu potrzebne jest do uzyskania tego samego efektu. Jedyną jakościową różnicą było radykalne zmniejszenie przewodności w próbkach domieszkowanych niewielkimi ilościami potasu, prawdopodobnie z powodu powstawania dodatkowych barier w niskich temperaturach wygrzewania. Taka sama zależność od koncentracji sodu oraz potasu, zarówno w przypadku materiału pochodzącego z jedno- oraz trójetapowego procesu, była widoczna w przypadku koncentracji swobodnych dziur w ogniwach, w tą różnicą, że na każdy rząd wielkości zmiany w koncentracji dziur przypadają dwa rzędy wielkości zmiany przewodności. Wszystkie te fakty świadczą o tym, że pozytywny efekt metali alkalicznych nie zależy od rodzaju pierwiastka, ma swoje źródło we wnętrzu absorbera a nie na interfejsach, oraz wpływa zarówno na koncentrację nośników jak i ich ruchliwość.

Taka sama zależność od koncentracji sodu i potasu zaobserwowana została także dla metatrwałego fotoprzewodnictwa. Jedną z ciekawych obserwacji jest to, że poprzez wiele rzędów wielkości (także dla próbek z niską zawartością potasu) obserwowana jest proporcjonalność PPC do zrelaksowanej wartości przewodnictwa. Fakt ten mocno podkreśla, że ten sam czynnik wpływa na PPC oraz na zrelaksowane parametry elektryczne.

Wpływ domieszkowania metalami alkalicznymi na absorber CIGS może być wytłumaczony za pomocą modelu pasywacji defektów na granicach ziaren. Bariery na granicach ziaren związane z obecnością defektów wpływałyby zarówno na ruchliwość jak też koncentrację nośników poprzez powstawanie warstw zubożonych we wnętrzu ziaren w pobliżu ich powierzchni. Ten

[1] Całośc wykonania próbek, domieszkowanie metalami alkalicznymi oraz charakteryzacja składu próbek, w tym koncentracji sodu i potasu, wykonana została przez prof. Rolanda Wuerza oraz Alexandra Eslama w Zentrum für Solarenergie und Wasserstoffforschung (ZSW) w Stuttgarcie.

model został porównany z danymi eksperymentalnymi i pomimo jego prostoty osiągnięta została dobra zgodność symulacji z eksperymentem. Tak więc głównym wnioskiem z pracy jest stwierdzenie, że dominującym czynnikiem przyczyniającym się do wzrostu wydajności ogniw fotowoltaicznych w wyniku domieszkowania metalami alkalicznymi jest pasywacja granic ziaren. Inne efekty, takie jak domieszkowanie wnętrza ziaren, chociaż nie są wykluczone, mają prawdopodobnie mniej znaczący wpływ.

Słowa kluczowe: $Cu(In,Ga)Se_2$, ogniwa fotowoltaiczne, granice ziaren

Abstract

Solar cells based on Cu(In,Ga)Se_2 have been one of the most prominent types of thin-films solar cells since their first development in the 1970's and their subsequent introduction into commercial manufacture in 1998 by Arco Solar. One of the greatest leaps in their development took place in the early 1990's, when cheap, soda-lime glass substrates were used instead of the typical borosilicate glass or alumina ones. Diffusion of sodium from the substrate led to an increase in efficiency, mostly through an improvement in V_{OC} and the fill factor. Since then, other alkali elements such as potassium and rubidium have been successfully used to improve the performance of CIGS solar cells. And even though all of the commercially available CIGS cells include alkali doping, the precise mechanism of its beneficial effect is still under debate. To date, most experimental research focuses on the comparison between alkali-free and alkali-rich cells or films, sometimes with different alkali types or incorporation methods, with only a few cases where alkali concentration in the films was varied between samples. To better understand the pathway of alkali operation it might be important to study the influence of different alkali concentrations over a broad range of different devices.

Another interesting aspect of CIGS solar cells is the persistent photoconductivity – an increase in the observed conductivity and carrier concentration (and, as a result, also power conversion efficiency) under illumination, which remains even after the light source has been turned off, provided temperature is low enough. Again, this effect was previously mostly studied on either alkali-free or alkali-rich devices.

In this work, a systematic study of the effect of different concentrations of sodium and potassium, on the relaxed and metastable electrical and capacitive properties of CIGS devices is presented. Main type of samples were thin films and complete cells with CIGS absorbers fabricated by single stage process providing layers of uniform morphology and composition. For better insight into the physical properties also larger-grained three-stage CIGS used in commercial manufacture was studied-. Alkali doping was achieved through post-deposition

treatment (PDT) to limit the impact of alkalis on sample morphology[2]. The control over the amounts of alkalis introduced into both types of samples was achieved through varying PDT temperatures. On thin films, conductivity vs temperature measurements were done in both relaxed and metastable state. In the case of solar cells, free carrier concentration was measured through Drive Level Capacitance Profiling (DLCP) in both relaxed and light-soaked state. Comparison between solar cells and thin films allows to distinguish between the effect originating in the absorber and at the junction/interfaces.

In thin films, the addition of sodium resulted in an increase in conductivity and decrease in activation energy of the σ(T) slope, dependent on the sodium concentration in the film. Almost the same result was observed with potassium, except 4x more potassium was needed for the same effect. The only difference was observed for low-potassium films, where the conductivity decreased significantly, presumably due to secondary phases and resulting internal barriers arising at low K-PDT temperatures. The same dependence on alkali concentration, for both single-stage and three-stage devices, doped with either Na or K was observed in the free hole concentration on solar cells, the only difference here being that the increase in p was half of the orders of magnitude of the increase in conductivity. All of those results point to the alkali effect being independent of the alkali type, originating in the absorber rather than at the interfaces, and influencing both the carrier concentration and the mobility.

Persistent photoconductivity was found to depend on the alkali concentration in the same manner as the relaxed properties. The one interesting fact observed here is that the PPC is proportional to the relaxed conductivity over multiple orders of magnitude, even in the low-potassium thin films. This strongly suggest the same principle limiting the relaxed parameters as well as the magnitude of the PPC.

The impact of alkali doping on CIGS absorbers could be explained by the model of alkali-induced passivation of defects at the grain boundaries. Defect-induced barriers at the grain boundaries would limit both the mobility and the carrier concentration through depletion regions within grain bulk. This model was compared with the experimental data and despite its

[2] All of the device manufacture, alkali-doping, compositional and basic photovoltaic characterization was done by prof. Roland Wuerz and Alexander Eslam at Zentrum für Solarenergie und Wasserstoffforschung (ZSW) in Stuttgart, Germany

simplicity a good correlation between simulation results and experiment was achieved. Thus, the main conclusion of this work is that the dominating factor which contributes to the solar cells efficiency increase due to alkali doping is the passivation of grain boundaries. Other effects, such as doping of the interior of the grains, although not excluded, probably have a less significant effect.

Keywords: $Cu(In,Ga)Se_2$, solar cells, grain boundaries

Table of Contents

Structure

The first 5 chapters contain introductory information regarding the subject of the thesis. In the first chapter, basic principles of solar cells physics are outlined. This is followed by detailed description of $Cu(In,Ga)Se_2$ technology in Chapter 2, including information about the structure, manufacture methods and means of alkali introduction into the layers. In the next chapter a brief description of defects in $Cu(In,Ga)Se_2$ is presented, underlining the electronic effects of grain boundaries. Next is the persistent photoconductivity, with its experimental observations and theories explaining its origin. Finally, in Chapter 5 alkali element doping is characterized, with description of its effects on solar cells and thin films, location in the CIGS absorbers and a list of theories that have been used to explain its effects.

Chapter 6 contains the motivation, outlining questions this thesis tries to answer and the means used to achieve it.

In Chapter 7 the physics behind characterization methods used in this work is described. These include Drive Level Capacitance Profiling and measurements of conductivity of thin films as a function of temperature.

In Chapter 8 the experimental details regarding studied devices and measurement protocols and setups are described. These include tables of photovoltaic parameters of solar cells and the values of alkali concentration in the devices obtained through Secondary Ion Mass Spectroscopy, provided by the collaborators from ZSW.

In Chapter 9 experimental results are presented. Those are divided by the type of alkali-doping used, and contain measurement results on thin films and solar cells in both relaxed and metastable state. Two additional subsections deal with the impact of selenium annealing and copper concentration variations to distinguish between the impact of doping and variation between devices.

Chapter 10 contains discussion of the results. Here, the results on both thin films and solar cells, as well as with sodium and potassium, are compared. This is also the chapter, in which grain boundary passivation model is introduced and compared with experimental results.

Chapter 11 contains the conclusions and description of further work needed to explore the subject further.

1 Introduction

1.1 The climate change

From 1950 to 2015, the global population rose from 2.5bln to 7.3bln, while the percentage of those suffering extreme poverty decreased from 63% to 10% [1]. This was possible in a significant part due to cheap energy fueling the production of fertilizers, mechanization of agriculture, household electrification, transport and industry. These energy sources, however, were fossil fuels: coal, natural gas and mineral oil – all of which contribute to the climate change. Now, with CO_2 emissions rising, the need for alternative energy sources – be it nuclear, solar or wind – is more pressing than ever before. This need becomes even more evident if we factor in the increasing cost of CO_2 emission certificates (EU ETS) [2], and the geopolitical implications of oil and gas trade.

According to the International Energy Agency (IEA) about 75% of CO_2 emissions come from electricity production [3]. One way to reduce that number is to increase the share of solar-generated electricity. Reaching the COP26 net zero scenario may be impossible without the increase in PV capacity.

The first modern solar cells were developed as a mean to power telephone line repeaters, and were developed by Bell Lab's employees Daryl Chapin, Calvin Fuller, and Gerald Pearson in 1954 [4]. They were silicon-based devices with a power conversion efficiency of about 6% [5]. By 1955, the first module, with 35Wp power, was installed by Bell labs in Americus, Georgia [6]. Right now, the world's largest solar power plant in Gonghe, China, has installed power of 2.2GWp. Global installed solar power increased from 1.3GWp in 2000 to over 700GWp in 2020 and constitutes about 1% of global energy consumption, and about 3% of electricity [7]. Moreover, it is an energy source that recorded the steepest price decline: from 360$/MWh in 2009 to 37$/MWh in 2020, and in the USA its price is cheaper than that made using natural gas and considerably cheaper than coal [8].

Now more than ever it is important for this trend to continue. In order to achieve that it is important to study and improve photovoltaic technologies – their efficiency, cost of production, materials usage as well as their potential to be recycled after disposal. In this work I will focus on the physical properties of CIGS films and the impact of alkali doping on their efficiency.

1.2 Photovoltaics

In order for a solar cell to work, three prerequisites have to be met:

- light has to be absorbed generating free charge carriers (current generation)
- there has to be a potential difference (voltage)
- those carriers have to be separated to respectable contacts before they recombine

A device most commonly used to achieve that is a p-n junction, a n and p-type semiconductors joined together, either made from a single material (homojunction) or two different materials (heterojunction).

1.2.1 The p-n junction

Doping is achieved by introducing impurity atoms, which energy levels are shallow enough so that at room temperature they are ionized into a free charge carrier and an ionized impurity atom, according to formula (1), for donors:

$$N_D = n^- + N_D^+ \tag{1}$$

and acceptors:

$$N_A = p^+ + N_A^- \tag{2}$$

where N_D is the concentration of donors, N_A concentration of acceptors, n – concentration of free electrons and p – concentration of free holes.

The n- and p-type doping in a p-n junction creates a gradient concentration of free electrons and holes. Holes diffuse to the n-side while electrons diffuse to the p-side leaving ionized donors/acceptors behind. Once the carriers go to the other side, they become minority carriers and recombine with the majority carriers of the other side. Between the two types of semiconductors a charge-depleted region appears, called the space-charge region (SCR). Since the charge of ionized donors/acceptors is no longer compensated by the free carriers (depletion), electric field appears in the SCR, mitigating the effects of diffusion gradient: keeping the electrons on the n-side and holes on the p-side, and drift current emerges.

In the p-n junction in thermal equilibrium in the dark, the Fermi levels on both sides are aligned. Once light shines on a device, and additional charge carriers are generated ($\Delta n = \Delta p$), the equilibrium no longer exists, and Fermi levels split:

$$E_{Fn} - E_F = k_B T \ln\left(\frac{n_0 + \Delta n}{n_0}\right) \quad (3)$$

$$E_F - E_{Fp} = k_B T \ln\left(\frac{p + \Delta p}{p_0}\right) \quad (4)$$

The maximum voltage one can extract from the solar cell, the open-circuit voltage (V_{OC}) is limited by the Fermi-level splitting according to Formula (5), therefore adequate doping is essential for a good solar cell:

$$q\, V_{OC}^{max} = E_{Fn} - E_{Fp} \quad (5)$$

An ideal solar cell can be described using a diode equation, showing the relation between current density J and voltage V:

$$J = J_0 \left[\exp\left(\frac{q\, V}{A k_B T}\right) - 1\right] - J_{SC} \quad (6)$$

where J_0 is the diode saturation current, q is the elementary charge, T is the temperature in Kelvins, k_B is the Boltzmann constant and J_{SC} describes the short-circuit current (photocurrent) density and A is the ideality factor describing the type of recombination. For practical reasons, current density J (current per area) is typically used instead of current.

An example of a current-voltage (JV) characteristic of a solar cell is presented in Figure 1.1. Points describing the most important solar cell parameters were marked in the figure, and consist of:

- **open-circuit voltage V_{OC}** limited by the Fermi-level splitting and recombination, strongly dependent on temperature and weakly on illumination intensity
- **short-circuit current density J_{SC}** roughly proportional to illumination
- **maximum power point (MPP)** – an optimum working point of the cell, in which the extracted power can be maximized
- **efficiency $\eta = \frac{J_{mpp} \cdot V_{mpp}}{P_{sun}}$**
- **fill factor FF** $= \frac{J_{mpp} \cdot V_{mpp}}{J_{SC} \cdot V_{OC}}$ describing how the JV curve deviates from a rectangle, impacted mostly by the shunt and series resistance. Graphical representation of FF is the ratio between the dark-gray and light gray rectangle in Figure 1.1.

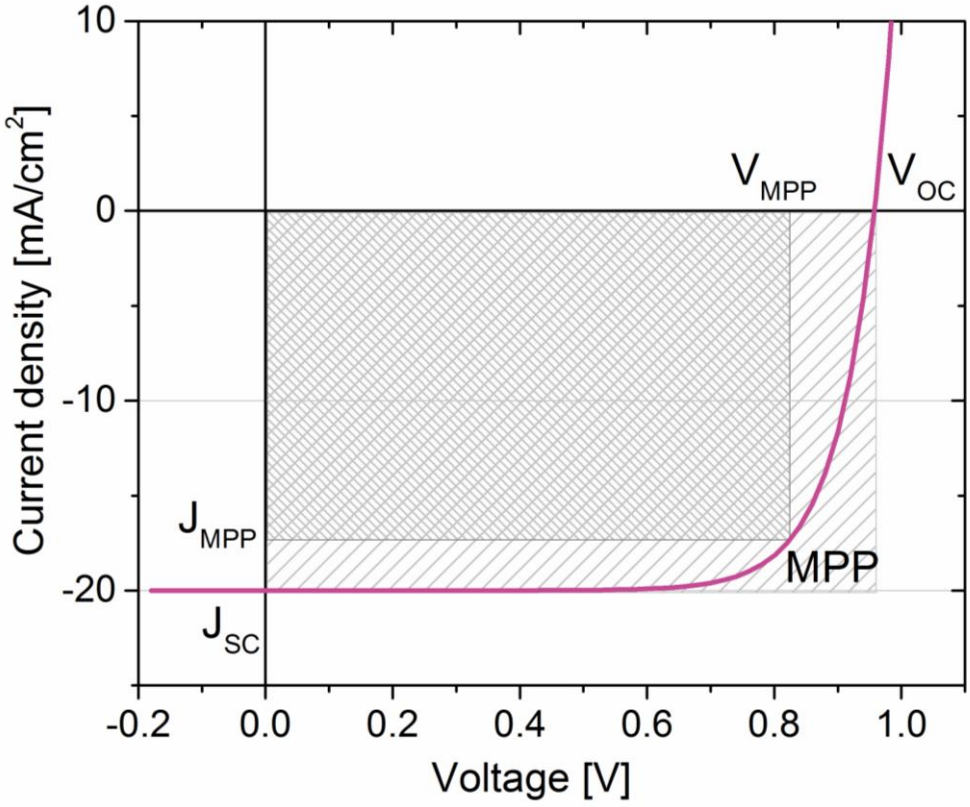

Figure 1.1 Example of an ideal JV curve. J_{SC} is the short-circuit current, V_{OC} the open-circuit voltage, MPP denotes the maximum power point.

1.2.2 Main types of solar cells

Conventional solar cells can be divided into two major groups: wafer-based devices, and thin-film cells, in which the active layers are deposited onto substrates such as glass, steel or polymer foils.

Wafer-based technologies date back to the 1950's and consist primarily of silicon (mono-Si and poly-Si) and gallium-arsenide (GaAs) cells. In this type of devices, the absorber is thick and rigid enough to act both as an active material and a substrate. This limits their use to rigid module technologies and demands great crystallinity and purity of the materials to compensate for the thickness to maximize the carrier diffusion length. On the upside, silicon photovoltaics benefits from the decades of advances in microprocessor technology, as they share the same substrate, and as the oldest and the most established photovoltaic technology, constituted 95% of the global market share in 2020[9].

The other major group of photovoltaic technologies are the conventional thin film cells, namely: amorphous silicon (a-Si:H), cadmium telluride (CdTe) and chalcogenides (CIGS). Their total market share is about 5%, distributed between CdTe (78% of thin-film), CIGS about 19% and a-Si:H below 2%[9]. Here, the photovoltaic material has a direct bandgap and very high absorption coefficient, meaning a layer of thickness between 100nm and 10μm can be used. This, together with the sputtering and evaporation methods of material deposition opens up the technology to a wide range of substrates, including flexible polymer sheets, and allows for semitransparency (through adjusting the absorber thickness) that can be used in building-integrated photovoltaics (BIPV) applications.

2 $Cu(In,Ga)Se_2$

2.1 $Cu(In,Ga)Se_2$ solar cells

Copper indium gallium selenide ($Cu(In,Ga)Se_2$, CIGS) is one of the most commonly used materials for thin film photovoltaics, with its use dating back to the 1970's (in the form of $CuInSe_2$) [10, 11]. It crystallizes in a chalcopyrite structure, and what is remarkable about it is its ability to handle off-stoichiometric compositions with regards to the copper deficiency [12]. Actually, it is the stoichiometric CIGS that possesses poor photovoltaic properties, with cell efficiencies in the range of 10% and increased recombination at the interfaces [13]. It is likely caused by a formation of a Cu_2Se phase at the surface of copper-rich grains (more about the grain boundaries can be found in chapter 3.3) [14]. Currently, most of the cells are prepared with 80% CGI (Cu/(In+Ga), meaning 80% of the stoichiometric concentration of Cu), and although their grains are smaller than those of Cu-rich cells [14], it is offset by the improved junction properties. and recombination happening mostly in the depletion layer. Because of their off-stoichiometry, CIGS materials are rich in defects, mostly copper vacancies (V_{Cu}) and $In(Ga)_{Cu}$ antisites. What is also remarkable is the benign character of structural defects in CIGS, such as grain boundaries [15]. An important defect-related property found in CIGS is its self-compensation – although the defect density is in the range of $10^{18}cm^{-3}$, the carrier density (holes) is the range of $10^{16}cm^{-3}$ – donors (antisites) and acceptors (Cu vacancies) counteract each other.

Another important feature of the $Cu(In,Ga)Se_2$ is the possibility of bandgap tuning through adjusting the In/Ga ratio, from 1.02eV for $CuInSe_2$ (CIS) to 1.68eV for $CuGaSe_2$ (CGS)[16]. This can be used both to find an optimum bandgap with regards to the Shockley-Queisser limit [17] and in tandem solar cells [18]. For single-junction solar cells, the typical GGI (concentration of gallium divided by that of both gallium and indium) is about 20-30%, corresponding to a bandgap of around 1.2eV. Sometimes bandgap grading, namely a variation of the GGI throughout the sample, is used to maximize the efficiency [19].

2.2 CIGS solar cell structure and manufacture methods

A CIGS solar cell can be prepared on a glass, polymer, ceramic or metal substrate covered by a molybdenum layer acting as the back contact. The active material, CIGS, forms the absorber, which main function is the absorption of light and generation of free charge carriers. The thin CdS buffer layer forms the p-n junction, and acts as a mediator between the lattice constants of CIGS and the window layer. The next layer is the window, a transparent conductive oxide (TCO), which acts as the front electrode. Sometimes an additional metallization grid is used to improve carrier collection. Usually, an anti-reflection coating is used to reduce reflection losses and to maximize energy efficiency (solar cells used in this work do not possess AR coating).

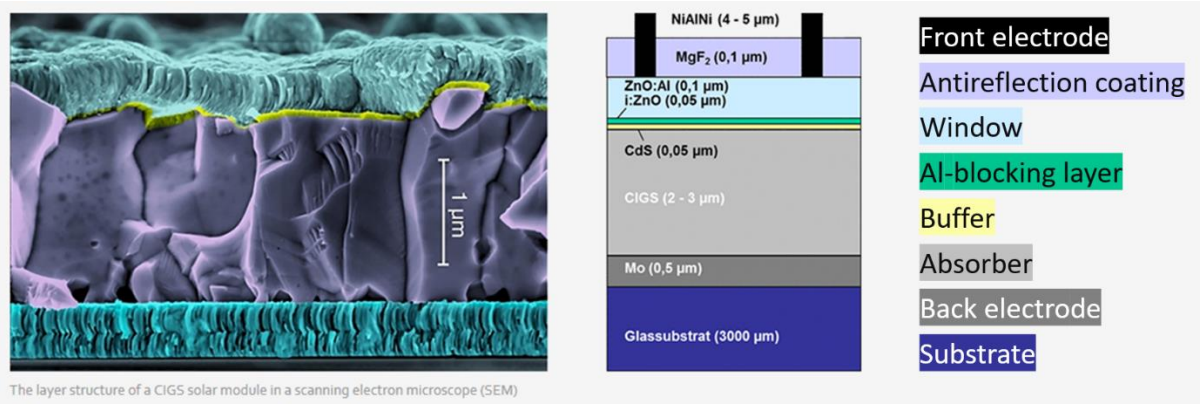

Figure 2.1. Scanning electron microscopy image of a cross section of a CIGS solar cell without AR coating and grid front electrode (left). Schematic of a complete solar cell with description of each layer (center and right). Adapted from ZSW [20].

2.2.1 Substrates

Currently, the most commonly used substrate material is regular, soda-lime glass (SLG). It is not only cheap and readily available, but also has a similar thermal expansion coefficient to CIGS, reducing the impact of thermal stress [21]. However, probably the biggest benefit of SLG is that it contains sodium, which is both beneficial to the CIGS morphology and increases the doping density in CIGS by orders of magnitude (see Chapter 5). If a controlled amount of sodium is needed, for instance in laboratory testing, a thin layer of a sodium-blocking material, such as SiO_2, Al_2O_3 or SiO_xN_y can be deposited on top of SLG [22]. Borosilicate glass (BSG, known also as Pyrex® or Corning Glass)[23, 24] and zirconia (ZrO_2)[25–27] are also sometimes used to limit diffusion of sodium from the substrate, mostly in the laboratory setting.

As CIGS is a thin-film technology, also flexible substrates may be used for deposition. Those include metal foils: stainless steel [28–31] and titanium [25], as well as polymers, such as polyimide (also known as Kapton®)[32, 33].

2.2.2 Back electrode

On top of the substrate, a 500nm-thick molybdenum back electrode is deposited. It is virtually the only metal currently used for the back contact, as it doesn't react strongly with the Se during CIGS deposition, does not diffuse into the CIGS layer, possesses matching thermal expansion coefficient, and most importantly, produces good ohmic contact to the CIGS material [34]. The most common way of Mo-contact deposition is through DC magnetron sputtering [35].

2.2.3 Absorber

$Cu(In,Ga)Se_2$ absorbers are manufactured using mostly one of the two main processes:

Sequential deposition / Selenization method

Sequential deposition was developed by Siemens Solar for CIS cells in the 1980's [36], and is or was formerly employed by: Honda Soltec, Miasole, Bosch CIStech, Showa Shell and Solar Frontier on either rigid glass or stainless steel foils [37–39]. It consists of DC sputtering of metals (Cu, Ga, In) and subsequent annealing in Se atmosphere in the form of hydrogen selenide H_2Se – highly flammable and toxic gas [40].

Coevaporation

In the coevaporation method, the elements are evaporated from elemental sources with no selenization step, at the substrate temperature between 400°C and 600°C. This allows for an easier in-line processing, including roll-to-roll methods. This types of processes are used by, among others: Manz – Würth Solar, Solibro and Hanergy [37, 38].

Coevaporation deposition comes in three main forms:

- In the **single-stage process** all of the elements are evaporated at once, at a constant rate, and Cu is kept lower than stoichiometry (typically 80%).
- The **two-stage process (Boeing process)** [41] of two steps, where the first layer is prepared Cu-rich (close to stoichiometry) and the second is Cu-poor.

- The **three-stage process** currently produces the most efficient CIGS cells [42], and allows for a bandgap grading through the variation in In/Ga concentration between the layers. It consists of three steps: first indium, gallium and selenium are deposited at a moderate temperature of about 400°C, followed by a Cu-layer deposited at high temperature of about 600°C, then again In, Ga and Se. The temperatures used are high enough to ensure the intermixing of the elements to form CIGS material, while at the same time the time duration does not allow for their homogenous distribution.

2.2.4 Junction / buffer

$Cu(In,Ga)Se_2$ with typical gallium concentration is grown p-type [12, 43], therefore another material is needed to form a heterojunction. Most commonly, a thin layer, about 50nm thick, of CdS is used as the buffer layer due to its very good lattice match and band alignment. It is typically deposited using chemical bath deposition (CBD). In order to get rid of the wet chemistry process and cadmium incorporation, sometimes alternative buffer layers, such as zinc compounds are used, but the CBD CdS still yields the best results [16].

2.2.5 Window / front contact

On top of the absorber, a transparent front contact, known as the window is the deposited. It is made of a transparent conductive oxide (TCO) – material with a large bandgap and good electrical conductivity. In CIGS it is typically a DC-magnetron sputtered 0.5-2μm Al:ZnO layer, (due to its high conductivity, in the range of 2000 S/cm). To inhibit the interdiffusion of Al into the CdS/absorber, a 50-100nm i-ZnO barrier for diffusion of Al is deposited using RF-magnetron sputtering [14, 44, 45].

3 Defects

3.1 Defects in solids

Deviation from an ideal crystal lattice may be manifold – from point defects, such as misplaced ions or impurity atoms, to structural modifications such as dislocations or grain boundaries. In this part, I will focus mostly on the first type.

The most common way of describing point defects in through the Kröger-Vink notation [46]:

$$A_C^B \tag{7}$$

where A denotes the type of atom (In, Ga, etc.) or lack thereof – a vacancy (V), B describes the relative charge to the lattice site (sometimes omitted), and C – the lattice site, either by naming the expected ion, or an interstitial (i). In example, V_{Cu}^{-} would refer to a vacancy occupying the copper lattice site and resulting in a -1 change in the charge, and In_i^{2+} describes and interstitial In ion, with a charge of 2+. The most common point defects are:

- **Vacancies V_x** where a void is located in place of an ion
- **Interstitial ions X_i** where an ion, either intrinsic or impurity, is located on an interstitial site
- **Substitutional defects X_y**, where a lattice site is occupied by a different ion, be it impurity ions (extrinsic) or an antisites – misplaced intrinsic ion

Defects can create states in the band structure of the material. If the level is located inside the bandgap, we define its energy as the difference between the defect level and the VBM or CBM. With regards to the electrical properties, we can divide defects into:

- **Shallow defects**, i.e. donors and acceptors – defects that are fully ionized at room temperature, creating free electrons (donors) or holes (acceptors). If more acceptors than donors are present in the material it exhibits p-type properties, if donors – n-type.
- **Deep defects**, which depending on their effective capture cross section for charge carriers, can either be:
    - **Traps**, with large capture cross section for one carrier type and small for the other, leading to the capture and release of one type of carrier

- **Recombination centers**, which have similar capture cross sections for both types of carriers, resulting in recombination after trapping two oppositely charged carriers. Detrimental for device efficiency

Metastable defects, are a separate group of defects that can be either shallow and deep. They can change their properties depending on the electronic configuration. An example would be the DX centers.

3.2 Important electrically active intrinsic point defects in CIGS

Cu(In,Ga)Se_2, due to its complicated stoichiometry as well as copper deficiency is rich in intrinsic defects. Some of the most important ones – either because of their sheer quantity, or their suspected impact on the electronic properties – are described in this chapter. Among extrinsic defects, the most impactful ones will be those connected to the alkali incorporation. Those will be described in chapter 5.2.3.

The most common defect in Cu(In,Ga)Se_2, be it in copper-poor or copper-rich stoichiometry, is the **copper vacancy $\mathbf{V_{Cu}^{-}}$**. It is very shallow, with the defect energy level located between 30meV from the VBM in CIS to 10meV in CGS(exact location depending on the GGI) and a low formation energy [15, 43]. It is the dominant acceptor in CIGS[14].

Another type of defect with a very low formation energy are the **substitutional defects $\mathbf{In_{Cu}^{2+}}$ and $\mathbf{Ga_{Cu}^{2+}}$**. Those are the main donors in the CIGS materials. In_{Cu}^{2+} is a donor, which is also though to act as a non-radiative recombination center [47]. It is likely benign though, as it is readily passivated by V_{Cu} forming ($2V_{Cu}$-In_{Cu}) defect pairs [12, 48]. This explains why the measured concentrations of free holes, typically 10^{14}–10^{16}cm^{-3} in the material are orders of magnitude lower than the V_{Cu} concentration (in the range of 10^{18}–10^{19}cm^{-3}), as V_{Cu} and In_{Cu} are mutually compensating [49]. Ga_{Cu}^{2+} on the other hand is a deeper donor, and it not likely to be passivated by copper vacancies.

Another important intrinsic defect is the **selenium vacancy $\mathbf{V_{Se}^{2+}}$**. It is a double donor (thus the +2 relative charge)[14].

3.3 Grain boundaries

Generally, grain boundaries are filled with point defects, as well as impurities tend to segregate on them. This is why most materials are better in monocrystalline form (Si and GaAs being prime example). However, polycrystalline CdTe and CIGS cells perform better than single-crystal [50, 51]. In alkali-doped CIGS, conductive atomic force microscopy (c-AFM) showed enhanced current collection at GBs [52], and the Kelvin probe force microscopy showed that recombination at GBs is reduced, meaning they could separate charge carriers due to the built-in electric field rather than lead to an increased recombination[53].

The studies shown that there are three major types of GBs in CIGS materials with regards to their electronic impact [54]:

- **Neutral**, typically symmetric, twin GBs with no change in stoichiometry with regards to bulk CIGS [55].
- **Beneficial**, typically random high-angle GBs (RHAGB), at which sodium segregation of about 2at% is observed, together with Cu depletion and an increase in selenium concentration [56] (more about the impact of sodium on GBs can be found in Chapter 5.1.3).
- **Detrimental**, RHAGB with little sodium (0.5at%), increased copper concentration and reduced selenium concentration, sometimes oxidated [56]

In the work of Raghuwanshi et al. [56] electron beam induced current (EBIC) measurement showed that in a sodium-doped devices about 27% of GBs were neutral, 58% beneficial, and 15% detrimental.

3.3.1 Models explaining the electronic impact of grain boundaries

There were multiple models explaining the impact of grain boundaries on CIGS solar cells proposed, here the most common ones will be presented:

Structural barrier model (downward band bending + neutral charge)

The structural barrier model assumes that the grain boundaries act as uncharged barriers. Here, band bending of the VB is observed close to the GB surface. This results in a neutral barrier for holes, and creating a hole-free path for electrons through the GBs, suppressing recombination [50, 51, 57]. This model postulates the presence of electrically inactive defects at the GB surface, as the active defects, i.e. in GaAs and Si create recombination centers. Density functional theory calculations by Persson and Zunger support this model, with Cu depletion at GB surface, leading to the lowering of the VBM and the formation of a hole barrier at GBs [50]. Additionally, calculations by Yan et al. [57] showed no deep defect centers at GB surface due to surface atomic relaxation, as well as no charge.

Electronic barrier model (downward band bending + positive charge)

In the electronic barrier model, the GBs cause downward band bending in both the conduction and valence bands, resulting in a hole repulsion similar to the one in the structural barrier model, but on top of that, the GBs are positively charged, further influencing charge separation by attracting electrons while creating a barrier for holes [58–60]. This again would result in a better carrier collection – electrons, the minority charge carriers, need to only diffuse to the closest grain boundary, through which they are then channeled into their respective electrode. As the grains in CIGS are usually columnar, most of the free holes would not need to cross a GB – a barrier – on the way to the electrode. If they do need to cross it though, the energy barrier would limit the hole mobility as well as could lead to recombination, killing both the V_{OC} and FF [61]. Scanning Kelvin probe microscopy measurements often show positively charged GBs, and the charge dipoles at them could lead to a downward band-bending [58, 59].

Type inversion at the GBs

The type inversion model is a more pronounced variation of the downward band-bending, where it is strong enough to cause type inversion in the vicinity of the GBs, causing the formation of local p-n junctions on the GBs, improving the electron collection. On the other

hand, the existence of the n-type regions (and downward band-bending in general) would limit the overall doping in the absorber bulk, especially in the small-grained material [61, 62].

Upward band-bending

There are some reports in which upward band bending was observed on GBs using Kelvin Probe Force Microscopy. Upward band bending would result in attraction of holes and repulsion of electrons. Such effect was observed by Raghuwanshi et al. on detrimental grain boundaries and linked to Cu enrichment [54].

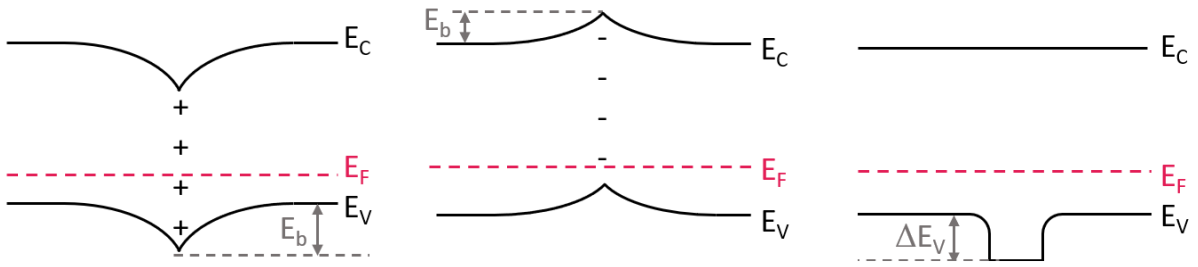

Figure 3.1 Energy band diagram of a grain boundary with: downward band-bending caused by donor defects (left), upward band-bending caused by acceptor defects (middle), downward shift of the VBM caused by a region with a different stoichiometry – structural barrier (right). E_b denotes barrier height, ΔE_V – change in VBM.

3.3.2 Simulation studies of GB effects in CIGS

Taretto and Rau [63] as well as Gloeckler et al. [64] studied the effect of horizontal and vertical GBs on the photovoltaic parameters of CIGS solar cells using 2D simulations. In general, they found that an increased amount of charged defects at the grain boundaries Q_t led to a decrease in calculated efficiency due to reduced V_{OC} and FF. In more detail, the results on the three studied cases can be expressed as follows:

- **Valence band offset with positive charge**, resulting from donor defects at the GBs, attracting electrons and repelling holes. A small barrier was found by Gloeckler et al. to increase recombination, while a larger barrier, leading to type inversion is supposed to reduce it [64]. Similarly, Taretto et al. observed a small increase in predicted J_{SC} for inverted GBs. Due to expected doping and grain size, existence of an inverted GB is

unlikely in real CIGS [63]. In general, higher band bending was attributed to increased carrier collection, but an overall loss of efficiency due to reduced voltage.

- **Valence band offset without charge**, where different stoichiometry at the GBs results in a downward shift in VBM was found by Taretto et al. to be slightly beneficial in vertical (reduced recombination), and detrimental in horizontal GBs (reduced mobility). On the other hand, Gloeckler et al. deemed such columnar GBs as detrimental to device efficiency, while horizontal GBs within the SCR region of the junction beneficial due to suppressed recombination.

4 Persistent photoconductivity

4.1 Experimental observation of PPC in CIGS

A typical property of $Cu(In,Ga)Se_2$ solar cells, observed also in other semiconductor compounds including among others GaAs, AlGaAs and CdZnTe, is the so-called persistent photoconductivity (PPC) – a metastable increase in conductivity of CIGS layers after illumination that can persist for hours up to days depending on the temperature [65]. In Figure 2.1 a typical conductivity vs temperature measurement, $\sigma(T)$ is shown. The bottom curve, labeled with σ_R represents a typical dark measurement. After illumination and subsequent cooling, the metastable state is fixed and the conductivity increases by 1-3 orders of magnitude, and the slope (activation energy) becomes lower. During heating, PPC persists until reaching the anneal-out temperature, visible as a change in slope of the σ_{LS} curve. The anneal-out temperature is linked to that of the light-soaking [66], and the effect created at room temperature typically anneals out between 250K-300K [67, 68]. The magnitude of the PPC does not depend strongly on the illumination intensity, provided the LS duration is sufficiently long [66].

In solar cells PPC is visible as an increase in capacitance. This was linked to an increase in free hole concentration as measured by CV or DLCP [69–71], typically by an order of magnitude (in the range of 10^{15}-$10^{16}cm^{-3}$). An example result from a DLCP measurement in both relaxed and metastable state can be seen in Figure 2.1. Additionally, PPC in solar cells leads to a temporary increase in efficiency caused by, among others: an increase in the V_{OC} due to increased doping density and reduction in the SCR width, reducing the recombination in the SCR [72]; an improvement of the fill factor and the reduction of the double-diode behavior [23, 67]. A decrease of the fill factor, correlated to an increase of the diode ideality factor due to metastable defects was also reported [73, 74].

PPC is observed in both solar cells and thin films [66, 75, 76], made from either polycrystalline or single-crystal CIGS [65, 75], in cells incorporating CdS, In_2S_3 and Zn-based buffer layers [23, 77, 78], as well as in both alkali-free and alkali-doped devices [79–81]. This all points to the effect being strictly linked to the chalcopyrite material itself.

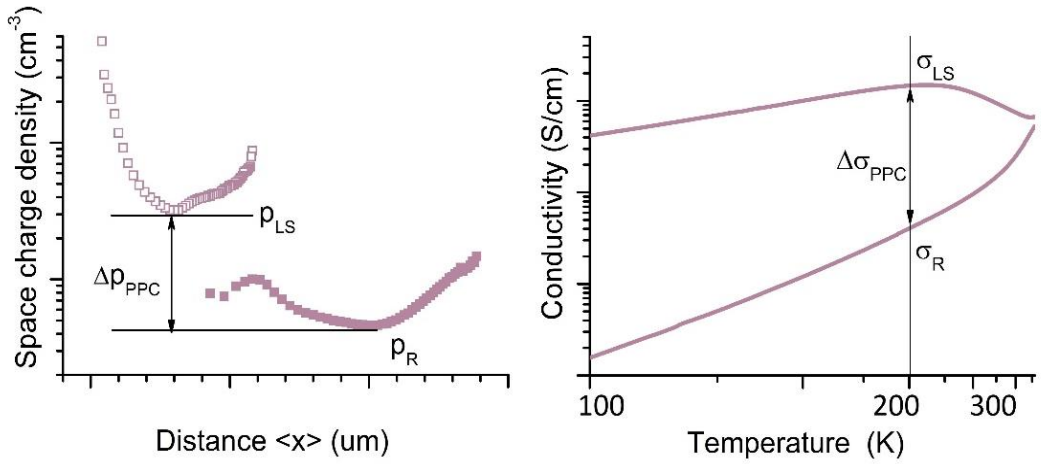

Figure 4.1 Charge carrier concentration in a CIGS material in a relaxed (p_R) and metastable state (p_{LS}) (left). Conductivity vs time relation in CIGS material in relaxed and light-soaked state (right).

4.2 Models of persistent photoconductivity in CIGS

Over the decades, multiple models explaining the PPC were proposed. The most prominent are:

- **Macroscopic barrier model** in which a macroscopic barrier inhibits the e-h recombination [82, 83]. On the interfaces (i.e. grain boundaries) macroscopic potential barriers exist and the charges are separated by the band bending at those, increasing the barrier height. Then, once the sample is cooled down, the barriers inhibit recombination and the lifetimes of carriers become very long.
- **Copper interdiffusion**. Copper in CIGS was found to be prone to electromigration [84]. It was speculated that Cu^+ ions could be moving in the SCR away from the interface and into the bulk, while V_{Cu}^- would move towards the interface. This would result in a change in the electric field in the device, as well as could influence its defect chemistry [85]. This model does not explain the PPC effect in thin-films.
- **Large lattice relaxation / DX center**. The most accepted theory, involving an amphoteric defect changing its state under illumination from donor to acceptor configuration with subsequent large lattice relaxation (it is, a barrier impeding relaxation [86]. Its precise mechanism will be described in the next chapter.

4.3 The Lany-Zunger model

The model proposed by Lany and Zunger describes the PPC as being caused by an amphoteric vacancy complex (V_{Se}-V_{Cu}). In CIGS, almost all V_{Se} will be in complexes with V_{Cu} at room temperature [87]. This defect complex can exist, among others, in two distinct configurations:

- **$(V_{Se}$-$V_{Cu})^{+}$** which is a shallow compensating donor/donor state, which creates a perturbed host state (PHS) right below CBM. It is linked to the large In-In distance
- **$(V_{Se}$-$V_{Cu})^{-}$**, a shallow acceptor state, similar to an isolated V_{Cu}, linked to the short In-In distance

An amphoteric defect level can described by the transition level, here: ε(+/-), which denotes the position of Fermi energy E_F, where the defect complex changes from + (donor) to – (acceptor) state, temporarily increasing the free hole concentration. As the conversion is linked to the large lattice relaxation, more precisely to the change in the distance between neighboring indium atoms (d_{In-In}), the metastable state can persist for a long period of time after the E_F changes back, as an energy barrier needs to be crossed to relax back.

The complete reaction of transition from the donor to the acceptor state can be summarized as:

$$(V_{Se} - V_{Cu})^{+} + e^{-} \xrightarrow{\Delta E_1} (V_{Se} - V_{Cu})^{-} + h^{+} \tag{8}$$

where the ΔE_1 denotes the activation across the energy barrier. The relaxation process requires the activation across the ΔE_2 barrier:

$$(V_{Se} - V_{Cu})^{-} + 2h^{+} \xrightarrow{\Delta E_2} (V_{Se} - V_{Cu})^{+} \tag{9}$$

From the practical point of view, the transition energy ε and the position of the Fermi energy in the relaxed state should give us the magnitude of the PPC. If we denote the free hole concentration in the relaxed state as p_R and in the metastable state as p_{LS} as in Maciaszek and Zabierowski [88], then the magnitude of the PPC can be described as:

$$\Delta p_{PPC} = p_{LS} - p_R \tag{10}$$

and the Δp_{PPC} is equal to double the number of (V_{Se}-V_{Cu}) complexes that changed state from the donor to acceptor configuration during LS. If we then assume that in the LS state almost all

of the complexes are in the acceptor state, the magnitude of the PPC would be given by the concentration of the vacancy pairs N_M and the percentage of the complexes already in the acceptor configuration f_A in the relaxed state [88]:

$$\Delta p_{PPC} = 2\, N_M (1 - f_A) \tag{11}$$

where f_A is equal to:

$$f_A = \frac{1}{1 + \left(\frac{p_R}{N_V}\right)^2 \exp\left(\frac{2\varepsilon}{k_B T}\right)} \tag{12}$$

In principle, the lower the free hole concentration is in the relaxed state, it is, the further above ε is the E_F, the more of the vacancy pairs are already in the acceptor state before the illumination – so the magnitude of the PPC is lower. In a highly p-type CIGS, most of the vacancy pairs are in the donor configuration and can be converted to acceptor configuration, leading to a higher PPC. This relation is graphically presented in Figure 4.2.

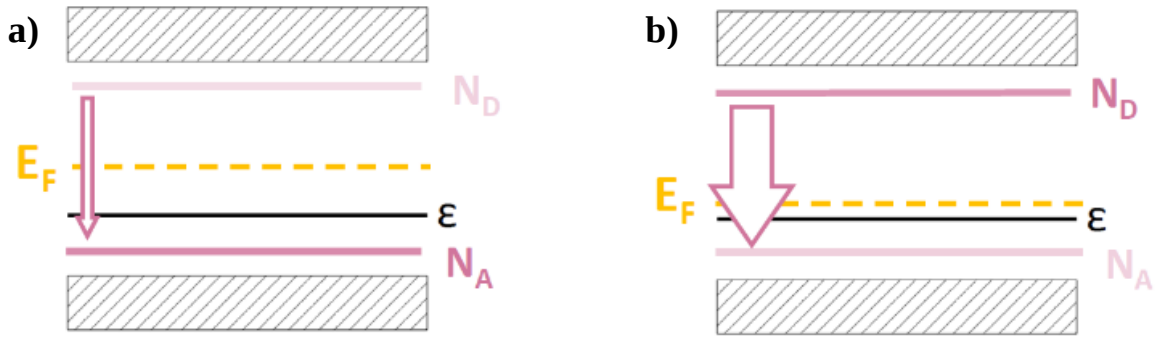

Figure 4.2 Schematic representation of the magnitude of PPC in the a) low doped CIGS, with Fermi energy high above ε, b) highly p type CIGS. N_A and N_D color intensity correspond to the share of the (V_{Se}-V_{Cu}) pairs in an acceptor or donor configuration in the relaxed state.

5 Alkali doping

In this work, the influence of alkali metals – sodium and potassium – on the device properties will be studied. To fully understand the significance of those, one can look at Figure 5.1, where the evolution of CIGS efficiency versus time is presented, together with the biggest improvements made to the devices. In the late 1980's an efficiency improvement was made due to thinning of the CdS layer from 6µm to 100nm. Potassium, discussed in this work, allows for the deposition of an even thinner layer of the CdS and betters the junction properties. The most significant increase so far was seen in the early 1990's, when the cells started being manufactured on soda-lime glass, introducing doping with sodium (pink shading in Figure 5.1) [89, 90]. Around the same time, three-stage cells were developed [91]. Lastly, doping with other alkalis, such as potassium and rubidium, gave rise to another efficiency jump in the mid-2010's, followed by a steady increase in efficiency, taking place up to now (yellow shading) [33, 91–93].

In this chapter, the main topics of alkali doping will be discussed – including different incorporation methods, observed changes in the device properties as well as proposed mechanisms of the alkali-effect.

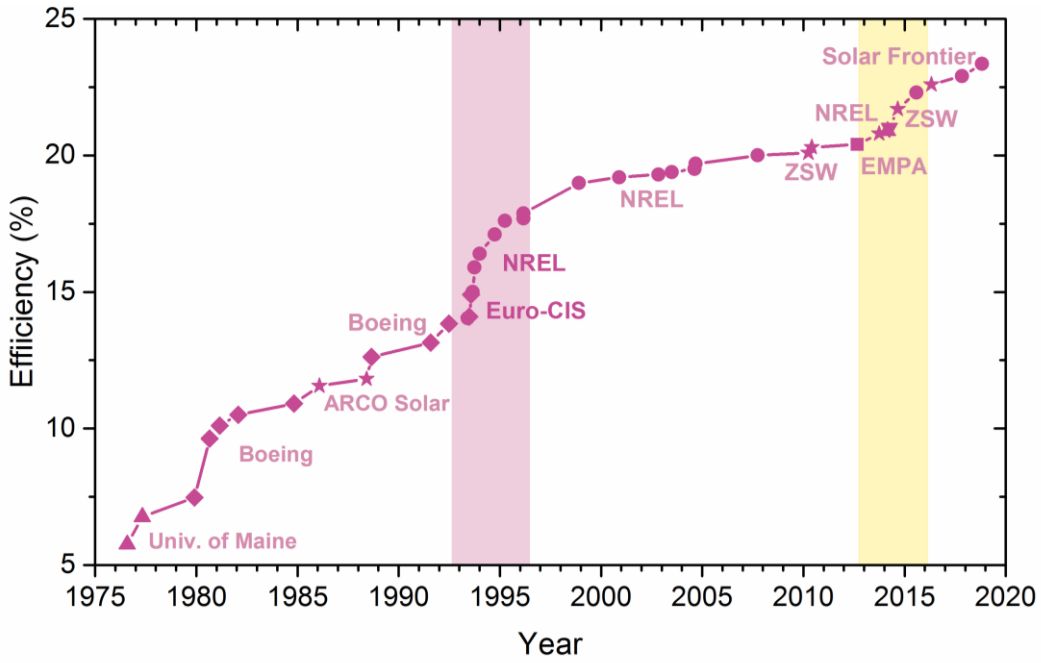

Figure 5.1 Evolution of CIGS best research cell efficiencies. Graph based on [91], data taken from NREL [94]. Shaded regions correspond to leaps in efficiency caused by sodium doping (purple) and heavy-alkali introduction (yellow shading).

5.1 Sodium

From the early 1990's, when the beneficial effect of sodium on the efficiency of CIGS solar cells has been observed for the first time [21, 89, 90], sodium has been a crucial part of highly efficient CIGS solar cells. In this chapter, methods of sodium incorporation, its location and the various effects it has on CIGS materials will be described.

5.1.1 Methods of sodium incorporation and concentration control

The oldest, and most widely used method of sodium incorporation into the CIGS layer is by preparing the cells on top of standard soda-lime glass substrates [95, 96]. Then, during the evaporation process, elevated temperatures lead to the diffusion of the Na ions through the molybdenum back contact and into the absorber. It is the cheapest and the easiest method, however not devoid of its problems: it makes precise control of sodium concentration impossible, and some of it might even diffuse later, during the cell's operation. This is especially important, as elevated sodium concentration could influence the potential-induced degradation (PID)[95, 97]. Moreover, this approach would not work on sodium-free substrates such as polymer or steel foils. To mitigate that alternative sodium incorporation methods were developed over the years that can be used both on rigid, Na-free substrates such as borosilicate glass (BSG, i.e. Corning 7059 [98]) ceramics (Al_2O_3 [22, 99], ZrO_2) or SLG covered with diffusion barriers such as SiO_2, Si(N,O) or Al_2O_3[22]. Those include, but are not limited to:

- **Sodium-containing precursors**, deposited on top of the molybdenum layer before the deposition of CIGS, such as thin alkali-doped silicate layers (thin layers of SLG) [25], NaF layers [22, 32, 95, 100, 101], or atomic sodium being incorporated into the molybdenum layer in the form of Mo:Na or Mo:Na sandwiched with Mo [98, 102, 103]. This allows growth of the CIGS layer in the presence of sodium, much like on top of SLG, but with better concentration control.
- **Incorporation of sodium during CIGS growth**, where NaF is co-evaporated during absorber growth, typically during one of the stages in a three-stage process [62, 104].
- **Post-deposition treatments**, in which a thin alkali layer, most often NaF of KF (sometimes also RbF or CsF), is deposited on top of the absorber and annealed [105–110]. As the alkali residue is then removed before the CdS deposition, the concentration of alkalis can be controlled through both the layer thickness and annealing temperature.

This type of methods limit the impact of alkali metals on the morphology of absorber, and as such are particularly useful in research.

Sometimes multiple methods are used on the same cell. A typical example would be KF-PDT on samples prepared on soda-lime glass to achieve mixed Na and K doping, or PDT with both NaF and KF [108, 110, 111].

5.1.2 Location of sodium and its typical concentrations

The concentration of sodium in typical CIGS solar cells prepared on SLG, including commercial ones, is normally equal to about 500-600pm [112–114]. In cells prepared on nominally alkali-free substrates, such as BSG, steel or polyimide, the values are much lower, typically in the range on single ppm [101, 112, 114]. Sodium incorporation techniques allow for concentrations from single ppm up to over a thousand, depending on the incorporation method [114–116].

Sodium, however, is not distributed uniformly across the entire absorber. First of all, secondary ion mas spectroscopy (SIMS) measurements showed an increase in Na concentration at the front and back contacts, especially at the CIGS/CdS interface [117, 118]. This may be due to the increased concentration of grain boundaries in those regions, as sodium is heavily segregated at those [114, 119–122]. Atom probe tomography (APT) results on SLG-based devices indicate Na concentration of about 0.5-1.5at% at the GBs [123, 124], as compared to 20-80ppm in the grain interior [121–123, 125]. Additionally, Na was found to form small clusters in the grain interior, with local concentrations reaching up to 14at% [114, 121].

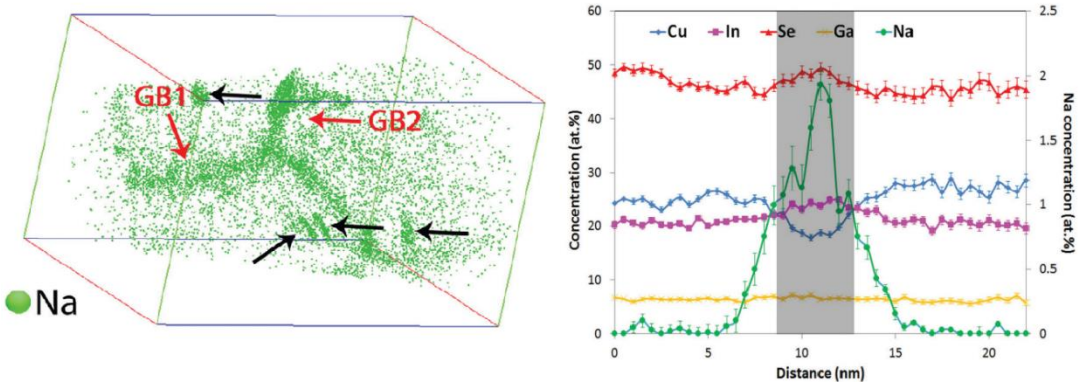

Figure 5.2 Left: an example of a 3D atomic probe tomography image showing Na enrichment on grain boundaries (red arrows) and in-grain clusters (black arrows). Right: concentration of elements across a GB extracted from APT measurements with visible Na enrichment. Both pictures were taken from Choi et al. [114]

5.1.3 The effect of sodium incorporation

The most visible effect of sodium incorporation, and the one which caused the widespread use of SLG substrates is that it causes an increase in efficiency, up to double that of the Na-free cells [21, 89, 105, 126–128]. This is caused mostly by an improvement in the FF and the V_{OC} [96, 105, 124, 128], with no significant impact on the J_{SC}. The improvement of the V_{OC} is linked to the increased hole concentration in the alkali-treated absorbers as measured by CV and DLCP – from about $10^{14}cm^{-3}$ in the alkali-free cells up to $10^{16}cm^{-3}$ [62, 105, 127, 129] in the sodium-rich ones. However, the increase in free hole concentration by itself is not enough to explain the total increase in V_{OC}, therefore it is likely that Na also promotes passivation of the interfaces/grain boundaries and suppresses recombination (especially visible in combined treatment with KF) [111, 126]. In thin films, the effect of sodium is observed mostly as an increase in conductivity [96, 112, 130].

There is an optimum amount of sodium in the CIGS layer and larger doses of Na can be detrimental to device performance [131, 132], mostly in terms of reduced J_{SC} and FF due to an increase in shunt-related losses [133, 134]. Additionally, samples with excess sodium might be prone to delamination from Mo layer.

5.2 Potassium

After the discovery of the beneficial effect of sodium on the CIGS cells and the development of post-deposition treatments, heavier alkali metals, such as potassium, cesium and rubidium were investigated, typically simultaneously with Na treatment. This resulted in a further improvement of the device efficiency. In this chapter I will focus on the effect of potassium-PDT, omitting the effects of heavy alkali doping.

5.2.1 Location of potassium and ion-exchange mechanism

Similar to sodium, potassium is mostly located at the grain boundaries, with very small concentration visible in the grain interior, but the segregation is even more pronounced than in case of Na [135]. Typical concentrations at the grain boundaries reach about 0.3at%. Additionally, the concentration of K at the CIGS/CdS interface is higher than in case of sodium [136]. Just like with sodium, the concentration of potassium during PDT can be achieved by adjusting the annealing temperature, but the same PDT temperature will result in a much higher concentration of K than Na [127].

A commonly observed phenomenon in cells treated with both sodium (be in from PDT or the substrate) and with heavier alkali metals, such as potassium, is the so-called ion exchange mechanism. It's principle is that the lighter ions get misplaced by the heavier ones, for instance Na by K [108, 121, 135], and the resulting lighter ion concentration is considerably lower than in cells with only the light ion treatment, possibly due to washing away during the CdS bath [137, 138].

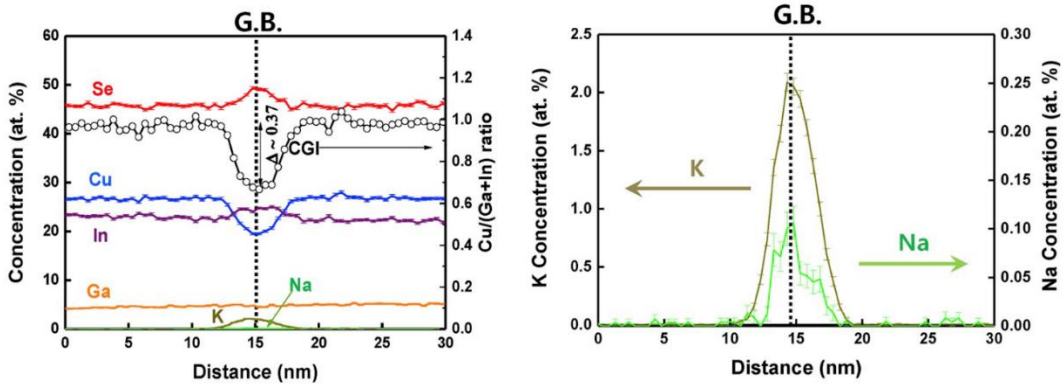

Figure 5.3 Left: concentration of elements across a GB extracted from APT measurements with visible Cu depletion and alkali enrichment. Right: the same picture scaled to show Na and K concentration across the GB. Both pictures were taken from Kim et al. [121]

5.2.2 The beneficial and detrimental effects of potassium incorporation

The beneficial role of the potassium-PDT is similar to the one of sodium. Devices treated with potassium exhibit increased free hole concentration [99, 107] just like those treated with sodium. However, most of the reported studies focus only on samples treated with both sodium and potassium at the same time. In those solar cells, higher V_{OC} than in the pure NaF-treated cells was observed, while the reports on the impact on fill factor or the J_{SC} vary [99, 108, 110].

What is different between the impact of sodium and potassium is that the only negative effects of Na were observed for its very high concentrations, while in case of K the effects are not as straightforward. When low doses of potassium were used together with sodium, for instance through subsequent NaF-PDT and KF-PDT, the resulting efficiency [138] and hole concentrations [107, 132] were reduced with regards to pure NaF-PDT (but still higher than in alkali-free devices). Once sufficiently large amounts of potassium were used this effect was no longer observed [132]. When KF-PDT was made on cells on SLG substrates with SiO_2 barrier or alumina, namely cells with very low initial alkali content, the V_{OC}, FF and overall efficiency were increased, but the J_{SC} was reduced compared to the alkali-free device [99, 139, 140].

5.2.3 Postulated models of alkali operation

When the beneficial effect of sodium was first observed, it was thought to cause change through morphological changes, as samples grown on Na-containing substrates (i.e. SLG) or on top of precursor layers typically have better morphology and bigger grains [21]. However, the improvement is also seen in samples which were subjected to PDTs, so while improved crystallinity may play a role in the beneficial effect of Na, it is not enough to explain it. Since then, the following models were proposed:

- **Elimination of the compensating donor In_{Cu} with Na_{Cu}** [130]**.** Na_{Cu} is electrically inactive, so this would lead to an enhanced p-type doping. This would explain why the Cu-poor devices benefit more from the Na-doping [141]. An argument for this model is the low formation energy of Na_{Cu} – calculations show Na_{Cu} to be the most probable Na location in CIS [142–144]. This however, could be a double-edged sword, as after filling the available In_{Cu} sites, Na_{Cu} could start replacing the V_{Cu} acceptors [141].

- **p-type enhancement through fast diffusion of Na** into the grains at high temperatures through occupation of Cu-sites, followed by fast outdiffusion at lower temperatures (during cool down) leaving enhanced number of Cu vacancies behind [142]. This model should work for alkali doping during growth of CIGS at high temperatures, but it is hard to apply to PDT-treated cells.
- **Oxygen model**, in which Na catalyzes the formation of neutral O_{Se} instead of donor V_{Se} at GBs [141, 145, 146]. V_{Se}, being a donor, could lead to a type inversion at grain boundaries, reducing the average hole concentration throughout the absorber, while at the same time could also act as a trap [146]. The reasoning behind it is that annealing in oxygen atmosphere yields somewhat similar results to sodium treatment [96], Na seems to be correlated with O on the CIGS surface [24, 96, 146], both tend to be segregated at grain boundaries, and lastly, sodium in known for its oxidating properties. However, measurements by Raghuwanshi et al. suggest oxygen to be linked to detrimental, rather than neutral GBs [56].
- **Passivation of the grain boundaries** positively charged donor atoms at the GBs could acts as hole barriers, impeding the hole transport across GBs, as well as cause carrier depletion stretching far into the grain interior [62]. Additionally, those donors could act as recombination centers, increasing recombination and reducing the V_{OC} and FF [61]. Passivation of donors at the GBs – i.e. In_{Cu} – by sodium would mitigate those effects.

Although the effects of potassium incorporation are similar to those its sodium, its location in the cell and the coexistence of both positive and detrimental effect suggests further possible explanations:

- **Improvement of junction properties**. KF-PDT was found to result in the depletion of Cu and Ga at the top surface of absorbers [108, 147], which in turn can lead to the lowering of the VBM and widening of the bandgap at the CdS/CIGS interface, potentially due to the formation of a K-In-Se phase [148, 149]. Additionally, the depletion of Cu together with the reported enrichment in Cd [108, 135] may lead to the creation of shallow donors Cd_{Cu} at the interface, causing a type inversion [107]. Either of those effects would result in an improvement of charge carrier separation at the interface and inhibit recombination, and as such increase the junction quality [150]. To that explanation points the increase of the V_{OC} upon the KF treatment, which is higher than expected for the reported increase in free hole concentration [107].

- **Grain boundary passivation** [99]. Similar to sodium, potassium is located mostly at the grain boundaries, and similar to Na is thought to be able to catalyze the oxidation of V_{Se} donors into neutral O_{Se} [138]. Also, KPFM measurements showed reduced potential fluctuations at the GBs in KF-treated cells, pointing to GB passivation [150].

6 Motivation

The beneficial effect of alkali incorporation into the CIGS absorbers has been known since the 1990's, but the precise mechanism is still under debate. Although a lot of research has been done in this subject, most of it focuses simply on the comparison between alkali-free and alkali-rich devices or differences between alkali-doped cells prepared with different methods, without a systematic study looking deeper into the correlation between alkali concentration and changes induced in the electrical characteristics. There are some studies, in which sodium concentration was varied between a wider set of devices, however almost all of those concern sodium incorporation from the substrate or precursor [98, 101, 112, 115]. As sodium can act also on the morphology of the absorber during growth, it makes the insight into the purely electrical impact not straightforward. In order to mitigate that, sodium supply through a post-deposition treatment which does not introduce changes in crystallinity and morphology of CIGS absorbers, would be preferable. As it is postulated that sodium and potassium could impact the CIGS performance through similar pathways, it is important to study the similarities and differences between sodium- and potassium doped devices. However, most of the available data is focused on the comparison of the impact of sodium and combined sodium and potassium treatment, without studying the pure-K doping. This is important, as combined treatment leads to the best results, but makes the distinction between the alkali effects harder if not impossible.

Most studies focus on either solar cells or thin films. As the two incorporate the same absorber, but different interfaces (i.e. CIGS/CdS in cells vs CIGS/Au in thin films) comparison between those will give insight into which effects are linked to the absorber itself, and which are linked to the interfaces. Additionally, as the grains are columnar in shape, the difference in transport in the planar (thin films) and vertical (cells) direction may highlight the impact of grain boundaries. Moreover, the electric field distribution is different in cells and thin films.

A similar story can be told about the metastable properties of CIGS cells with regards to alkali doping. These are typically studied on a very narrow range of devices, often either alkali-free or sodium-rich. There are a few reports of alkali doping and persistent photoconductivity being researched together[70, 80], but the available data is focused only on Na-free – Na-rich pairs, with no systematic studies across various sodium concentrations, or substrate types.

In this work, I want to present a systematic study of the effects of sodium and potassium doping on the relaxed and metastable properties of CIGS thin films and solar cells.

This study is primarily aimed on answering the following questions:

- is the dominant alkali activity tied to the volume of the grains or to grain boundaries;
- does it affect mobility and/or concentration of free carriers;
- and does it create deep defects associated with metastability?

For the main part of this study the single-stage coevaporation processed devices were chosen, as it allows for the greatest stoichiometry uniformity. The single-stage devices were prepared by ZSW on both SLG/SiO_xN_y and ZrO_2 substrates to study whether the morphology of the substrate and the miniscule amounts of sodium diffusing through the SiO_xN_y barrier during growth will have an impact on the resulting CIGS thin film. Post-deposition treatment with NaF and KF was chosen as a method of controlled introduction of alkali metals as it does not influence the morphology of the absorber because it is done after absorber deposition and at lower temperatures. This way the resulting alkali concentration can be adjusted in a range spanning 3 orders of magnitude.

Single-stage absorbers, however, have two major drawbacks –the grain size is reduced as compared to the three-stage process, and the efficiency of resulting cells is lower. A series of devices made using 3-stage process was therefore studied in order to examine to what extent the process type is important in the context of alkali doping. Finally, changes due to different copper content or annealing in the selenium atmosphere were investigated to narrow down the possible routes in which sample variation could influence the results.

All samples investigated in this work were prepared at ZSW in the framework of Beethoven II project. Structural and compositional characterization together with standard J-V characterization of solar cells was also performed at ZSW.

7 Methods

7.1 Conductivity as a function of temperature

The DC conductivity can be measured by applying voltage to a device of known dimensions and recording the current response:

$$\sigma = \frac{d}{S}\frac{I}{V} \tag{13}$$

where d represents the distance between the electrodes and S is the cross-section of the device.

In a p-type semiconductor, the conductivity σ can be described as:

$$\sigma = pq\mu \tag{14}$$

where p is the free hole concentration, q is the carrier charge and μ is the hole mobility. As the measurement is made as a function of temperature, the dependence of the product of carrier concentration and mobility on temperature can be obtained.

The mobility of charge carriers in a given semiconductor is linked to the types of scattering or trapping taking place, including [151–153]:

scattering on acoustic phonons	$\mu_{ap} \sim T^{-3/2}$	(15)
ionized impurity scattering	$\mu_{ion} \sim T^{3/2}$	(16)
scattering on dislocations	$\mu_{dis} \sim T$	(17)
scattering on grain boundaries	$\mu_{GB} \sim T^{1/2} \exp\left(-E_B/k_B T\right)$	(18)
trapping at defects	$\mu_{trap} \sim \exp\left(-\Delta E_{trap}/k_B T\right)$	(19)

As the resulting mobility follows the relation:

$$\frac{1}{\mu} = \sum \frac{1}{\mu_i} \tag{20}$$

the process with the lowest mobility limits the overall mobility in the material. As such, scattering on acoustic phonons is typically the dominant mechanism limiting the mobility in

single-crystal semiconductors at higher temperatures, while scattering on ionized impurities dominates in the low-temperature region. In polycrystalline materials, grain boundaries may influence greatly the overall mobility [154].

Theoretically, in the temperature range coved by our measurements, the free hole concentration in a doped semiconductor should follow the relations:

moderate temperature (saturation range) $$p = N_A \quad (21)$$

low temperature (freeze-out) $$p = \sqrt{N_V N_A} e^{-E_{ac}/k_B T} \quad (22)$$

where E_{ac} is the position of the acceptor level with regards to the valence band edge and k_B is the Boltzmann constant. As the σ(T) relation is typically presented as an Arrhenius plot ln(σ) vs 1/T, the slope of the obtained relation should be 0 in the saturation range and $-E_{ac}/k_BT$ in the freeze-out range.

7.2 Capacitance-Voltage Measurements (CV)

Capacitance-voltage measurements are a common way of measuring free carrier concentrations in semiconductor junctions. CV use is, however, limited only to asymmetric junctions – this is those, which have one side doped considerably higher than the other. Then, the space-charge region (SCR) stretches to the lower-doped side only. In our case we will consider a n^+p device, where the CIGS absorber is the p-type and CdS is the n^+. Then, the SCR width stretches into the CIGS layer and its width W is equal to:

$$W = \sqrt{\frac{2\varepsilon_r \varepsilon_0 (V_{diff} - V)}{e} \frac{(N_A + N_D)}{(N_A N_D)}} \quad (23)$$

where V_{diff} is the diffusion potential, V is the applied voltage, ε_r is the relative dielectric constant of CIGS, and N_A and N_D are concentrations of acceptors and donors respectively. In a n^+p junction, $N_D >> N_A$, and equation (23) can be simplified to:

$$W_p = \sqrt{\frac{2\varepsilon_r \varepsilon_0 (V_{diff} - V)}{e N_A}} \quad (24)$$

As can be seen in (24), the one-sided junction width is a function of applied bias and the doping density (mostly) on the lower-doped side. Through applying an electric field to a device, the width of the SCR can be decreased (forward bias) or increased (reverse bias). If we then think of the sample as a capacitor, then by changing the W, which would then correspond to the distance between the capacitor terminals, the capacitance C will be affected:

$$C = \frac{\varepsilon_r \varepsilon_0 A}{W} \tag{25}$$

where A is the surface area of the device. If we then introduce a small AC voltage, the capacitive response can be rewritten as:

$$C = \frac{dQ}{dV} \tag{26}$$

As charge is here equal to the product of the density of ionized acceptors N_A, their charge and the volume, relation (26) can be rewritten as:

$$C = qAN_A \frac{dW}{dV} \tag{27}$$

By differentiation of equation (27) with regards to voltage we get:

$$\frac{dC}{dV} = \frac{-\varepsilon_r \varepsilon_0 A}{W^2} \frac{dW}{dV} \tag{28}$$

Then, by combining equations (27) and (28), the change in capacitance after a change in bias can be defined as:

$$\frac{dC}{dV} = \frac{-\varepsilon_r \varepsilon_0}{W^2} \frac{C}{qN_A} \tag{29}$$

This relation is the basis of the CV measurement – by applying a combined DC offset bias and smaller, fixed amplitude AC voltage on top of it, it allows for the probing of free carrier

concentration as a function of distance from the junction (equation (30)). In CV, the AC modulation (dV in equation (29)) is responsible for the determination of charge carrier density by causing a capacitive response, while the varied offset bias (V in formula (24)) allows for probing as a function of distance, influencing the SCR width W, as the majority of the signal comes from the edge of the SCR [69]:

$$N_A(W) = -\frac{C^3}{q\varepsilon A^2\left(\frac{dC}{dV}\right)} = -\frac{2}{q\varepsilon A^2}\left[\frac{d\left(\frac{1}{C^2}\right)}{dV}\right]^{-1} \quad (30)$$

where W can be calculated from the capacitance as:

$$W = \frac{\varepsilon_r \varepsilon_0 A}{C} \quad (31)$$

In most cases, the resulting doping profile is the one of the free charge carriers. However, this method is strongly influenced by interface states, as well as slow-responding defects.

7.3 Drive Level Capacitance Profiling (DLCP)

Drive Level Capacitance Profiling is a modified version of CV developed by Michelson and Gelatos in the 1980's [155]. Contrary to CV, it is insensitive to surface & interface states, therefore comparing CV and DLCP measurements on the same device may give insight into the bulk and interface response.

In CV, an AC voltage is applied on top of a DC bias, and the AC amplitude dV is kept constant while the DC bias is varied. In DLCP however, the AC drive voltage amplitude is swept over each DC bias, while adding a small DC offset so that the maximum forward voltage is kept constant with increasing amplitude [69, 155]. Typically, a series of measurements are made with increasing temperature, and the frequency of applied bias is selected according to device properties and the desired result – doping density (high frequency, 100kHz-1MHz) or defect response (low frequency). For each (angular) frequency of AC bias and temperature pair there is a specific limiting energy E_e (equation (32)). In a p-type material only the gap states below E_e can follow the changes in applied AC bias and contribute to the capacitance [155]:

$$E_e = -kTln\left(\frac{\omega}{2\pi\nu_0 T^2}\right) \quad (32)$$

where υ is the thermal emission prefactor $\nu_0 = N_v(T) < v > \sigma_h$, and reflects the effective DOS in the valence band N_V, average thermal velocity <v> and a capture cross section σ_h. Due to the band bending at the junction, the crossing point between the E_e and the Fermi level will be linked to a spatial position x_e. Close to the interface, where $x<x_e$ the Fermi energy E_F is below E_E, and the states respond slower than the applied bias, not contributing to the response. At

$x=x_e$, gap states between E_V and E_F (including shallow dopants) will respond at AC frequency, and beyond x_e – much faster than the modulation.

In CV, the applied AC perturbation was small enough so the capacitance could be described as:

$$C_0 = \frac{\varepsilon_r \varepsilon_0 A \rho_e}{\varepsilon_r \varepsilon_0 F_e + x_e \rho_e} \tag{33}$$

where x_e is the spatial distance from junction, F_e is the electric field, and ρ_e is the charge density.

In DLCP, an increase in the AC amplitude calls for the use of the higher orders of correction to junction capacitance:

$$C = \frac{dQ}{dV} = C_0 + C_1 dV + C_2 (dV)^2 + \cdots \tag{34}$$

where:

$$C_1 = -\frac{0.5\ \varepsilon_r \varepsilon_0 A \rho_e^2}{(\varepsilon_r \varepsilon_0 F_e + x_e \rho_e)^3} \tag{35}$$

From this, the spatial doping profile can be calculated as the carrier density N_{DL}:

$$N_{DL} = \frac{\rho_e}{q} = -\frac{C_0^3}{2q \varepsilon_r \varepsilon_0 A^2 C_1} \tag{36}$$

as a function of the distance from the junction W:

$$W = \frac{\varepsilon_r \varepsilon_0 A}{C_0} \tag{37}$$

In practice, the only parameters we needed is the dielectric constant ε_R and sample area. Measuring it correctly is crucial for the obtained carrier density.

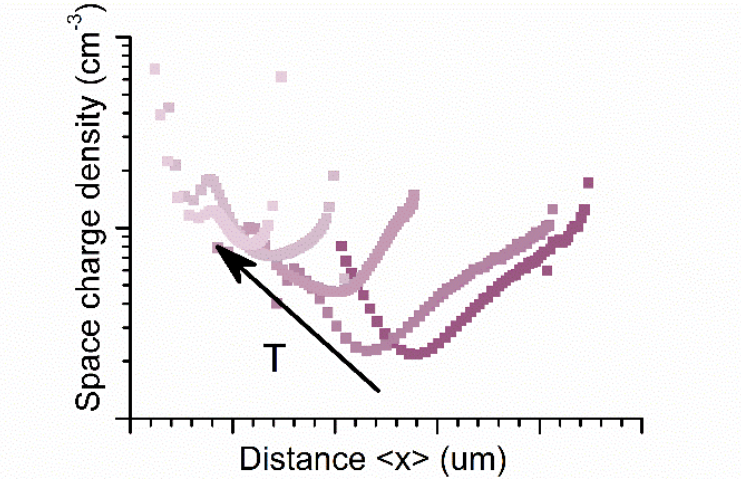

Figure 7.1 An example of a series of DLCP measurements taken at different temperatures.

7.4 Current-voltage characterization as a function of temperature

By performing a series of current-voltage measurements and plotting the V_{OC} as a function of temperature for a given illumination intensity, one can get a closer look into the recombination mechanisms. In a solar cell, the open circuit voltage V_{OC} follows the relation:

$$V_{OC} = \frac{E_a}{q} - \frac{Ak_BT}{q} ln\left(\frac{J_{00}}{J_{SC}}\right) \quad (38)$$

where A is the ideality factor and E_a is the activation energy, and J_{00} is the time-independent part of the diode saturation current density J_0:

$$J_0 = J_{00} \exp\left(\frac{-E_a}{k_BT}\right) \quad (39)$$

In order to maximize the efficiency of a solar cell, it is important for the diode saturation current density J_0 to be as low as possible. In a p-type material, assuming recombination in the SCR J_{00} can be expressed as [14]:

$$J_{00} = \frac{qD_nN_CN_V}{N_AL_D} \quad (40)$$

Where D_n is the diffusion constant of electrons, and L_D is the diffusion length of electrons. In order for the J_0 to be low, the doping density and minority carrier lifetime have to be high. In order to maximize carrier lifetimes, unwanted recombination should be suppressed.

By extrapolating the V_{OC}(T) relation to 0K, the activation energy and through that, the type of dominating recombination mechanism may be assessed[42]:

$$V_{OC}(T = 0K) = \frac{E_a}{e} \quad (41)$$

where E_a will be equal to E_g for recombination in the space charge region or in the bulk of absorber, and may be reduced in case of recombination at the interface.

8 Experimental

8.1 Sample preparation

All samples and SIMS measurements were made by members of the group of dr. Roland Wuerz at ZSW, primarily by Alexander Eslam.

Series	Batch	Process	Cell	Thin film
SLG-1st	1st	1-stage	SLG/SiO_xN_y/Mo/Cu(In,Ga)Se_2/ CdS/ ZnO/ZnO:Al/Ni/Al/Ni	SLG/SiO_xN_y/Cu(In,Ga)Se_2/Au
ZrO_2-1st	2nd	1-stage	ZrO_2/Mo/Cu(In,Ga)Se_2/ CdS/ZnO/ZnO:Al/Ni/Al/Ni	ZrO_2/Cu(In,Ga)Se_2/Au
ZrO_2-3st	3rd	3-stage	ZrO_2/Mo/Cu(In,Ga)Se_2/ CdS/ZnO/ZnO:Al/Ni/Al/Ni	ZrO_2/Cu(In,Ga)Se_2/Au
Cu-series	4th	1-stage	ZrO_2/Mo/Cu(In,Ga)Se_2/ CdS/ZnO/ZnO:Al/Ni/Al/Ni	ZrO_2/Cu(In,Ga)Se_2/Au
Large-grained	5th	3-stage	ZrO_2/Mo/Cu(In,Ga)Se_2/ CdS/ZnO/ZnO:Al/Ni/Al/Ni	ZrO_2/Cu(In,Ga)Se_2/Au

Table 1. List of the measured CIGS solar cell and thin film series.

In each case absorbers for solar cells and thin films were prepared in the same run

Substrates

Solar cells and thin films were prepared on two types of substrates:

- **SLG/SiO_xN_y** 2mm-thick soda-lime glass (SLG) substrate covered with a 160nm thick SiO_xN_y barrier layer made by reactive sputtering
- **ZrO_2** zirconia substrates

In all cases, half of the substrates – future cells – were covered with a DC sputtered 550nm Mo layer, half were left as is for planar devices.

CIGS layer

- **Single-stage** A 2µm thick layer of Cu(In,Ga)Se_2 was coevaporated in a single-stage process in an Octoplus 500 growth chamber using MBE components, with a nominal substrate temperature of about 450°C
- **Three-stage** devices were prepared in the same setup using a three-stage protocol at a substrate temperature of about 600°C

Post-deposition treatment

After absorber/thin film evaporation and subsequent cooling, NaF/KF layers were evaporated with a rate of about 0.3 Å/s under low Se flux (about 2 Å/s) for 20 min (unless otherwise specified). The final alkali concentration controlled by adjusting the substrate temperature during the PDT (T_{PDT}), between 110 and 400°C (no PDT was used on reference devices). Samples denoted with Se-PDT were annealed under Se-flux without prior alkali evaporation.

Cells

After PDT, CIGS layers prepared on Mo-coated substrates were rinsed to remove NaF residue, and covered with 60nm CBD CdS layer, 80nm RF-sputtered ZnO, 350nm sputtered ZnO:Al. The top electrode was made from Ni/Al/Ni using a shadow mask, without AR coating. Complete cells had an area of about 0.5 cm^2. For DLCP measurements a smaller part of the sample was defined using mechanical scribing.

Planar devices

Absorbers were etched in 10% HCl to remove excess NaF and etched in KCN to remove oxidation from the surface. Two Au contacts of 160nm thickness, 1mm separation were deposited using a mask.

Figure 8.1 Photographs of devices on ZrO_2 used in this study. Left – solar cell used for DLCP measurement, with active surface reduced through mechanical scribing. Middle – thin film used for conductivity measurements, with measured area defined by mechanical scribing (rectangle in the top of the device). Right – 50mm^2 solar cell used for STC JV measurements by ZSW.

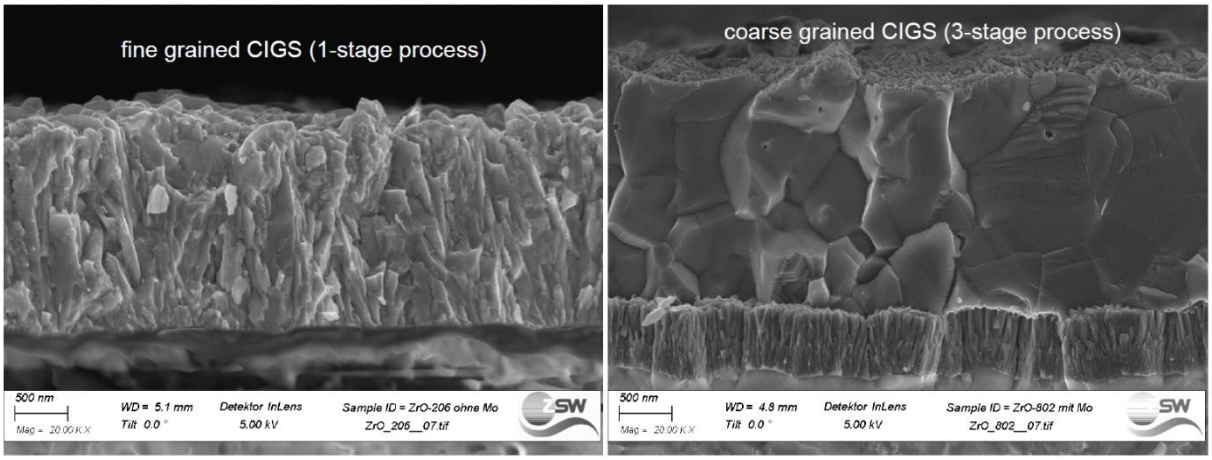

Figure 8.2 SEM cross-section images of single-stage (left) and three-stage (right) solar cells before deposition of CdS.

Average grain size was estimated to be roughly 250x250x750nm in case of single-stage CIGS and about 500x500x1250nm in case of three-stage CIGS.

8.2 Alkali concentration values and photovoltaic parameters of investigated devices

Alkali concentration in the cells and thin films was measured by Alexander Eslam at ZSW by Time of Flight Secondary Ion Mass Spectrometry using a TOF.SIMS 5 instrument from IONTOF, allowing for the detection of alkali elements down to lower region of ppm. As sputter source an oxygen ion beam was used over an area of 130 × 130 μm². The analyzer beam was a Bi^+ beam, over a smaller area of 50 × 50 μm². Calibration was done with alkali-free CIGS devices implanted with ^{23}Na (dose =1.2×10^{14} cm^{-2}) and ^{39}K (dose =1.6×10^{14} cm^{-2}) to calculate absolute values of alkali concentration. To avoid surface artefacts, the value of alkali concentration is taken as a mean from 0.2 to 1.6 μm depth. The CGI (Cu/(Ga+In)) and GGI (Ga/Ga+In)) ratios were measured using X-ray Fluorescence Spectrometry (XRF).

All standard testing condition (STC) current-voltage, SIMS and XRF measurements were performed by ZSW

SLG – single stage, 1st batch

General		Planar		Cells						Composition	
PDT	PDT-T [°C]	c(Na) [ppm]	c(K) [ppm]	c(Na) [ppm]	c(K) [ppm]	PCE [%]	V_{OC} [mV]	FF [%]	J_{SC} [mAcm^{-2}]	CGI	GGI
x	**25**	**7**	**-**	**22**	**-**	**9.4**	**545**	**60.1**	**28.8**	**0.80**	**0.31**
Se	**340**	<0.1	-	2	-	9.8	553	59.8	29.5	0.81	0.29
NaF	110	52	-	77	-	9.9	553	63.2	28.5	0.80	0.30
NaF	150	88	-	190	-	12.0	588	72.1	28.4	0.83	0.31
NaF	190	167	-	261	-	12.8	613	73.7	28.5	0.80	0.31
NaF	250	474	-	504	-	15.1	654	77.7	29.9	0.80	0.31
NaF	340	534	-	473	-	16.1	673	78.3	30.6	0.80	0.29
NaF	400	927	-	-	-	-	-	-	-		

Table 2. Chemical composition and photovoltaic parameters of single-stage solar cells and thin films prepared on SLG/SiO_xN_y substrates. Batch subjected to NaF-PDT, x denotes devices without PDT, Se – devices which underwent PDT procedure, but without alkali deposition.

Values of c(K) were not measured. For NaF-PDT at 400°C only a planar device was provided, as the CIGS layer peeled off during the chemical bath deposition of CdS.

ZrO_2 – single stage, 2nd batch

General		Planar		Cells						Composition	
PDT	PDT-T [°C]	c(Na) [ppm]	c(K) [ppm]	c(Na) [ppm]	c(K) [ppm]	PCE [%]	V_{OC} [mV]	FF [%]	J_{SC} [mAcm^{-2}]	CGI	GGI
NaF	101	67	4	67	0.9	10.0	539	62.3	29.9	0.81	0.29
NaF	131	114	0.45	93	0.5	11.8	573	70.0	29.4	0.81	0.28
NaF	153	135	1.6	161	0.6	11.8	584	71.6	28.3	0.80	0.29
NaF	198	280	1.5	408	1.2	12.9	611	73.9	28.6	0.77	0.33
NaF	250	513	1.4	553	1.2	14.6	642	76.9	29.5	0.78	0.33
NaF	275	-	-	648	3	14.6	650	76.5	29.4	0.78	0.33
NaF	314	957	4.2	619	3	15.2	648	77.7	30.3	0.79	0.29
x	**25**	**15**	**1.2**	**0.17**	**0.72**	**9.9**	**547**	**60.3**	**30.0**	**0.82**	**0.29**
KF	105	44	133	2.7	237	0.9	266	22.5	15.1	0.81	0.29
KF	130	16	245	5.5	488	4.0	384	39.0	26.5	0.81	0.28
KF	191	79	755	16	1076	13.5	636	68.4	31.1	0.81	0.29
KF	247	63	1703	22	1606	13.9	625	71.7	31.0	0.81	0.28
KF	315	47	2219	30	1508	14.2	618	75.5	30.4	0.81	0.28

Table 3. Chemical composition and photovoltaic parameters of single-stage solar cells and thin films prepared on ZrO_2 substrates. Batch subjected to NaF-PDT and KF-PDT, x denotes devices without PDT

ZrO_2 - 3stage, 3rd batch

General		Planar		Cells						Composition	
PDT	PDT-T [°C]	c(Na) [ppm]	c(K) [ppm]	c(Na) [ppm]	c(K) [ppm]	PCE [%]	V_{OC} [mV]	FF [%]	J_{SC} [mAcm^{-2}]	CGI	GGI
NaF	126	46	1.9	33.7	0.04	11.1	555	65.2	30.8	-	-
NaF	147	66	2.1	65	0.1	11.7	563	68	30.7	-	-
NaF	197	144	1.2	114	0.15	12.5	584	69.5	30.7	-	-
NaF	250	186	2.1	166	0.3	13.0	600	70.5	30.6	-	-
NaF	341	232	2.5	288	2.8	13.4	607	70.9	31.2	-	-
x	**25**	**17**	**1.4**	**5**	**0.3**	**10.3**	**548**	**60.0**	**31.4**	-	-
Se	**150**	**0.8**	**0.55**	**0.02**	**0.35**	**11.6**	**551**	**66.3**	**31.8**	-	-
KF	130	0.9	39	0.4	180	3.0	378	31.0	25.4	-	-
KF	200	0.6	225	1.7	195	13.3	610	67.6	32.3	-	-
KF	350	4.7	606	6.3	495					-	-
KF	350	0.2	502	5.5	501					-	-

Table 4. Chemical composition and photovoltaic parameters of three-stage solar cells and thin films prepared on ZrO_2 substrates. Batch subjected to both NaF- and KF-PDT, x denotes devices without PDT, Se – devices which underwent PDT procedure, but without alkali deposition. Note the different temperature of Se-PDT as compared with the SLG batch.

Copper-series, single-stage, 4th batch

General		Planar		Cells						Composition	
PDT	PDT-T [°C]	c(Na) [ppm]	c(K) [ppm]	c(Na) [ppm]	c(K) [ppm]	PCE [%]	V_{OC} [mV]	FF [%]	J_{SC} [mAcm^{-2}]	CGI	GGI
x	x	35.7	2.4	3.0	1.7	8.5	489	58.2	29.8	74.0	-
x	x	33.0	0.9	1.6	0.8	9.0	521	57.9	29.8	79.5	-
x	**x**	**15.1**	**1.2**	**0.2**	**0.7**	**9.9**	**547**	**60.3**	**30.0**	**82.1**	-
x	x	19.8	0.6	-	-	10.0	551	60.9	30.0	86.5	-
NaF	312	801	1.6	423	6.6	15.3	669	77.6	29.4	72.9	-
NaF	314	957	4.2	619	3.1	15.3	648	77.7	30.3	78.5	-
NaF	**307**	**1040**	**4.3**	**642**	**2.1**	**15.0**	**657**	**76.7**	**27.8**	**83.0**	-
NaF	313	680	1.7	-	-	14.6	657	76.7	28.9	86.4	-

Table 5 Photovoltaic parameters and alkali concentration of single-stage devices prepared on ZrO_2 with different copper content, with and without NaF PDT. Devices with CGI used throughout the first 3 series are in bold.

Large-grained CIGS, 5th batch

General		Planar		Cells						Composition	
PDT	PDT-T [°C]	c(Na) [ppm]	c(K) [ppm]	c(Na) [ppm]	c(K) [ppm]	PCE [%]	V_{OC} [mV]	FF [%]	J_{SC} [mAcm^{-2}]	CGI	GGI
x	x	0.2	0.2	<0.1	<0.1	10.6	552	62.0	31.0	0.80	
NaF	311	0.3	259	293	0.8	12.1	588	66.6	30.8	0.80	
KF	311	145	1.6	2	355	15.1	660	74.0	31.0	0.79	

Table 6 Devices prepared on ZrO_2 using large-grained three-stage process.

8.3 Conductivity measurements

Conductivity vs temperature measurements (referred to as σ(T)) were performed on planar devices. Gold contacts were spaced by 1mm, and the measurement area was defined through mechanical scribing, by enclosing a 0.8-1.5mm wide, 4mm long part of the device (1.5mm each contact, 1mm spacing, see Figure 8.1). The total area was kept small to ensure uniform distribution of light during light-soaking procedure. Ohmicity of the contacts was checked for each sample by measuring a current-voltage curve.

Measurements were conducted using a two-point probe method in a nitrogen cryostat in vacuum (typically $5 \cdot 10^{-5}$mbar) using a custom-built set-up based on Keithley 428 current amplifier and National Instruments DAQ 6122 card, using a lock-in amplifier as a voltage source, with the temperature adjusted through a LakeShore temperature controller.

As a relaxed state we considered the state after at least 24 hours in the dark at an ambient temperature, in vacuum. The metastable state LS was achieved through illumination with a 980nm, 5mW laser (2x6mm spot size) at 300K for 30min and subsequent cooling to 100K under illumination. Light was set up by measuring the current response of a biased device (typically 0.5-1V) and adjusting for maximum current while changing the position of a laser. To ensure repeatability of the LS conditions, I tested the illumination intensity effect on the PPC magnitude on both alkali-free and alkali-rich devices and cross checked it with literature – small differences in intensity due to suboptimal light alignment, below an order of magnitude, will not affect the GT in a significant way [66].

Typical cooling time was about 20-30minutes from 300K to 90K, corresponding to an average cooling rate of 8K/min. Typical heating rate was about 3.5K/min from 100 to 200K, then 2.5K/min and down to about 1K/min for temperatures above 300K, for both relaxed and light-soaked measurements. This is a compromise between the desired heating rate of 3.5K/min for metastable effect not to relax, and the limitations of the heater. Analogically, there were multiple measurements performed on a few distinct samples to see how the cooling down or heating up speed influences the GT curves, and whether the results are congruent (they are).

As the samples show small variations over time, samples within a series were always measured in random order, so that the effect of time and the parameter measured can be distinguished.

For all devices, we observe a metastable increase in conductivity after LS, and a decrease in the slope of the σ(T) curve. For the heating rates used, relaxation of the metastable state was typically observed at about 225-250K [66, 68, 75]. In following chapters, metastable conductivity σ_{LS} and the metastable increase in conductivity $\Delta\sigma_{PPC}$ will be evaluated and compared at 200K – as it is the highest temperature before the PPC's relaxation is observed.

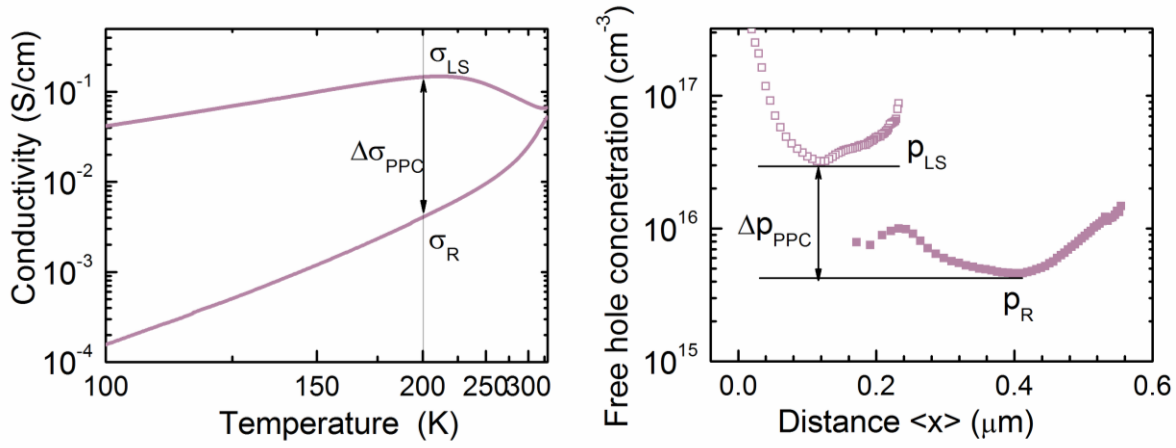

Figure 8.3 Left: an example of a σ(T) measurement result in the relaxed and light-soaked state: σ_R denotes the value of relaxed, σ_{LS} light-soaked and $\Delta\sigma_{PPC}$ a metastable increase in conductivity at 200K. Right: typical result of DLCP measurements in the relaxed (solid squares) and light-soaked state (open squares). P_R and P_{LS} denote the free hole concentration in the relaxed and light-soaked state at 200K, while Δp_{PPC} is the metastable increase in doping density.

8.4 DLCP

Drive-level capacitance profiling measurements were performed using a two-point probe method on solar cells, with the area of 3-8mm^2 defined using mechanical scribing (Figure 8.1).

Measurements were done with a HP4284A LCR meter in a He closed-cycle cryostat in vacuum during the heating ramp. The temperature was increased from 50K to 300K in 50K increments. AC frequency value was set to a value between 300kHz and 1MHz.

As a relaxed state I considered the state after at least 24 hours in the dark at an ambient temperature, in vacuum. The light-soaked state (LS) was created by illumination with a halogen lamp (1 sun) in vacuum for 30 minutes at 300 K followed by cooling down to 50 K, still under illumination.

As both deep defects and shallow dopants will contribute to the DLCP profile depending on the frequency, an Admittance Spectroscopy scan (capacitance vs frequency) was first made to find the appropriate frequency – high enough to fall below the admittance step, where only the shallow defects respond, but at the same time low enough to reduce the artifacts from i.e. cable capacitance. All hole concentration values referred to in this paper (unless specified otherwise) correspond to the minima of the DLCP curves at 200 K (see Figure 8.3). This temperature was chosen as it is the highest temperature before the metastable effects start to anneal out within the timescale of our experiment [156].

Another source of potential artifacts is in the resistance of the sample itself. As the capacitance measured is relatively small, the LCR meter is set to the Parallel Circuit Mode, where the series resistance is considered insignificant (see Figure 6-3 in the instruction manual [157]). This works well in highly doped devices or in higher temperatures. However, low-doped devices (i.e. alkali-free cells) measured at lower temperatures, for which the series resistance is not negligible, might exhibit artificially higher capacitance and as such, the reported free hole density might be substantially higher than in reality. An example of such measurement artifact can be seen in Figure 8.4. The distortion brought by series resistance, pronounced at forward bias, is also the reason why the lowest value of DLCP profile was chosen as the closest to the real free hole density (the increase observed at reverse bias is interpreted as due to the contribution of deep levels [156].

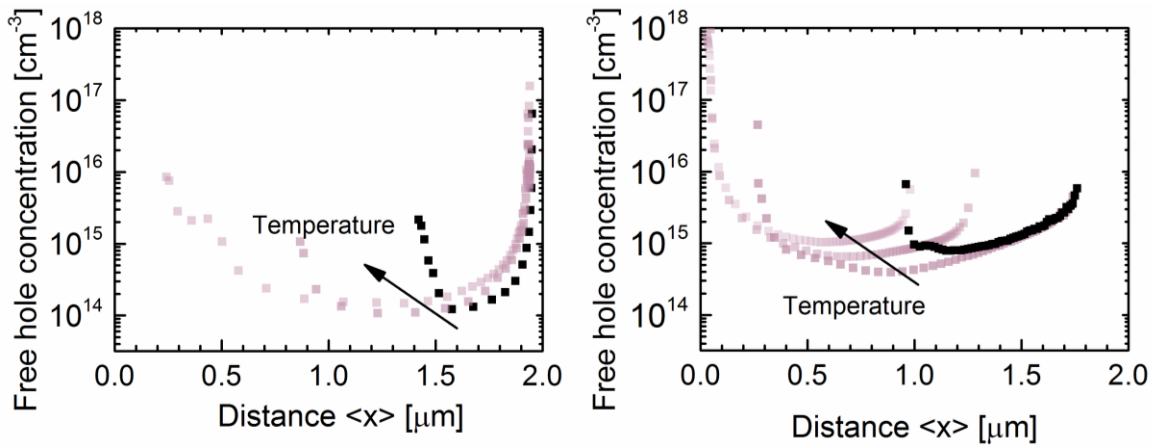

Figure 8.4 Artifacts in DLCP results. Black squares denote measurements, in which artificially high free carrier concentration was observed at low temperatures due to measurement setup constraints.

9 Results

9.1 The impact of selenium-annealing

As the PDT process takes place in selenium atmosphere, it is important to see what the annealing in selenium atmosphere itself does to the cells to exclude the possibility that the observed effects are due to selenium annealing at various temperatures rather than alkali PDT treatment. In order to see that, a thin film and a cell that were subjected to PDT treatment but without alkali layer, were analyzed. As can be seen in Figure 9.1, annealing of the SLG-series thin film in selenium atmosphere at optimum T_{PDT} (340°C) made virtually no difference to its conductivity vs temperature characteristics, so we concluded that changes in the electrical properties are due to alkali doping not an annealing effect. In DLCP, the only visible difference was observed in the metastable state, where the Se-annealed cell exhibited slightly higher metastable increase in free hole concentration.

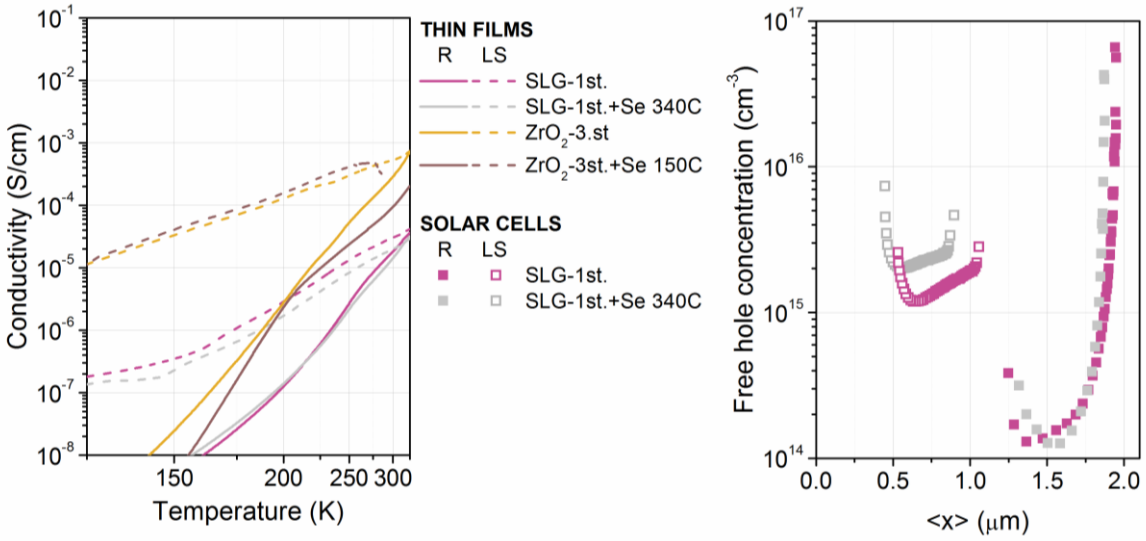

Figure 9.1 Conductivity vs temperature measurements for alkali-free devices with and without Se-PDT (left). DLCP measurement on alkali-free single-stage cells on SLG/SiO_xN_y with and without Se-PDT in the relaxed (solid) and light-soaked state (open squares).

9.2 Sodium-doped samples

9.2.1 Free hole concentration in the relaxed state

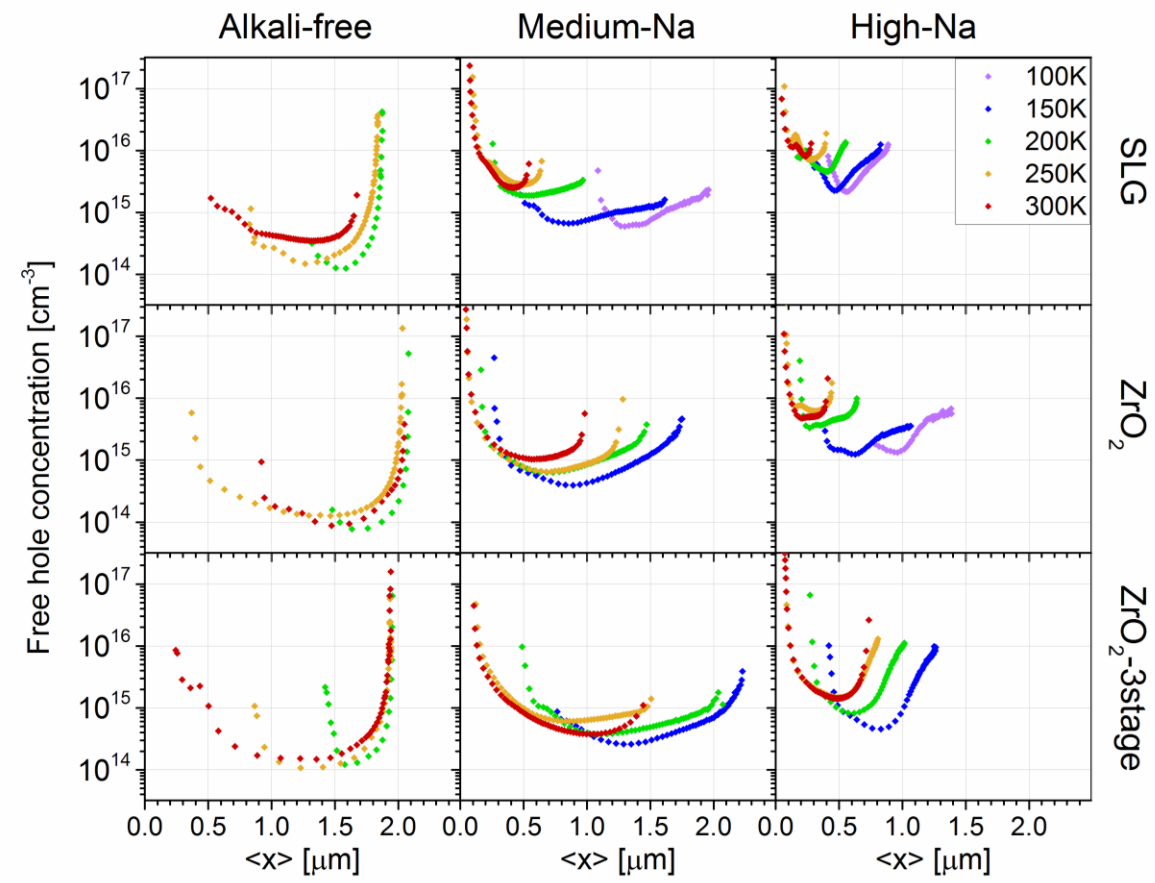

Figure 9.2 Relaxed DLCP profiles as a function of temperature for alkali-free, medium Na and Na rich solar cells prepared on SLG/SiO_xN_y (top row) and ZrO_2 (middle row) substrates and 3 stage CIGSe cells on ZrO_2 substrates (bottom row). Please note the spectra for alkali free devices at lower temperatures might exhibit artificially high carrier density (see Chapter 8.4).

Substrate	Process	x	medium-Na	high-Na
SLG/SiO_xN_y	Single-stage	22	190	473
ZrO_2	Single-stage	<1	95	554
ZrO_2	Three-stage	5	114	166

Table 7. Concentration of sodium for the alkali-free, medium-Na and high-alkali cells presented in Figure 9.2.

DLCP spectra taken at high frequency as a function of temperature for investigated series of solar cells are presented in Figure 9.2. For each of the 3 series: single-stage devices on SLG/SiO_xN_y and ZrO_2 as well as 3-stage devices on ZrO_2, three devices were chosen, representing alkali-free, medium-Na and Na-rich compositions.

In the left column DLCP curves for Na-free devices are shown. As can be seen, all of them look similar – U-shaped, leaning on the back contact (as 0 corresponds to the CdS/CIGSe interface, 2μm to the back contact interface). The observed free hole concentration, taken at the minimum of the DLCP curve, at 250-300K is about $10^{14}cm^{-3}$, which corresponds well to the literature data available for alkali-free solar cells, where p was shown to lay between $1\text{-}2\cdot10^{14}cm^{-3}$ be it single-stage or 3-stage devices [32, 88, 158]. For undoped samples high series resistance distorts the results of measurement: the observed free carrier density increases with temperature decreasing. This can be clearly seen in Figure 9.3 where the values of free hole concentration taken at low temperatures are higher than those at higher temperatures – contrary to what is expected. The increased apparent hole concentration at low temperatures is a byproduct of the high series resistance, unaccounted for in the model used here (see Chapter 7.3). Therefore, in this work only values of free hole concentration at 200K and above will be taken into consideration.

Upon addition of even a minuscule amount of sodium, free hole concentration is increased by about an order of magnitude, depending on the cells' manufacture method and sodium concentration. The curves also become wider, stretching for the most part of the absorber. The free hole concentration increases with increasing temperature, partially due to the ionization of deeper defects and also to the effect of deeper defects responding to ac frequency.

Once a high concentration sodium is added the curves become narrower, take on a V-shape and move closer to the CdS/CIGS interface (lower series resistance). Free hole concentration is further increased, to about $5\cdot10^{15}cm^{-3} – 10^{16}cm^{-3}$ (300K), two orders of magnitude higher than it was in the Na-free case. These values are again comparable with the data available for Na-containing cells, including those used commercially [115, 117, 129, 159].

In all, the hole concentration values for all three categories of devices – Na-free, medium-Na and Na-rich cells – are consistent throughout all three series of devices and increase with an increase in sodium concentration/PDT temperature.

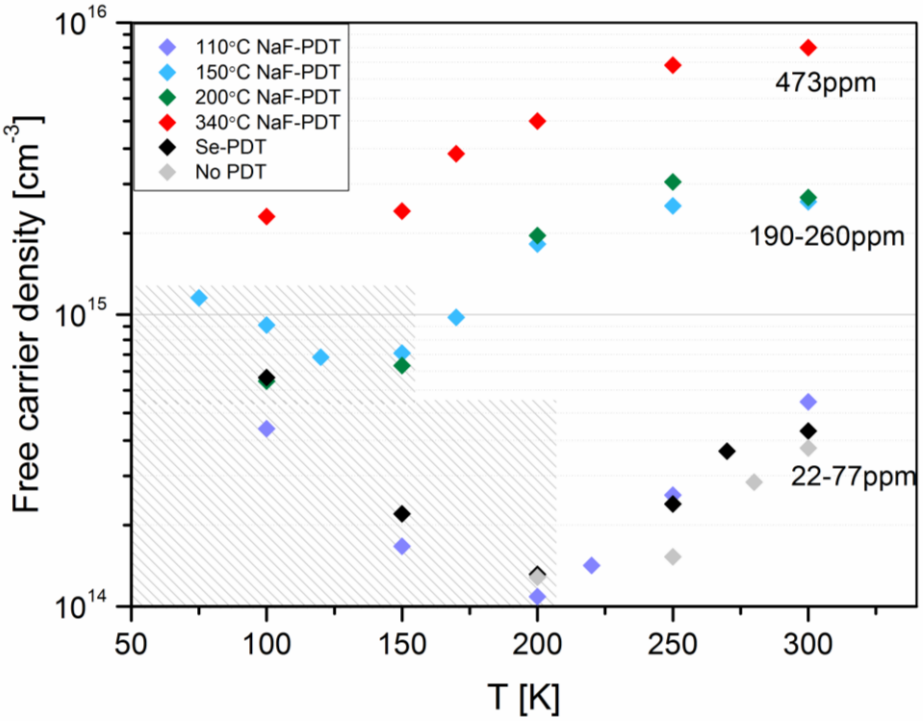

Figure 9.3 Values of the free hole concentration obtained from DLCP for cells in the SLG series as a function of temperature in the relaxed state. Dashed area represents the region of artificially high apparent p. Values on the right represent the sodium concentration range.

9.2.2 Free hole concentration – metastable state

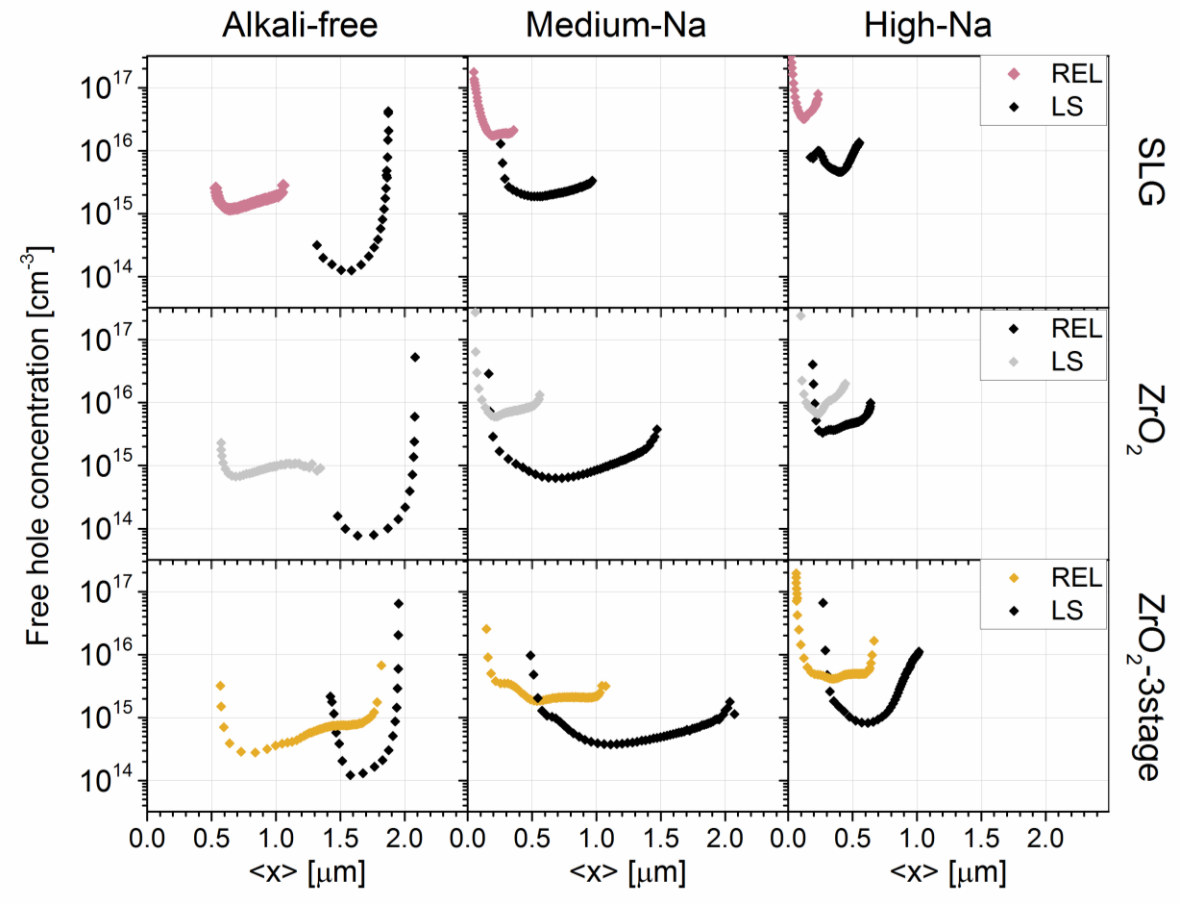

Figure 9.4 Comparison of the relaxed and light soaked DLCP spectra of alkali-free, intermediate and high sodium-doped devices prepared on SLG and ZrO_2 substrates using single- and three-stage evaporation methods. All measurements were taken at 200K.

In Figure 9.4, a comparison between relaxed and light-soaked DLCP spectra of selected cells taken at 200K is presented. In the alkali-free devices, the relaxed free hole density equals $10^{14}cm^{-3}$. The difference in the absolute position of the back edge – between about 1.8µm to 2.2µm – is not significant, as it can be attributed both to the difference in the absorber thickness, as well as to the uncertainty of the sample surface. The metastable curves look virtually the same in both of the single-stage devices with carrier density at about $10^{15}cm^{-3}$, while the PPC effect in the larger-grained, 3-stage device is considerably lower at $4 \cdot 10^{14}cm^{-3}$. The same can be said about the medium-Na cells, where the PPC effect for the 3-stage device is lower as well, although this may be in part attributed to the variation in alkali content. The greatest variation can be seen in the high-Na cells, where both the relaxed and metastable free carrier density is an order of magnitude higher in the SLG series than in the 3-stage one, and the PPC is barely visible in the single-stage, ZrO_2 cell.

9.2.3 Conductivity of thin films – steady-state properties

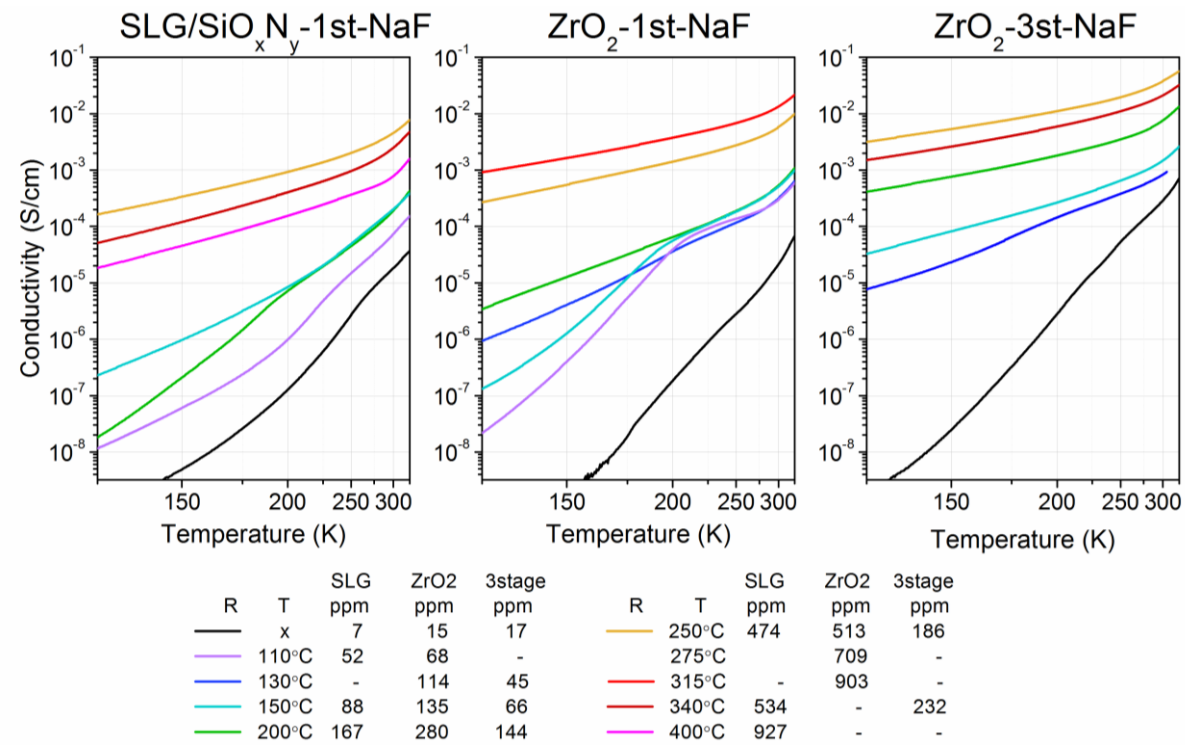

Figure 9.5 Conductivity vs temperature measurements of thin film devices prepared on (left) SLG and (center) ZrO_2 substrates using the single-stage method, and thin films prepared on ZrO_2 substrates using a 3-stage method (right). The same color scheme was used across all three plots with regards to the PDT temperature.

Series of conductivity vs temperature measurements for thin film devices with different concentrations of added sodium are presented in Figure 9.5. As can be seen, samples which underwent NaF-PDT exhibit considerably higher conductivity than alkali-free ones (black line), up to over 2 orders of magnitude at room temperature. This is consistent with the literature data, where an increase in conductivity was observed after Na-doping, independent on the supply method [96, 112, 130]. Additionally, this difference in conductivity becomes even more pronounced at lower temperatures – reaching about 5 orders of magnitude at 150K.

In thin films prepared on SLG substrates, already an addition of 52 ppm Na (as compared to 7 ppm in Na-free device) resulted in an about 4x increase in conductivity, followed by a small increase with further sodium addition. This increase is even more evident in the single-stage CIGSe films prepared on ZrO_2 substrates, with the difference reaching over an order of magnitude. In both series we then reach a plateau, when increasing temperature or sodium concentration does not influence the conductivity – in case of SLG it lays between 150ºC and 200ºC (88 ppm and 167 ppm respectively), in ZrO_2 – between 110ºC and 200ºC (68 ppm and

280 ppm respectively). Additionally, some of the curves in this region are curved, with significantly higher slopes at low temperatures. This feature, however, seems not to depend monotonically on the temperature or Na content, alternating between “normal” and “kinked” behavior. This could be caused by the PDT process itself – as those PDT temperatures are outside of the normal PDT temperature range (which is considerably higher), the process parameters might not be optimized, resulting in unwanted effects. For instance, there may be some defect property (i.e. thermal activation from deep defect states), which may be influenced by annealing sodium or selenium atmosphere in this temperature range.

Between 200ºC and 250ºC a step increase in sodium concentration and – as a result – conductivity is observed in both series. However, in SLG series after reaching a maximum conductivity for NaF-PDT at 250ºC (474 ppm Na) further increase in temperature or addition of sodium results in a decrease in conductivity. There are some reports showing that excessive amount of sodium can negatively influence the material [131], i.e. could lead to a decrease in hole concentration [132], which could in turn impact conductivity. The sample annealed at 400ºC exhibits significantly worse properties than that annealed at 250ºC. In the corresponding cells the one with NaF-PDT made at 400ºC exfoliated from the substrate, so it is possible that a second, Na-rich phase is forming, reducing the beneficial effect of Na (just as described by Kamikawa et al. [132]). In samples prepared on ZrO_2 substrates, no such effect was observed, even though the maximum concentration of sodium was comparable to the 400ºC planar device from the SLG series. This may point to the effect being influenced by temperature rather than Na concentration itself, as the highest PDT for the ZrO_2 series was 314ºC – lower than the 340ºC at which the decrease is first observed in SLG-series.

While the results for the two single-stage series looked fairly similar, the conductivity of films prepared using the 3-stage method follow the same trend with regards to alkali incorporation, but the conductivity is always higher by about an order of magnitude (at room temperature), and the changes are observed already for lower sodium concentrations. It is to be expected, as 3-stage devices are known for their bigger grains and overall better crystallinity [42], so the reduced grain surface would impact the amount of alkali that can enter the CIGSe layer. Again we see the reduction of σ once the PDT-temperature reaches 340 ºC.

Another interesting aspect, seen across all three series, is the reduction of the slope of the σ(T) curves (or the activation energy of conductivity) with an increase in sodium concentration. It is

visible most clearly in the low-Na three-stage devices, where the alkali-free layer (black) and the 45 ppm layer (blue) have fairly similar conductivity at room temperature, but the slope of the curve is vastly different. This is likely caused by the impact of sodium on the hole mobility in the material and its temperature dependence.

A hypothesis that potential barriers influenced by alkali metals determine conductivity dependence on temperature will be further explored in the next chapters.

9.2.4 Conductivity of thin films – metastable properties

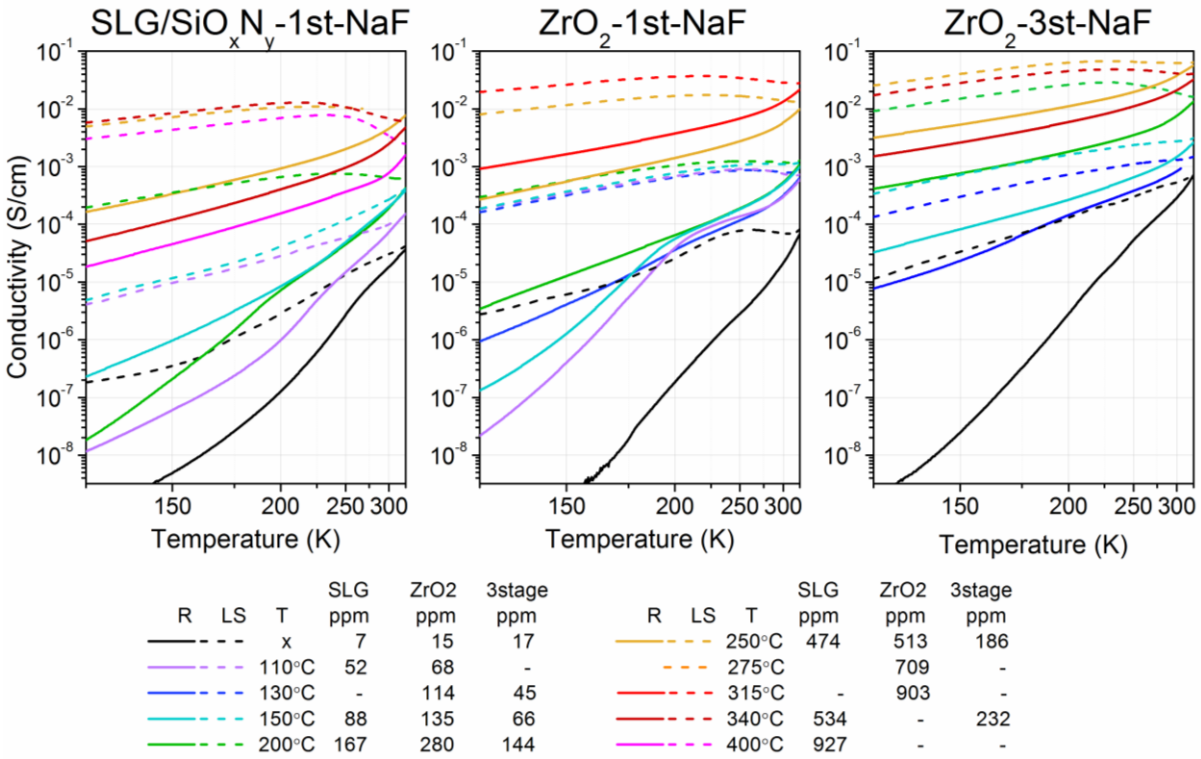

Figure 9.6 Conductivity vs temperature measurements for Na-containing devices in relaxed (solid lines) and metastable state induced by light-soaking (dashed lines). Discussion of the relaxed properties can be found in previous chapter.

In all cases, the slope of LS curve is lower than that of the device in steady state. This is clearly visible in the low-alkali films, where the relaxed slope is the sharpest.

What is also interesting, is that the films which exhibit the double-slope behavior in the relaxed state show normal LS behavior. In ZrO_2 series, the films with T_{PDT} between 110ºC and 200ºC, all of the devices – both those with and without kink in the $\sigma_R(T)$ curves – exhibited virtually the same $\sigma_{LS}(T)$ characteristics.

9.3 Effect of potassium

9.3.1 Free hole concentration – relaxed state

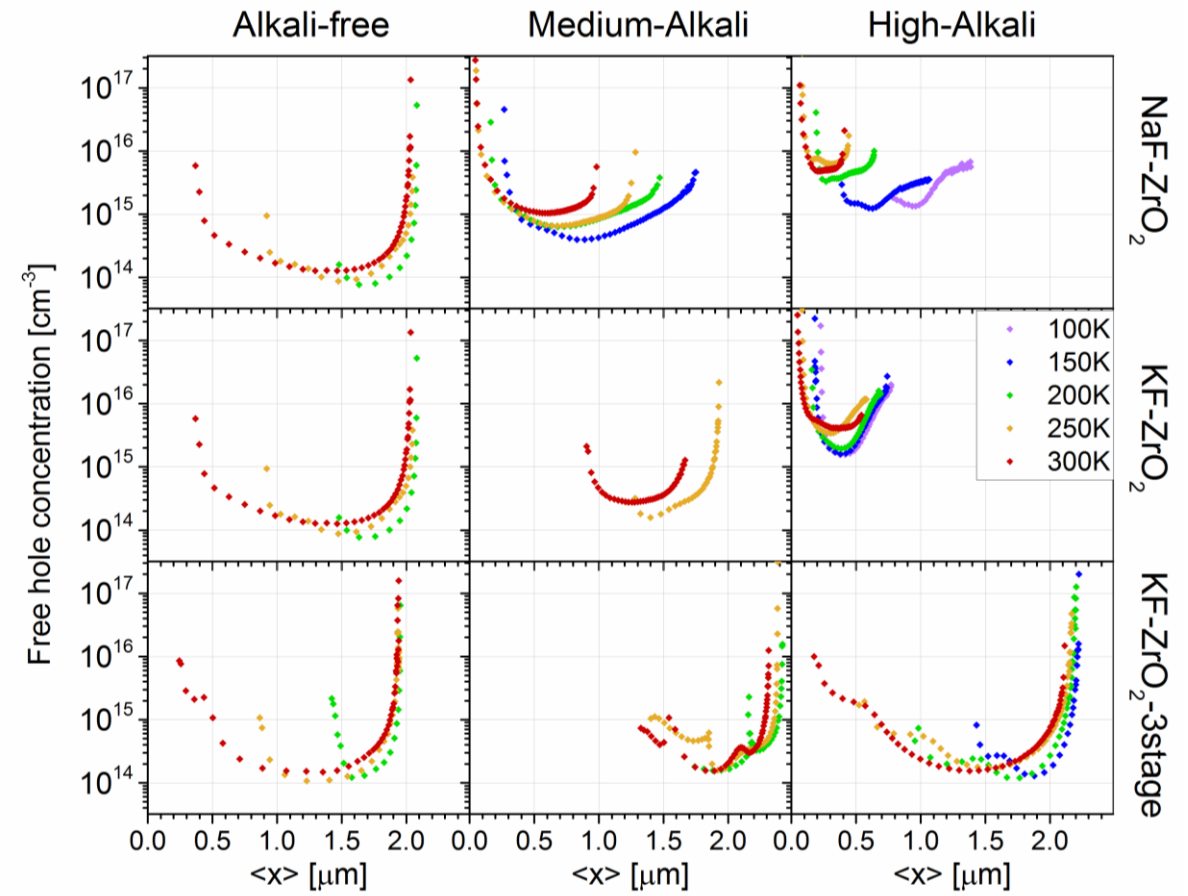

Figure 9.7 Relaxed DLCP profiles as a function of temperature for alkali-free, medium-alkali (and alkali-rich solar cells: Na-doped single-stage devices on ZrO_2 substrates (top row) potassium-doped single-stage devices on ZrO_2 (middle row) substrates and potassium-doped 3-stage CIGSe cells on ZrO_2 substrates (bottom row). The spectra for alkali-free devices at lower temperatures might exhibit artificially high carrier density.

PDT	Process	x	medium-alkali	high-alkali
NaF	Single-stage	<1	95	554
KF	Single-stage	<1	554	1794
KF	Three-stage	<5	189	495

Table 8. Concentration of sodium/potassium in ppm for the alkali-free, medium-alkali and high-alkali cells presented in Figure 9.7.

DLCP spectra of the potassium-doped series, together with a reference sodium-doped cells are presented in Figure 9.7. The alkali-free series were discussed previously, as both the sodium and potassium doped cells were prepared in the same cycles. The low-potassium single-stage cell differs from its sodium counterpart – the increase in the free hole concentration is very low, and all of the DLCP spectra taken below 250K were highly distorted, thus not shown here. Similar results were obtained for the 3-stage cell, with the spectra differing from the typical U or V-shape and pushed towards the back contact, typical of samples with a very low free hole concentration.

However, after an addition of large amounts of potassium (last column), the single-stage device exhibits similar characteristics to the high-Na one – namely, an increase in the relaxed hole concentration of over 1 order of magnitude compared to the alkali-free cell, with narrowing of the DLCP curve. The main difference between the high-Na and high-K cells here is the temperature dependence, which is considerably less pronounced for the potassium cell. The high-potassium three-stage cell, on the other hand, exhibited virtually no increase of the relaxed hole concentration as compared with the alkali-free one. This again might be in part caused by the DLCP limitations regarding low doping densities. What is similar here to the Na-doped 3-stage devices is that the overall doping density increase is lower than in case of single-stage cell and the spectrum is broader.

9.3.2 Free hole concentration – metastable state

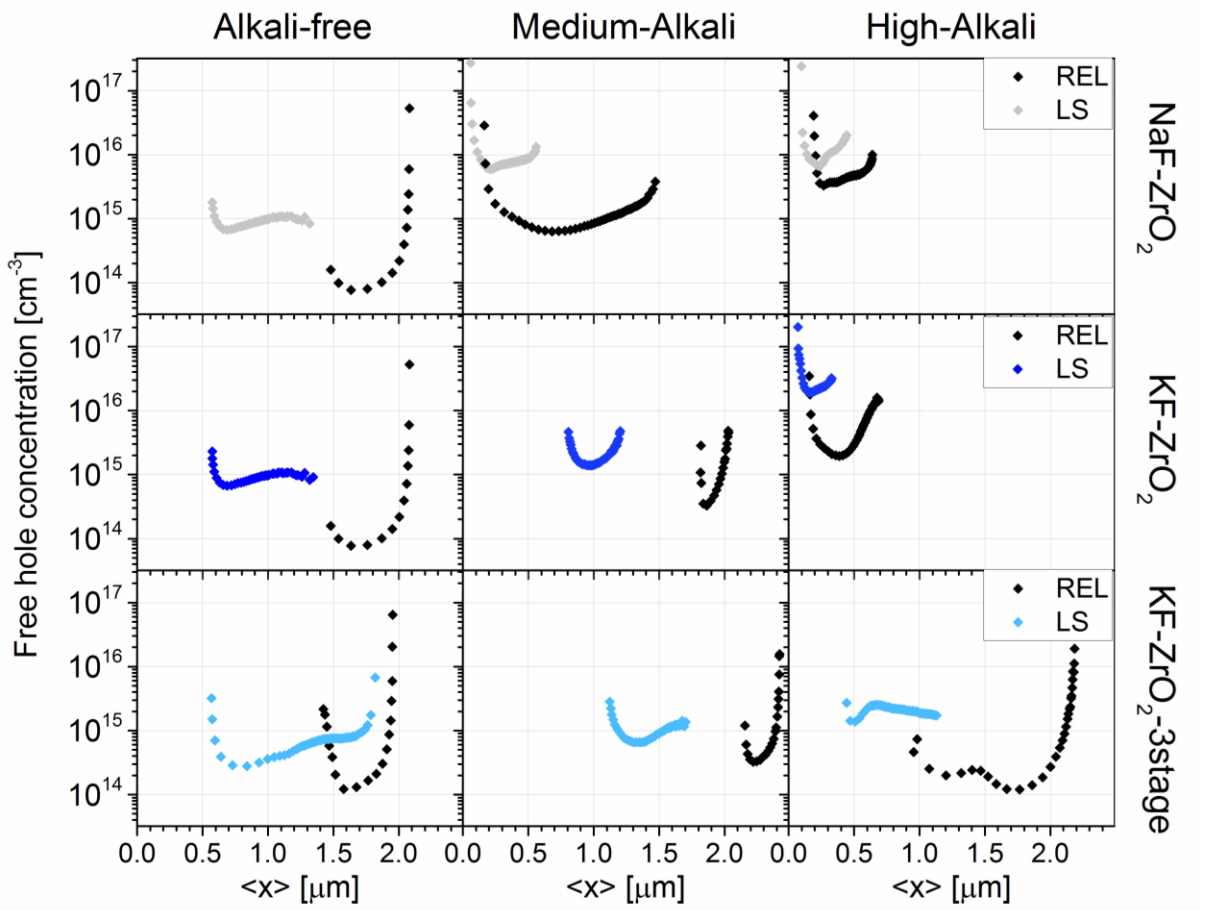

Figure 9.8 Comparison of the relaxed and metastable (light-soaked) DLCP spectra of alkali-free, medium- and high potassium-doped devices prepared on ZrO_2 substrates using single- and three-stage evaporation methods. In the first row, results on Na-doped single-stage CIGS were presented for comparison. Alkali-free cells are the same as previously presented for Na-series. DLCP spectra for low-potassium cells in the relaxed state are unreliable. All measurements were taken at 200K.

DLCP results taken at 200K in the relaxed and metastable state of devices doped with potassium are presented in Figure 9.8. Measurements on the low-K cells in the relaxed state at this temperature did not yield reliable results, as the junction was dominated by secondary barriers and unfit for DLCP analysis. However, after light-soaking the carrier concentration is increased as would be expected, and appears similar to that in the low-sodium devices, albeit its magnitude is slightly lower. The high-potassium single-stage cell (right column, middle row) looks almost the same as the corresponding high-sodium cell, with free hole concentration about an order of magnitude higher than in the alkali-free. In the metastable state, p increased a further order of magnitude, more than in case of ZrO_2 single-stage Na-doped device presented here, but similar to that of the one from the SLG series (see Figure 9.4).

9.3.3 Conductivity of thin films

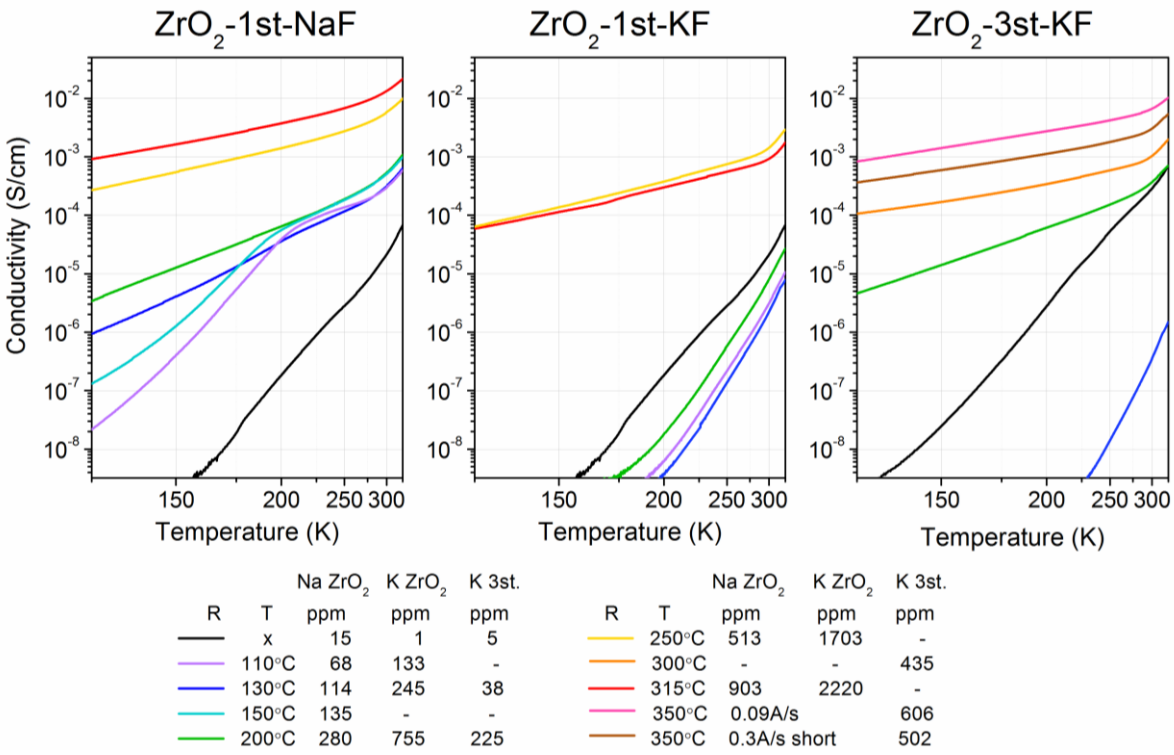

Figure 9.9 Conductivity vs temperature measurements of single-stage thin film devices prepared on ZrO_2 substrates with (left) NaF-PDT and (center) KF-PDT, and thin films prepared on ZrO_2 substrates using a 3-stage method subjected to KF-PDT (right). The same color scheme was used across all three plots with regards to the PDT temperature.

As was established in the literature and previous chapters, addition of any amount of sodium results in an increase in conductivity and free hole concentration with regards to the alkali-free CIGSe thin films and absorbers. In this chapter, the similarities and differences between the impact of sodium and potassium doping will be discussed.

First, I would like to focus on the impact of high concentrations of potassium (or potassium added in PDT at or above, 250°C). As can be seen in Figure 9.9, the $\sigma_R(T)$ curves have a very similar shape and slope to those measured after NaF-PDT. This would point to the general mechanism of conductivity increase being similar for both alkalis. One significant difference is that potassium concentrations required for the change are 3-4 times higher. Additionally, the maximum conductivity achieved with KF-PDT is still about an order of magnitude lower than that of NaF-PDT.

If we then look to the low-K (or low-temperature-K) we can see that in those cases addition of potassium was detrimental to the device performance. In single-stage thin films, adding

133 ppm or 245 ppm of K (100ºC and 130ºC respectively) resulted in a **decrease** in conductivity of about 1 order of magnitude as compared to the alkali-free device. Only once 755 ppm K was added (or annealing temperature reached 190ºC) the effect started to subside, though σ was still lower than in case of the K-free layer. This effect is even more pronounced in the 3-stage devices, where the alkali-free conductivity is higher. There, addition of potassium at 130ºC resulted in an almost 3 orders of magnitude decrease (!). This is a proof that the deteriorating effect of low-temperature PDT is not limited to certain CIGS technology, but is a more general phenomenon. After raising the PDT temperature to 200ºC, σ_R(330K) resembled that of the alkali-free device, but with a considerably lower activation energy of conductivity.

It is worth noting that the cells after low-temperature PDT, which correspond to the layers showing low conductivity and high slope of σ(T) dependence exhibit extremely bad efficiency (see Table 3 on page 43). Thus, the deterioration of conductivity for low-K samples indicates a presence of internal barriers in the CIGS material itself which hinder the carrier transport.

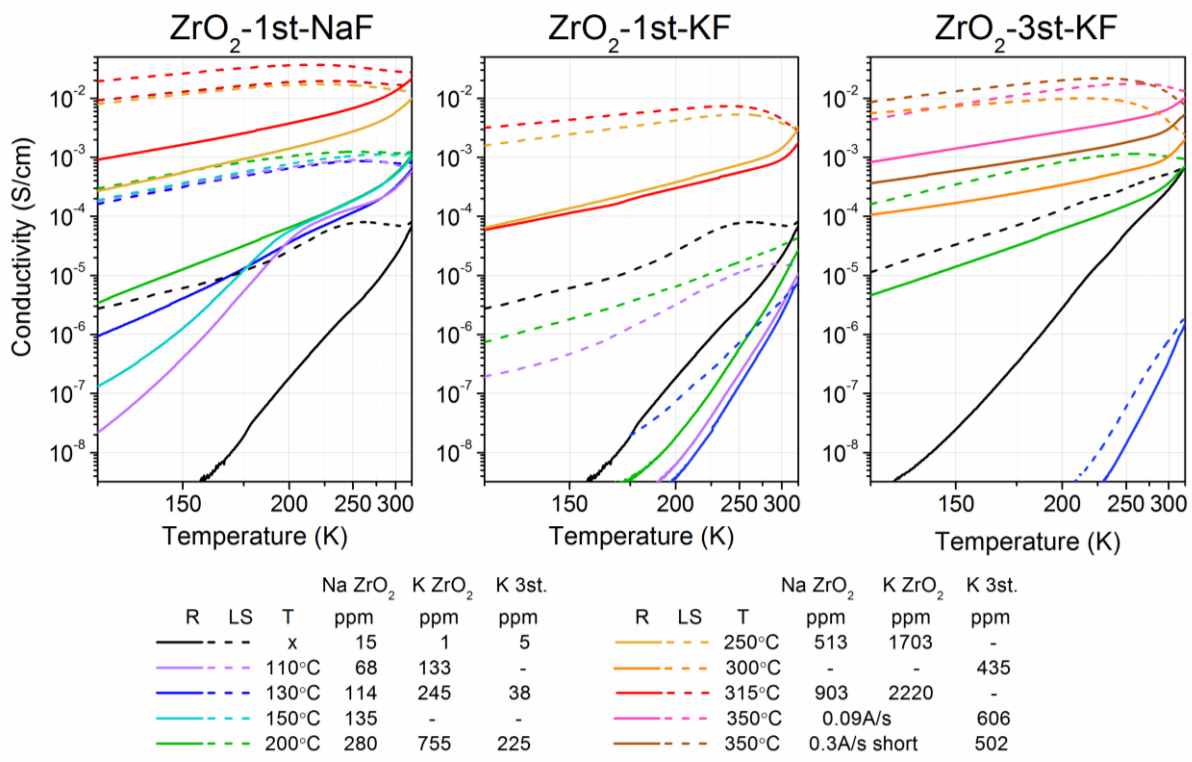

Figure 9.10 Conductivity vs temperature measurements in the relaxed (solid lines) and metastable state (dashed line) of single-stage thin film devices prepared on ZrO_2 substrates with (left) NaF-PDT and (center) KF-PDT, and 3-stage thin-films subjected to KF-PDT (right). The same color scheme was used across all three plots with regards to the PDT temperature.

In the light-soaked state, potassium doped thin films exhibit similar characteristics to the sodium doped ones in terms of both the activation energy and the overall magnitude of the PPC. The major difference can be observed in the films doped with small amounts of potassium (dark blue in Figure 9.10). Here, not only did the potassium reduce the conductivity in the relaxed state, but also significantly decreased the observed PPC – especially in case of the 3-stage device.

9.4 Influence of process type and Cu-content

In previous chapters, the influence of sodium and potassium on the electrical characteristics of CIGS films and solar cells was presented. However, to fully understand the results it is crucial to look deeper into other factors which might influence the properties of the material, such as the type of process (single-stage vs three-stage), the influence of the grain size or the copper to indium & gallium ratio (CGI). These factors will be discussed in this chapter.

9.4.1 Influence of the process type on the alkali-free and high-alkali absorbers

No significant differences between the single-stage CIGSe samples prepared on SLG/SiO_xN_y and ZrO_2 substrates was observed in the previous part. Here, variations in the electrical characteristics between devices prepared using different evaporation processes will be discussed. In addition to devices described previously, a set of large-grained 3-stage solar cells and thin films – alkali-free, NaF and KF-treated – was investigated. All devices studied in the main parts of this work had comparable values of CGI ranging between 0.77 and 0.82 to reduce the impact of mean copper concentration. Values of CGI for the devices described in this chapter can be found in Table 9.

In Figure 9.11 $\sigma(T)$ characteristics of single-stage, three-stage and large-grained three-stage thin films are presented. The alkali-free 3-stage films, both regular (yellow) and large-grained (green), look virtually the same. They have about an order of magnitude higher conductivity than the alkali-free single-stage film, but its slope – meaning the activation energy – is similar

across all three devices. In DLCP measurements at 200K shown in Figure 9.12 all three alkali-free cells exhibit $p \approx 10^{14} cm^{-3}$ with the DLCP curve pushed to the back contact.

All high-sodium doped thin films have very similar values of conductivity and its temperature dependence, but the observed free hole concentration of the three-stage cell is smaller by a factor of about 3.Values of conductivity of high-K thin films were lower than those from high-Na, and the smallest difference was in three-stage device, which also had the highest conductivity. In solar cells on the other hand, the highest carrier concentration was observed for the single-stage cell. The lack of a systematic dependence of the properties of the alkali-rich devices on the process type makes it safe to assume that the main differences between those devices are caused by variations in the alkali concentration.

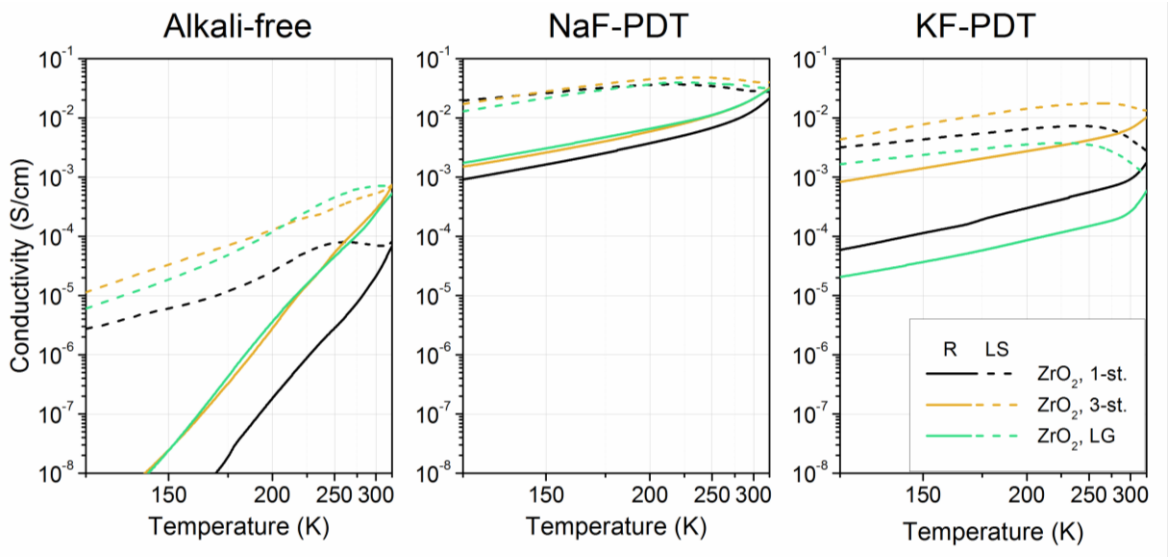

Figure 9.11 Conductivity vs temperature measurements of alkali-free, sodium- and potassium-doped thin films prepared on ZrO_2 substrates using the single-stage (black), three-stage (yellow) and large-grained three-stage method (green).

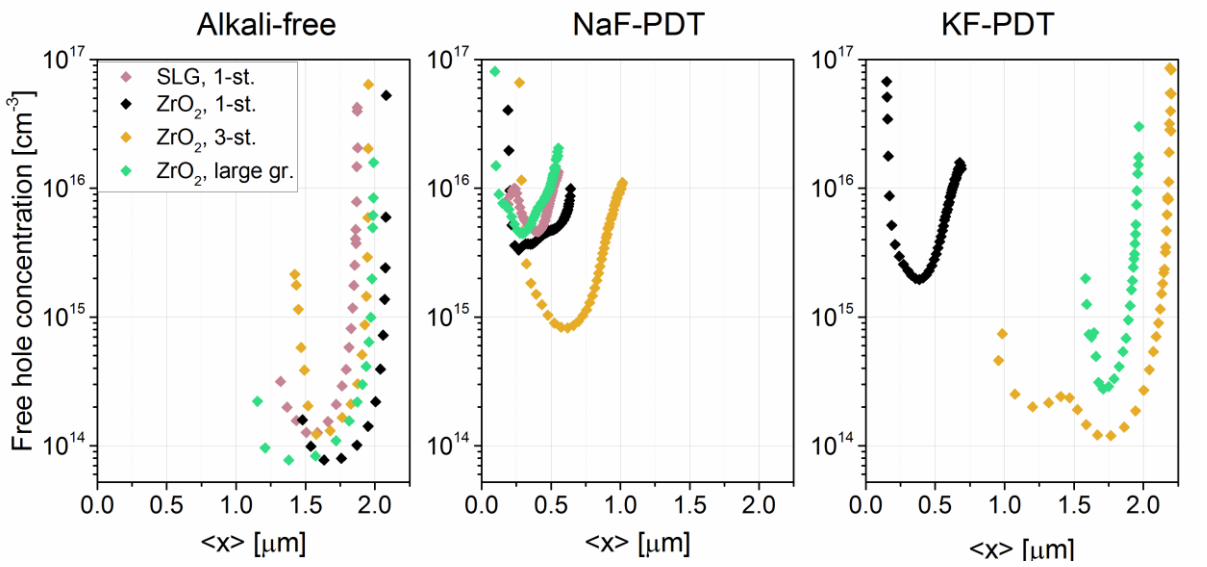

Figure 9.12 DLCP measurements taken at 200K on solar cells complimentary to the thin films presented in Figure 9.11.

Substrate	Process	Alkali-free	NaF-PDT	KF-PDT
ZrO_2	Single-stage	0.82	0.78	0.81
ZrO_2	Three-stage	-	-	-
ZrO_2	Large-grained	0.80	0.79	0.80

Table 9 CGI of thin films presented in Figure 9.11 and cells presented in Figure 9.12. Dash denotes lack of an appropriate measurement.

		Thin films			Solar cells		
Substrate	**Process**	**Alkali-free**	**NaF-PDT**	**KF-PDT**	**Alkali-free**	**NaF-PDT**	**KF-PDT**
ZrO_2	Single-stage	17	956	2252	< 1	553	1794
ZrO_2	Three-stage	< 1	144	605	5	166	495
ZrO_2	LG three-stage	< 1	156	259	< 0.1	293	355

Table 10 Dominant alkali concentration in ppm of thin films presented in Figure 9.11 and cells presented in Figure 9.12. For alkali-free devices the sum of both alkalis was provided.

9.4.2 Influence of CGI ratio of the film and cell properties

All of the previously described thin films and solar cells had the copper content equal to the CGI ratio of about 80%. To study the impact of the copper content on device characteristics, additional measurements on thin films with CGI between 74% and 86% were performed. In the alkali-free series, going from 74 to 86% CGI resulted in a steady increase in conductivity of

about 1.5 orders of magnitude, with the impact on the metastable σ(T) dependence being similar. This result confirms the general opinion that increase of copper content leads to lower compensation in the CIGS material. All of the NaF-treated thin films exhibit similar conductivity and its dependence on temperature, and as such it is unlikely that copper would play a significant role in the change in conductivity in the alkali-treated devices. However, it is impossible to distinguish between the influence of copper content on the compensation level of the material and impact of sodium-depending Cu content, as the sodium concentration varied largely between devices, possibly due to different sodium diffusivity in the material.

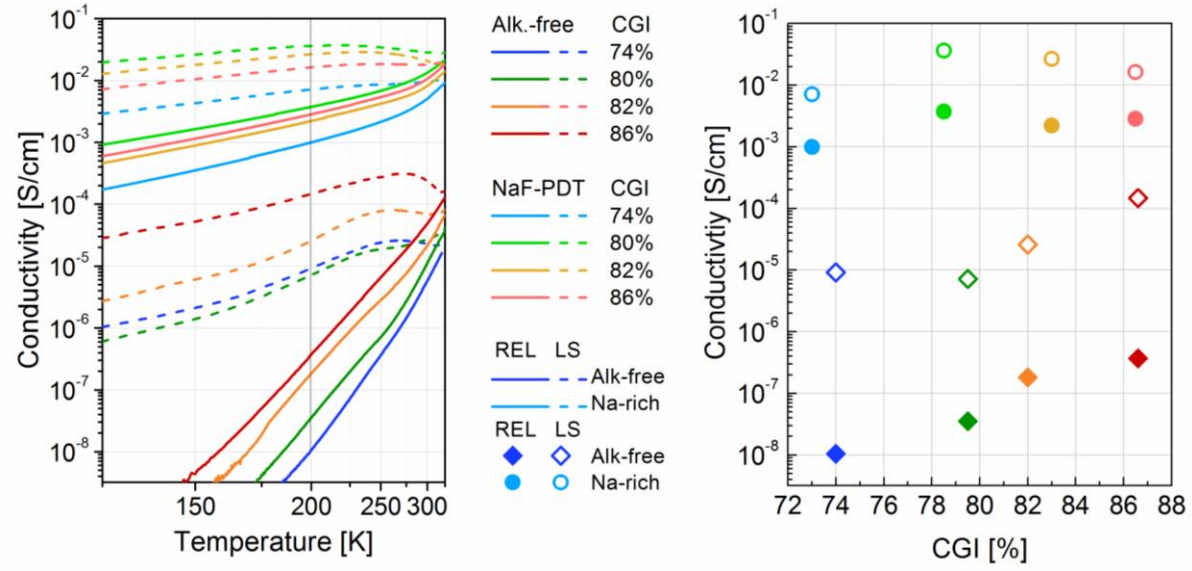

Figure 9.13 Conductivity vs temperature measurements of alkali-free (dark lines) and sodium-doped single-stage thin films with varying CGI (left). Values of conductivity of those films at 200K as a function of CGI (right).

CGI	Alkali-free [ppm]	NaF-PDT [ppm]
74%	36	801
80%	33	957
82%	15	1040
86%	20	680

Table 11 Sodium concentrations of thin films from the copper series presented in Figure 9.13

10 Discussion

10.1 Relaxed properties

10.1.1 The effects of sodium and potassium

What can be immediately taken from the results presented before is the similarity between the effect of sodium and potassium on Cu(In,Ga)Se_2. Doping with both alkalis (excluding low-K concentrations) resulted in an increase in the $V_{OC,}$ FF, and the solar cell efficiency, with little to no change in the J_{SC} (see Chapter 8.2). This is a consequence of the changes in the electrical properties of CIGS absorbers resulting from alkali doping. I observed the following effects which have been in detail discussed in the previous chapters:

- an increase in free hole concentration in solar cells
- an increase in conductivity with subsequent reduction of the slope of the σ(T) dependence (likely linked to decreased mobility barriers)
- increase in the absolute value of the PPC

What stands out is the striking similarity in the results obtained for sodium and potassium, pointing to a similar pathway in both cases. However, in order to come to some definitive conclusions, it is important to be able to compare data available from different measurement and device types. As about 4x more potassium than sodium was needed to achieve the same beneficial effect, a common variable, effective alkali concentration c_{eff}(alk), could be introduced:

$$c_{eff}(alk) = c(Na) + 0.25\, c(K) \qquad (42)$$

Where c(Na) and c(K) is the sodium and potassium concentration. Using effective alkali concentration we can construct graphs in which properties of Na- and K-treated samples are directly compared. If we then look at Figure 10.1 we can see that both free hole concentration in solar cells and the conductivity in thin films follow similar trendlines for sodium and potassium – stable, low value until c_{eff}(alk) reaches about 100ppm, followed by a steep increase until a second plateau between 100 and 400ppm and another smaller increase for higher

concentrations. The exception are three samples fabricated under low KF-PDT temperature which will be discussed separately.

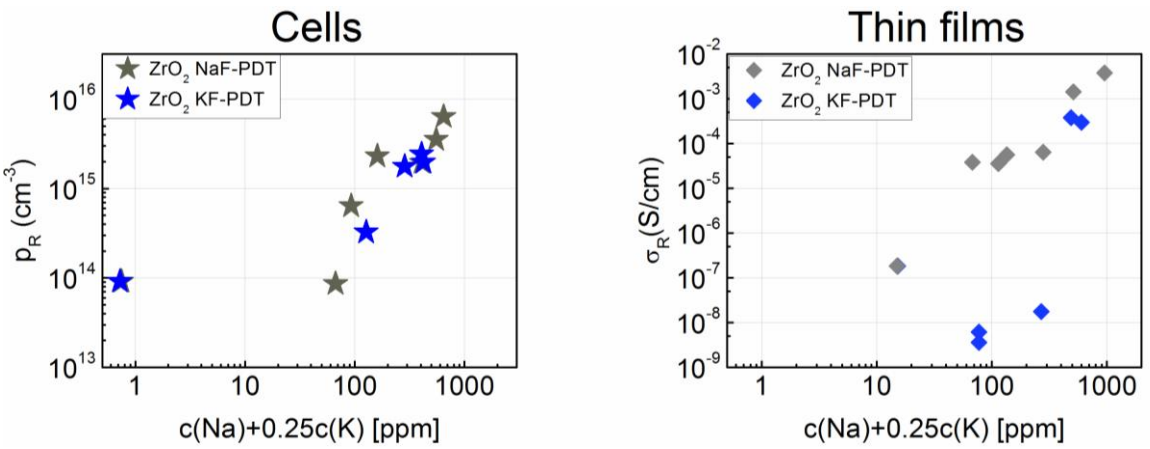

Figure 10.1 Free hole concentration in sodium and potassium-doped single-stage cells in the relaxed state (left), and conductivity of corresponding thin films (left). All measurements taken at 200K.

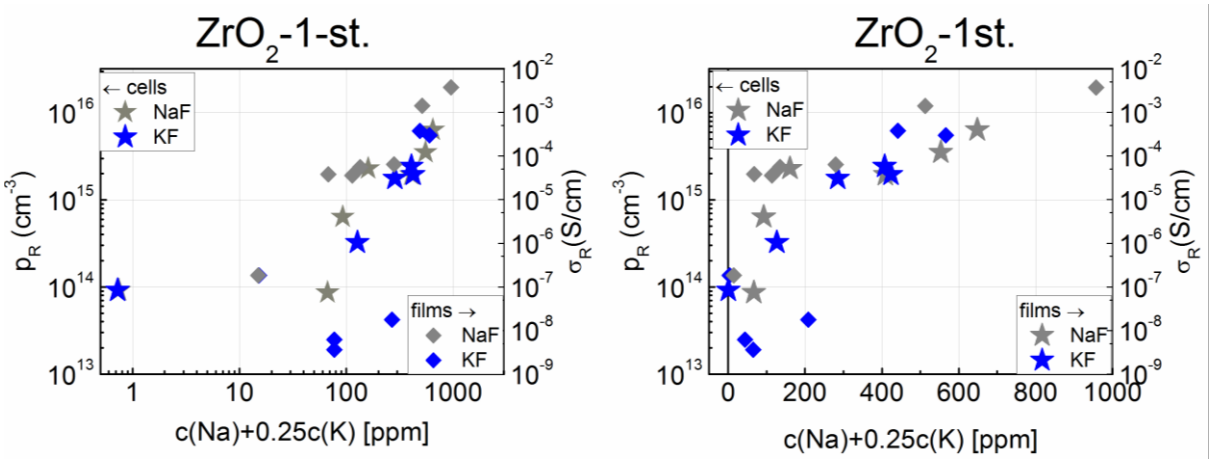

Figure 10.2 Free hole concentration (stars, left axes) and conductivity of corresponding thin films (diamonds, right axes) in Na and K-doped single-stage devices in the relaxed state as a function of effective alkali concentration. On the left the X axis is in the logarithmic scale, on the right – linear to better show the high-alkali region.

A relation between the free carrier concentration and conductivity dependence on the effective alkali concentration is presented in Figure 10.1. As can be seen, they both follow the same trendline (again except the three low-potassium thin films), with the only difference being that there are 2 orders of magnitude increase in conductivity per each order of magnitude in free hole concentration.

Conductivity in CIGS can be denoted as:

$$\sigma = pe\mu \tag{43}$$

where p is the free hole concentration, e is the electron charge and μ is the hole mobility. This would mean that, if we assume the lateral and horizontal mobility within the CIGS to be the same (which may not be the case, as will be shown in Figure 10.8 on page 74), free hole density rises hand in hand with mobility:

$$\mu \sim p \tag{44}$$

Thus we conclude that the same factor has impact on both the mobility and free hole concentration. Mobilities calculated using DLCP-determined free hole concentration are presented in Figure 10.3 and range from 0.006 cm^2/Vs for the alkali-free materials up to about 0.6 cm^2/Vs for the high alkali ones. This is consistent, although on the lower end side, with the mobilities measured for polycrystalline CIGS films available in literature [160, 161]. Lower mobility goes hand in hand with the higher slope of the σ(T) dependence. These features point towards a model of barriers at grain boundaries limiting both free hole density and mobility, which will be presented in the subsequent chapters. At this point it has to be concluded that amount of sodium and potassium introduced to CIGS directly correlates not only with the free hole concentration but also to the mobility value.

In order to better study the effect of alkalis on mobility, Hall measurements would be preferable. Within the Beethoven project a set of corresponding thin films with Hall electrodes was studied. However, due to a very slow, logarithmic in time, transients due to the PPC observed in the conductivity and hence in the asymmetry voltage, which surpassed by orders of magnitude the expected Hall signal, the measurements were unsuccessful.

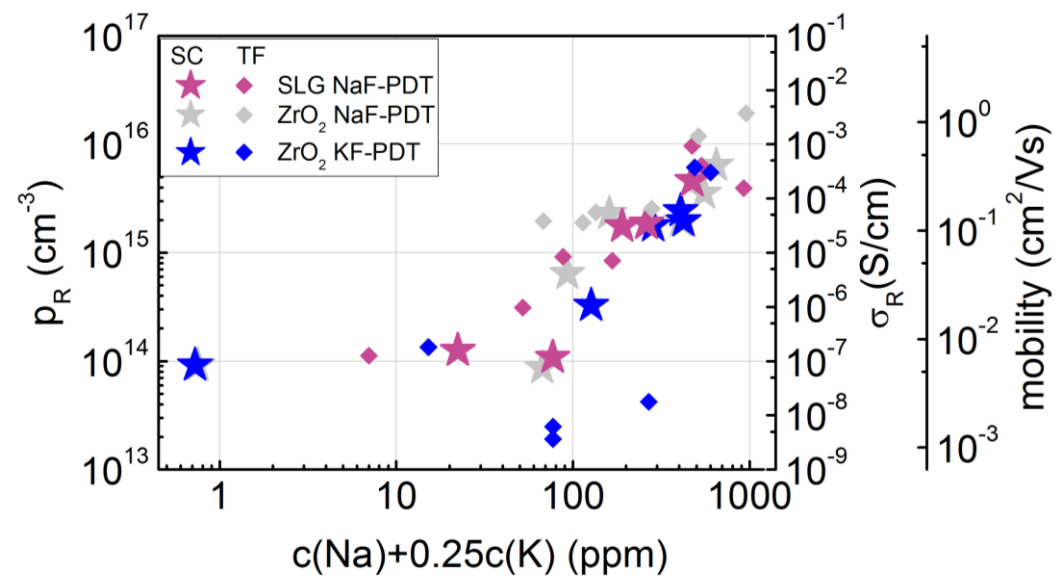

Figure 10.3 Values of relaxed free hole concentration (stars, left axis) and conductivity (diamonds, right axis) at 200K as a function of alkali concentration in single-stage devices. On the far right, an additional axis was added with approximate values of mobility calculated as $\mu = \sigma/pq$

The sodium- and potassium-induced changes in the conductivity and free hole concentration are also manifested in the photovoltaic properties of CIGS cells, as can be seen in the results of standard testing condition JV characterization results performed by ZSW plotted as a function of alkali concentration (Figure 10.4 and Figure 10.5). In sodium-doped cells, the V_{OC} and FF increase with the addition of Na, while the J_{SC} stays mostly unaffected. The efficiency increases from about 10% in the alkali-free cells to roughly 15-16% for high-Na cells. In general, high-K devices follow the trendline established by Na-doped devices[3]. The main difference is, just as was the case in the conductivity and DLCP measurements, in the outlier cells with low-K, which are visibly worse than both the trendline and respectable alkali-free devices with regards to all of the parameters, with the efficiency of the worst cell being below 1%.

[3] As more potassium diffuses into the device at the same T_{PDT} [127], resulting in a smaller effect per ppm, in Figure 10.13 potassium concentrations were scaled by a factor of 0.25 for clarity.

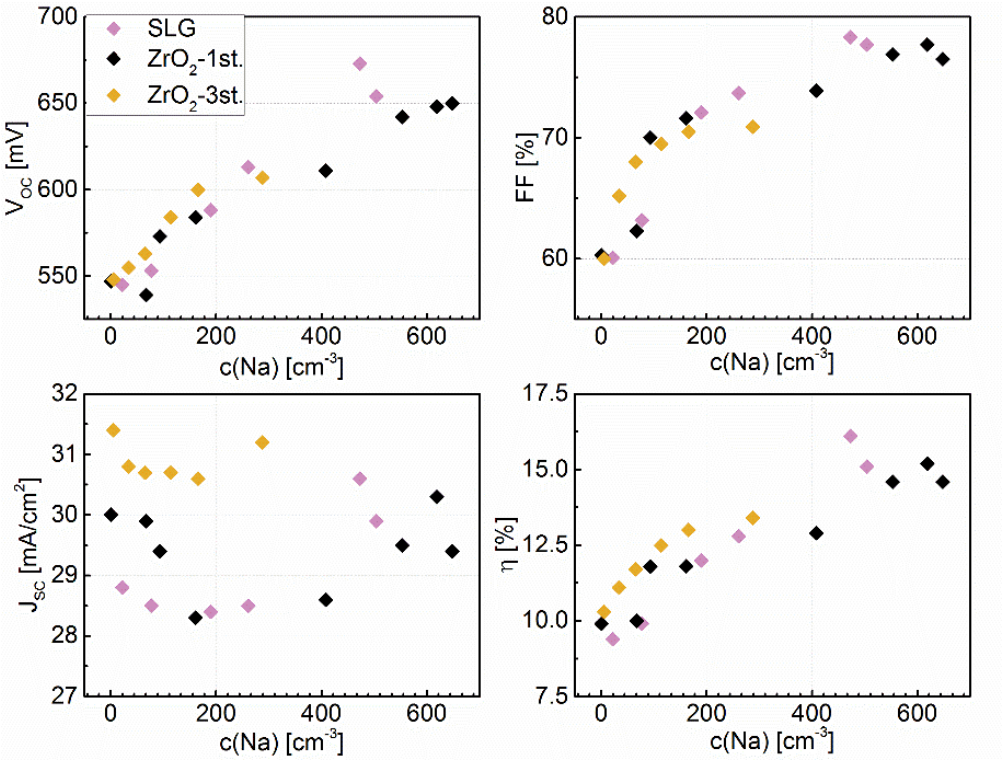

Figure 10.4 Photovoltaic parameters of solar cells prepared on SLG (purple), ZrO_2 (black) and on ZrO_2 using the 3-stage method (yellow) as a function of sodium concentration.

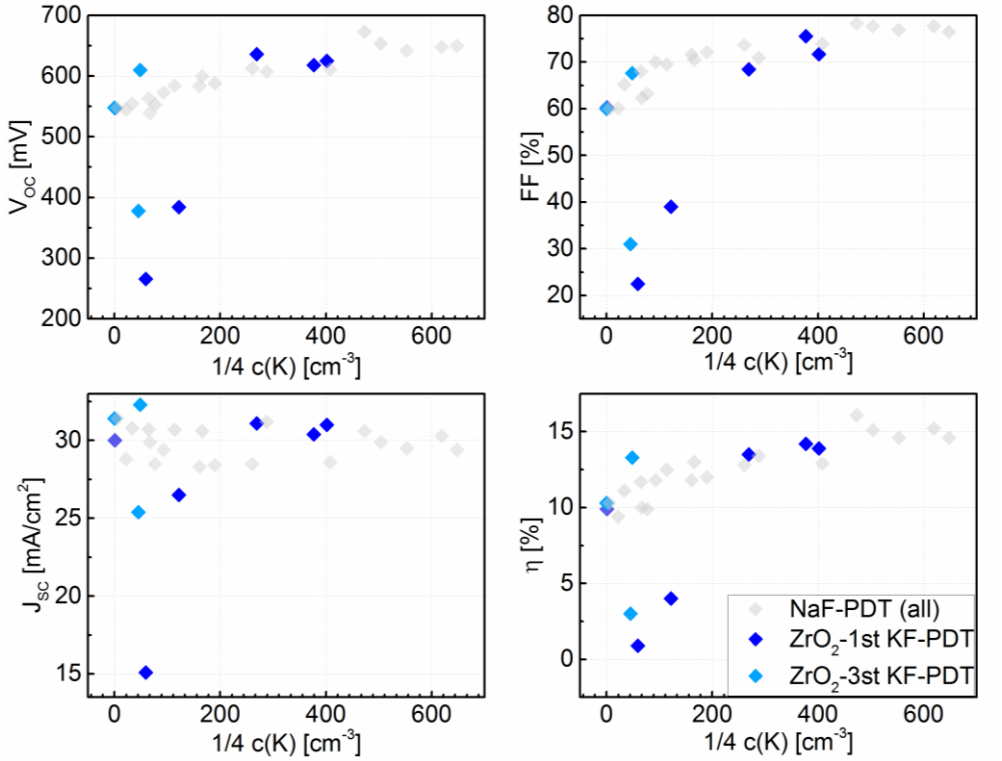

Figure 10.5 Photovoltaic parameters of solar cells prepared on ZrO_2 using single-stage (dark blue) and 3-stage method (light blue) as a function of potassium concentration. Gray points represent the results for sodium-doped cells presented in Figure 10.4. For clarity, the concentration of potassium was scaled by a factor of 0.25.

If we compare the effects of the two alkalis, we can see two main differences:

1) about four times more K than Na is needed to achieve the same beneficial effect
2) addition of small amounts of potassium (or addition of potassium at low temperatures) resulted in a decrease in conductivity and efficiency as compared to the alkali-free devices.

There are a few possibilities as to why the effect of potassium could be slightly different than that of sodium, namely:

a) higher concentrations of K than Na are needed for the same effect, i.e. because of a higher energy needed for a K^+ ion to passivate a given defect
b) the concentration itself might not be as important as the temperature at which the PDT took place, either through an increased diffusion into the grain or through the formation of potassium-containing phase(s) at the grain boundaries.

It is evident that while theory a) may explain the difference in needed concentrations of potassium for the beneficial effects, it cannot by itself explain the negative impact of low K concentrations. One possibility discussed in the literature is the ion-exchange mechanism, where potassium is thought to be pushing out sodium from the absorber. This mechanism, however, does not explain the changes in the sodium-free devices. A more likely alternative could be a formation of a K-containing phase on the grain boundaries, resulting in a creation of an energy barrier, limiting mobility and doping concentration. Growth of that phase could then occur within a narrow range of temperatures and outside of this range other processes become more favorable.

10.1.2 The effect of process type

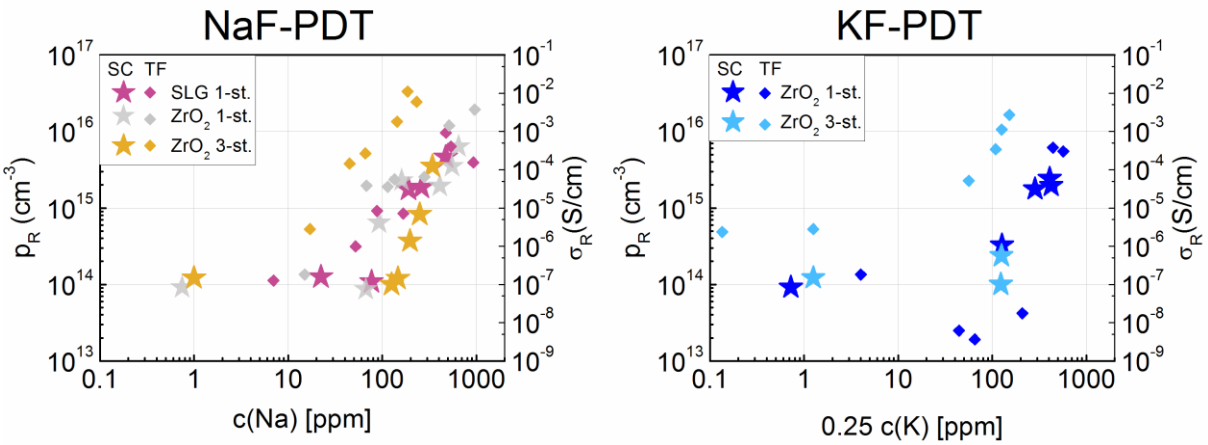

Figure 10.6 Free hole concentration (stars, left axes) and conductivity of corresponding thin films (diamonds, right axes) in Na and K-doped devices in the relaxed state as a function of effective alkali concentration.

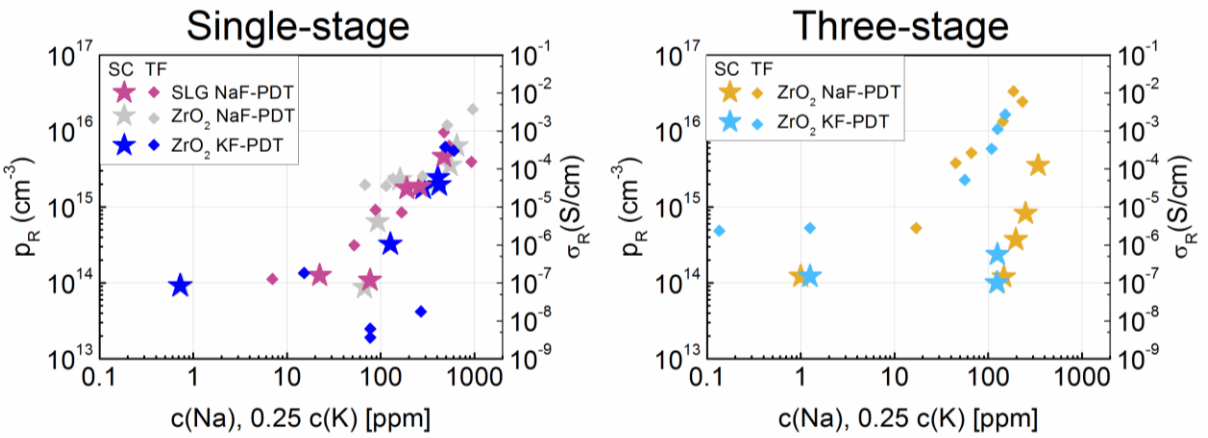

Figure 10.7 Free hole concentration (stars, left axes) and conductivity of corresponding thin films (diamonds, right axes) in single-stage and three-stage devices in the relaxed state as a function of effective alkali concentration.

In this work, the effect of sodium and potassium was studied not only on single-stage, but also on three-stage devices. In Figure 10.6 carrier concentration and conductivity of all 5 main series is presented, divided into Na- and K-doped devices. In Na-doped devices, we can see that both single-stage materials (prepared on SLG/SiO_xN_y and ZrO_2) show similar dependence. The difference is in the three-stage series. Thin films show about an order of magnitude higher conductivity than their single-stage counterparts. Analogous situation can be seen in the potassium-doped series.

If we then present the same data differently, dividing between the processes as shown in Figure 10.7, we can see that the main difference lays in fact between the deposition processes rather than the alkali doping used. In thin films, the conductivity is about an order of magnitude higher than expected, as well as shifted towards lower alkali concentrations, although its shape follows the behavior of cells. The increased conductivity in thin films, without a change in p of the cells, may be caused by a different pathway of current – in the three stage process, material is not uniform laterally, with regions of higher and lower CGI and GGI. This might cause the current to choose a path with higher conductivity rather than through the whole layer thickness, while in the solar cells current has to pass through the entire stack (Figure 10.8). Moreover, the samples investigated in this study had big grains close to the CIGS/CdS interface and a thin layer of a fine-grained material closer to the back contact. This was not the case in the single-stage material, which had a uniform stoichiometry as well as grain size in the horizontal direction.

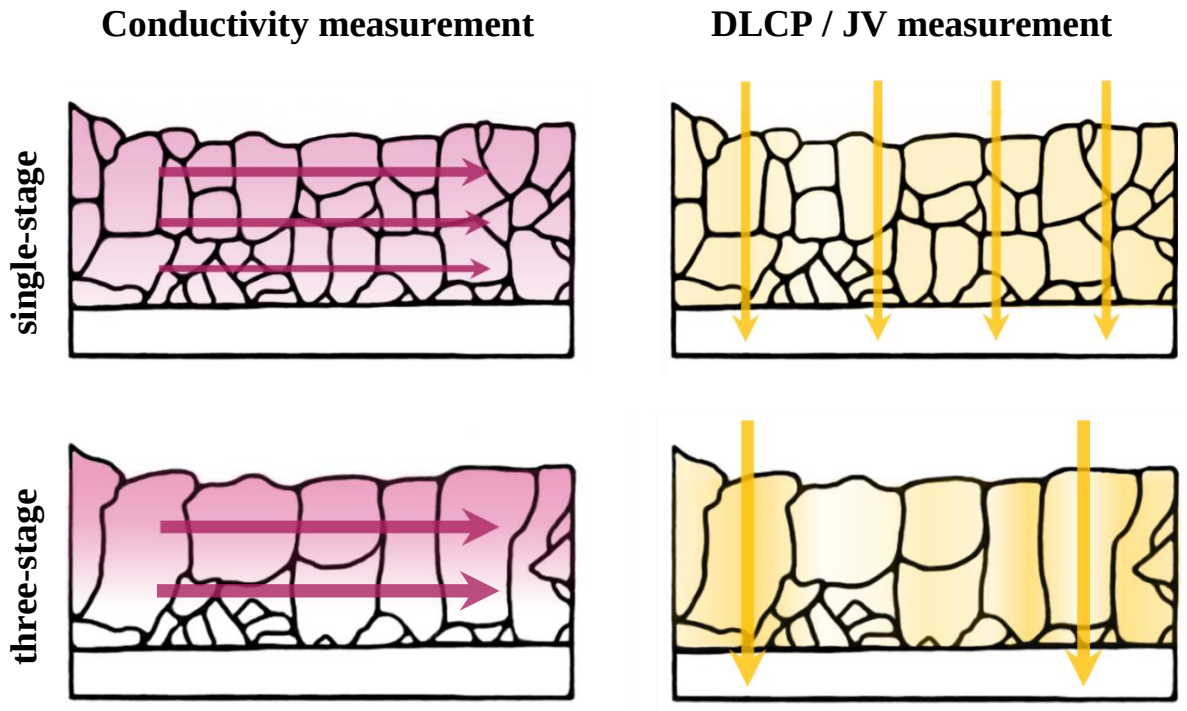

Figure 10.8 Schematic of a fine-grained (single-stage, top) and coarse-grained (three-stage, bottom) CIGS layer in case of a lateral (conductivity of thin films, left) and horizontal measurement (DLCP or IV in cells, right). Arrows show the general direction of current flow, while the intensity of color highlights probable current density.

Three of the possible sources of difference between single-stage and three-stage devices are the copper concentration, indium to gallium ratio and grain size. In the left part of Figure 10.9 presented is the same $p_R/\sigma_R(c(alk))$ relation as shown previously, this time for single-stage thin films prepared with different copper stoichiometry. As can be seen, all but the two low-Cu low-alkali thin films follow the single-stage trendline. The two outliers show decreased, rather than increased, conductivity, so the copper concentration gradient is likely not the cause of the increased conductivity in the three-stage thin films from the main series. In the right part of Figure 10.9 large-grained devices are presented. Those were manufactured using a modified three-stage process, where the resulting film had slightly bigger grains than those from the standard 3-stage process used at ZSW. Here, both the results for cells and thin films, independent of doping, fall on the three-stage trendline. This points to the process, rather than grain size itself being responsible for the change in conductivity of thin films.

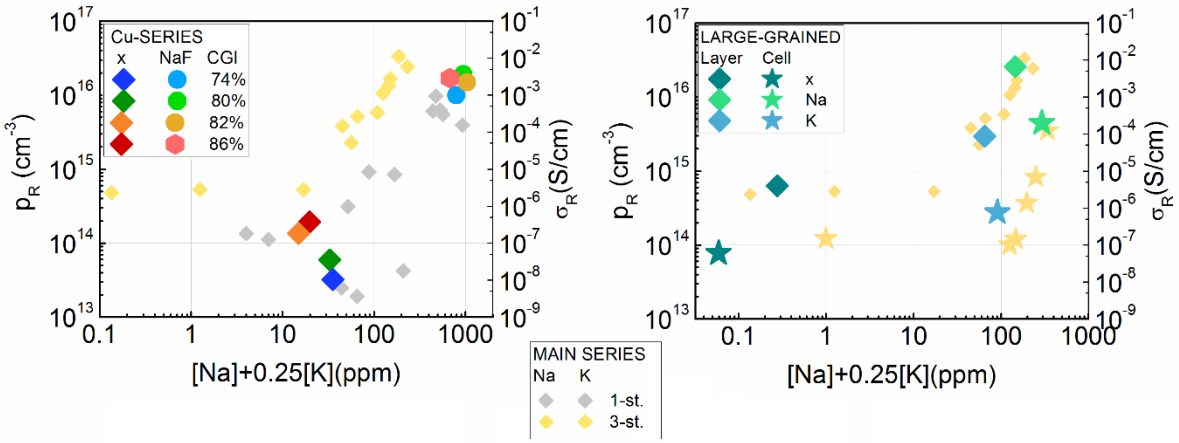

Figure 10.9 Conductivity at 200K as a function of sodium concentration for the Cu-series, comparison with results for other series described within this work (left). Comparison between free hole concentration (stars) and conductivity (diamonds) at 200K for the large-grained series and the 3 stage series (right).

Another question concerning the PDT process is whether the alkali concentration itself causes the observed changes or is it the annealing temperature. As can be seen in Figure 10.10, in the single-stage series the relation with PDT temperature is clearly visible for solar cells, while no such relation can be seen in the thin films. Unfortunately, with this samples it is impossible to determine which of the two – alkali concentration or annealing temperature in the presence of alkali metals – is more responsible for the changes in parameters, as the temperature is used to control the amount of diffusing alkalis.

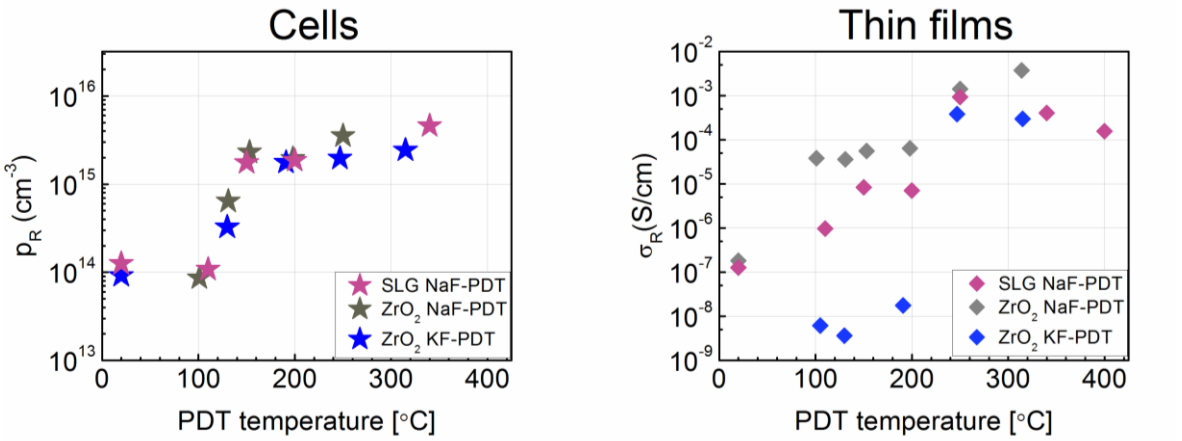

Figure 10.10 PDT temperature dependence of free hole concentration (left) and conductivity (right) of single-stage devices.

What can be deduced from the analysis presented in this chapter is that almost all of the studied devices, both thin films and solar cells, doped with sodium and potassium, and independent of the evaporation method show a similar dependence of free hole concentration/conductivity on the alkali concentration – with the major difference being that about 4x more potassium than sodium has to be used for the same effect. This all points to the alkali-effect being an intrinsic property of the CIGS absorber and not a junction/interface phenomenon.

The choice between the alkali effect being linked primarily to the PDT temperature or alkali concentration is hard to settle with the available devices – as the two are directly related to each other, with KF-PDT leading to higher alkali concentrations than NaF-PDT due to easier dissociation of KF [127].

10.2 Persistent photoconductivity

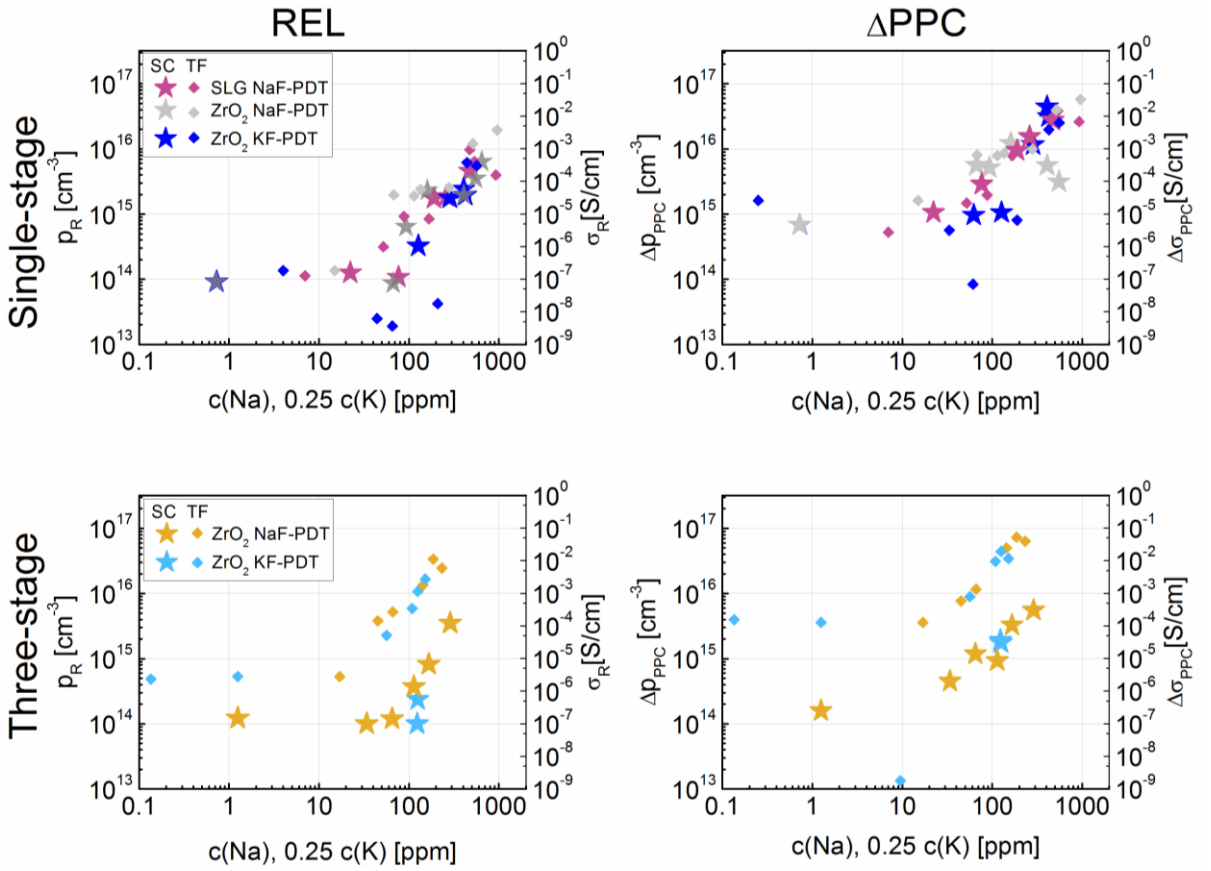

Figure 10.11 Free hole concentration (stars, left axes) and conductivity of corresponding thin films (diamonds, right axes) in Na and K-doped devices in the relaxed state (left column) and the magnitude of persistent photoconductivity effect (right column) as a function of effective alkali concentration from single-stage and three-stage devices.

Similarly as was the case for measurements in the relaxed state, the magnitude of persistent photoconductivity, here – the difference between the conductivity/free hole concentration in the relaxed and metastable state – was presented as a function of the alkali concentration. As can be seen in Figure 10.11, in almost all of the cases the shape of the dependence is virtually the same, albeit in all cases the values are about an order of magnitude higher than in the relaxed state. This points to either:

- The mechanism of PPC being directly tied to the relaxed p/σ
- Both the relaxed and light-soaked properties being limited by a common cause, i.e. by barriers at the grain boundaries and their alkali-induced reduction

As the metastable increase seems to be proportionally the same for all devices, to further study this the values of Δp_{PPC} and $\Delta \sigma_{PPC}$ were plotted in Figure 10.12 as a function of the relaxed properties.

Let first take a look at the $\Delta\sigma_{PPC}$ vs σ_R relation. **Here, the metastable increase in conductivity is equal to about a factor of 10 (black line) across almost 8 orders of magnitude**. This holds true for single- and three-stage devices; for alkali-free thin films and films doped with sodium, potassium or both (dark gray diamonds), also in the curious, low-potassium region; finally, the relation holds even for thin films prepared in other laboratory on polymer substrates (light gray)[4]. As such, it seems plausible that the magnitude of PPC is directly linked to some of the fundamental properties of CIGS that govern also the relaxed properties.

Such dependence in free hole concentration derived from DLCP is a bit more complicated. Firstly, it should be reminded that the lower limit of free hole concentration at $10^{14}cm^{-3}$ might be distorted by high series resistance and full depletion inside the grains. With that in mind, the values of Δp_{PPC} for solar cells with the lowest doping density vary from $10^{14}cm^{-3}$ up to $7\cdot10^{15}cm^{-3}$. This suggests an existence of a factor limiting p_R in this case. For devices with p_R ranging between $2\cdot10^{14}cm^{-3}$ and $2\cdot10^{15}cm^{-3}$ a linear relation between Δp_{PPC} and p_R can be seen, similar to that observed in thin films. Here, it is safe to assume that the change observed in conductivity is almost solely linked to the increase in carrier density. Finally, for the highest doping densities, the Δp_{PPC} becomes varied again.

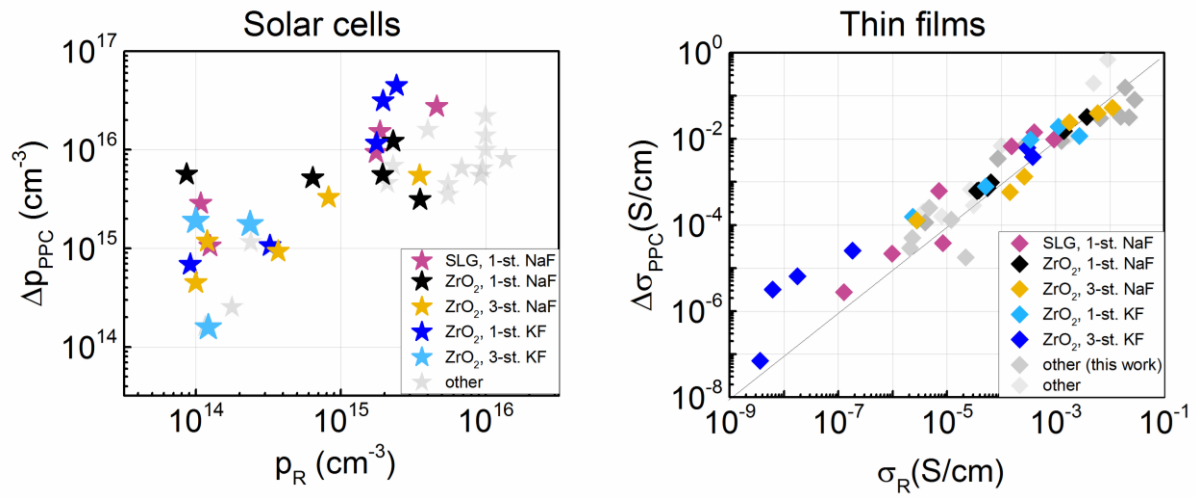

Figure 10.12 Metastable increase in the free hole concentration Δp_{PPC} as a function of relaxed free hole concentration p_R (left), metastable increase in conductivity $\Delta\sigma_{PPC}$ as a function of relaxed conductivity σ_R (right). Values from the 5 main series were compared with data for additional devices, i.e. double-PDT and large-grained CIGS (dark gray) and with devices from literature (light gray).

[4] Thin films prepared at Nantes University as a part of study of sodium-doped CIGS devices on polyimide substrates, described in Urbaniak et al.[62]

To better understand this, in Figure 10.13 the same graph is presented with color-coded effective alkali concentrations, divided into 5 main groups. First, there are the alkali-free devices (purple), with effective alkali concentrations below 30ppm. These constitute the lower end of the vertical dependence of Δp_{PPC} on p_R, with PPC of up to an order of magnitude, but in the case of thin films establish a trendline of $\Delta\sigma_{PPC}$ being about 10x higher than σ_R. Next is the low-alkali region (blue) – above 30ppm but below the threshold alkali concentration of 100ppm. Here, thin films follow the trendline, with higher relaxed conductivity and PPC proportional to it. This is not reflected in free hole concentration of cells – while the PPC is increasing just as expected, the p_R is still stuck at $10^{14}cm^{-3}$. As this behavior is not exhibited in thin films, it is likely a junction/interface effect. One possibility would be that the amount of alkali metals is still insufficient to passivate the CIGS/CdS interface, increasing recombination. This assumption is backed up by the $V_{OC}(T)$ measurements on the SLG series published in [126] (Figure 10.14), where devices with the lowest amount of sodium exhibited an interpolated $V_{OC}(0K)$ of 1.1V, about 100mV less than the theoretical value, pointing to an increased interface recombination.

The medium-alkali group (green) in both cases connects the low-alkali group with the one with maximum observed carrier density and conductivity, with PPC being proportional to the relaxed parameters. As such, it is a group for which the measured values of p_R and Δp_{PPC} are the most similar to that observed for thin films. Here, the $V_{OC}(T)$ dependence shows reduced interface recombination, and the $V_{OC}(0K)$ reaches its desired value. Thus, as it was concluded in [126] alkali doping improves not only bulk but also interface properties of CIGS devices. However, in this work only CIGS material properties will be analyzed.

Upon addition of higher alkali doses, the p_R and σ_R are no longer increased, and in case of solar cells the Δp_{PPC} is again no longer a direct function of p_R, possibly again pointing to the interface influence, this time with regards to an overabundance of alkalis, and possible formation of a secondary phase.

Lastly, there is also the low-potassium case (pink), resulting in films with very low conductivity (no DLCP measurements were successful on these samples), but still following on the $\Delta\sigma_{PPC}$ vs σ_R trendline, further suggesting that PPC and σ_R are interrelated.

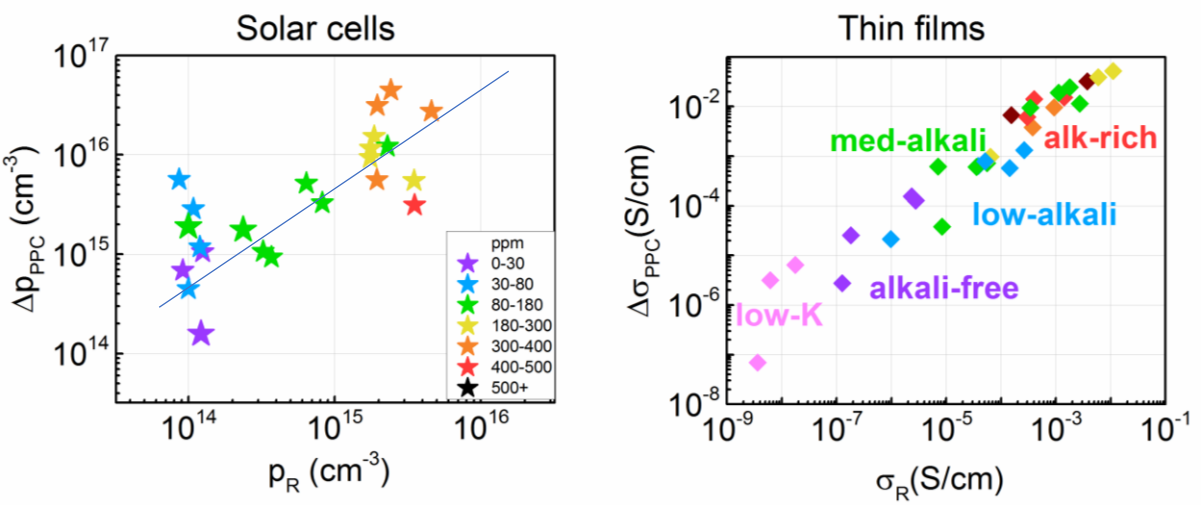

Figure 10.13 Metastable increase in the free hole concentration Δp_{PPC} as a function of relaxed free hole concentration p_R (left), metastable increase in conductivity $\Delta\sigma_{PPC}$ as a function of relaxed conductivity σ_R (right). Values from the 5 main series color-coded according to effective alkali concentration, with potassium values being divided by a factor of 4 as described previously.

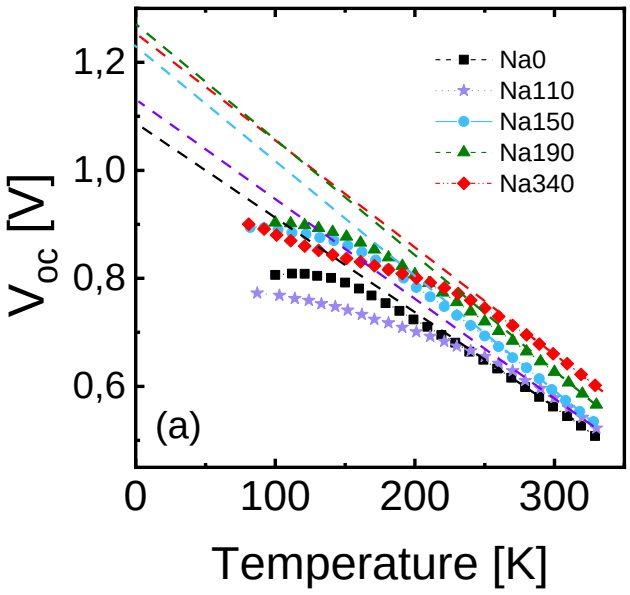

Figure 10.14 V_{OC} values as a function of temperature taken from a series of IV(T) measurements on NaF-doped SLG series presented in [126]. For devices with higher Na concentrations the interpolation of eV_{OC} to 0K is about 1.2eV, which corresponds to the E_g.. The alkali-free and low-Na devices, however, exhibit energy of about 1.1eV, 100meV lower than the bandgap. For detailed measurement protocol and raw JV data see Appendix 2.

10.3 The impact of grain boundaries

In this work for the first time two types of vital electrical characteristics were simultaneously investigated for a large range of alkali doping. Looking at the slopes of conductivity dependencies on temperature lead us to conclusion that they reflect the heights of the potential barriers at grain boundaries which are reduced upon alkali-PDT being caused by a reduction of barriers at the grain boundaries. To test this hypothesis, the results of σ(T) and DLCP measurements will be now analyzed according to the theory of Baccarani et al.[162] and supported by SCAPS [163] simulations.

The effect of grain boundaries on the conductivity of the CIGS layer is not limited to the existence of energy barriers at the GBs, but also involves a reduced overall free carrier concentration. If a p-type material has donor defects located on the grain boundaries (or an n-type material – acceptors) depletion regions are created along the GBs, which then stretch towards the middle of the grain. As the depletion width can be expressed as:

$$W_p = \sqrt{\frac{2\varepsilon_r \varepsilon_0 V_B}{e^2 N_A}} \tag{45}$$

where V_B is the barrier height, by knowing the doping density and the barrier height one can see what portion of the grain is depleted.

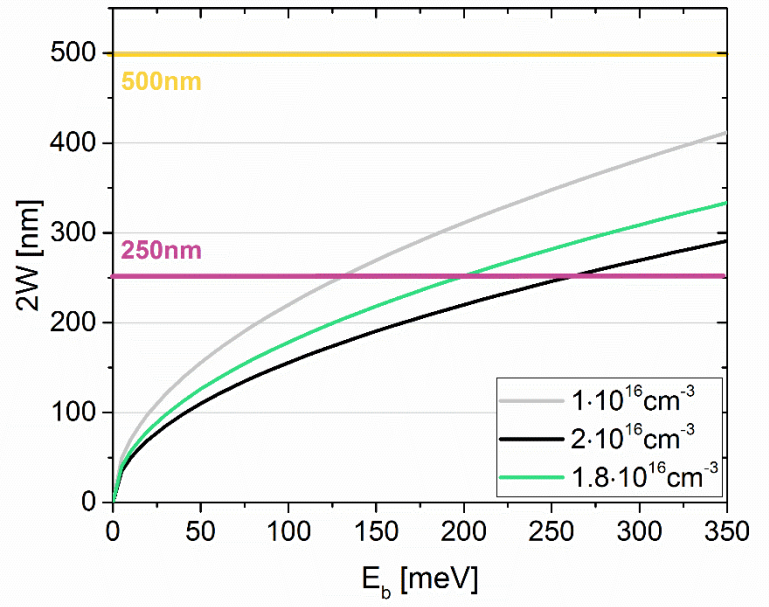

Figure 10.15 Values of double the depletion width W as a function of grain boundary barrier height for typical values of doping density expected for CIGS cells. Crossing with the horizontal lines expresses the point of a full depletion for single-stage (purple) and three-stage (yellow) films.

For a partially depleted grain, the grain size (linear) is higher than two depletion regions (stretching from both sides of the grain):

$$L > 2\,W_p \tag{46}$$

While for a fully depleted grain W_p stretches throughout the whole grain width..

If one assumes that the reason for the band bending is the presence of defect states, the barrier height will increase with the increase of their density on the GB surface up until the point of a full depletion, where the barrier height will reach its maximum. Then, upon addition of more defect states, the barrier height will be constant, but the whole energy level will be shifted downwards (in case of p-type material).

According to Baccarani et al., when mobility is limited mostly by barriers at grain boundaries, the conductivity in case of **fully depleted grains** can be then expressed as:

$$\sigma = \frac{q^2 L^2 N_V N_A \nu_c}{2k_B T\,(Q_t - LN_A)}\, exp\left(\frac{-E_A}{k_B T}\right) \tag{47}$$

, where Q_t is the planar defect density, L is the grain size in single dimension (parallel to the measurement), N_V is the density of states at the valence band edge, N_A is the shallow acceptor density and ν_c is the collection velocity:

$$\nu_C = \sqrt{\frac{k_B T}{2\pi m^*}} \tag{48}$$

Where m* is the effective mass of holes. And the activation energy E_A can be expressed as:

$$E_A = E_d - \frac{1}{2}E_g \tag{49}$$

Where E_t is the defect level.

For **partially depleted grains**[5]:

$$\sigma = \frac{q^2 L p_0 \nu_c}{k_B T}\, exp\left(\frac{-E_b}{k_B T}\right) \tag{50}$$

[5] In case of partially depleted grains, only the case when the Fermi level does not cross the defect level was taken into account, as the grains are too small for such crossing to be caused by a donor defect.

Where p_0 is free hole concentration in the neutral region, and the barrier height E_b is equal to:

$$E_b = \frac{e^2 Q_t^2}{8\varepsilon\varepsilon_0 N_A} \tag{51}$$

Conductivity is then proportional to:

$$\sigma \propto T^{-1/2} exp\left(\frac{-E_b}{k_B T}\right) \text{ for partially depleted grains} \tag{52}$$

$$\sigma \propto exp\left(\frac{-(E_d - \frac{1}{2}E_g)}{k_B T}\right) \text{ for fully depleted grains} \tag{53}$$

,where E_b is the barrier height, E_A the activation energy and E_t is the defect level above the valence band edge. Thus, the barrier height, as well as position of the defect level, may be calculated by making an Arrhenius plot of conductivity and temperature. Here, from the σ(T) measurements, barrier height was determined in three characteristic regions:

- **Low-temperature**: linear part between 100 and 200K, depending on the shape of the conductivity curve. Samples exhibiting a kink in the σ(T) characteristics were not included, as that property is likely caused by an additional effect
- **High-temperature**: the part above 300K with a strong increase in conductivity
- **LS** – taken from the LS curve below 200K (annealing out of the effect speeds up above 200K)

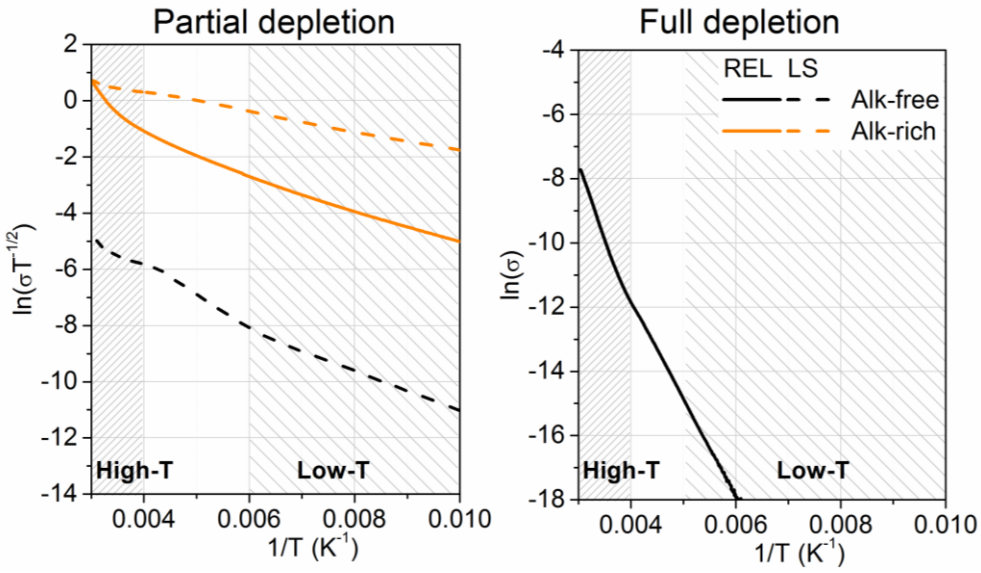

Figure 10.16 An example of a σ(T) measurement for alkali-free and alkali-rich devices with marked high- and low-temperature regions used for fitting. Different Y axes are used for fitting depending or whether a full depletion is expected or not.

As it is likely that the GBs are passivated by the alkali elements, it would be beneficial to present the barrier height E_b as a function of the alkali concentration. However, the devices studied in this work were prepared using different alkali elements, deposition methods (different grain size) and with PDT treatment taking place at various temperatures. Therefore, a common variable, effective alkali concentration at the grain boundary was introduced combining those:

$$Alk_{GB}^{eff} = c(Alk)\xi \frac{V_{grain}}{0.5\, S_{grain}} \tag{54}$$

where:

- S_{grain} is the surface area and V_{grain} is the volume of a 250nm×250nm×750nm grain for the single-stage process and 500nm×500nm×1250nm grain for the three-stage process. Surface area is divided by two, as each grain boundary is shared between two grains
- ξ takes 1 for sodium and 0.25 for potassium, as the effect of potassium is about 4x lower than that of sodium (see previous chapters)

This approach has some major weaknesses: first, it assumes that no alkalis are found within the bulk of the grain. It is however known from APT measurements that a minuscule amount of Na, in the range of 10-100ppm, does diffuse into the GI [121–123, 164].

As can be seen in Figure 10.17, activation energy in the high-temperature region does not depend strongly on the alkali concentration in the layer, which points to it being linked to the fundamental properties of the CIGS material, i.e. thermal activation of a deeper acceptor defect. According to Lany-Zunger model of the V_{Se}-V_{Cu} defect [70, 87], in this temperature range the redistribution between shallow donor and shallow acceptor states of the defect takes place and results in an increase of doping. When we then look at the low-temperature properties, it becomes evident that the activation energy depends on the alkali concentration in the film. In case of both single-stage and three-stage devices, the maximum barrier height was similar, equal to about 270-280meV. As it will lead to a full depletion of the grain[6], ln(σ) vs T^{-1} plot may be used to calculate the activation energy from donor-type defect, which would equal to:

$$E_A = E_d - \frac{1}{2}E_g \tag{55}$$

[6] According to formula (45) the depletion width for a 270meV barrier and $2\cdot10^{16}cm^{-3}$ doping density (typically assumed for CIGS) is about 130nm, enough to result in full depletion of a 250nm grain.

This would suggest a defect located at about 0.33eV below the conduction band edge. Additionally, the doping density N_A can be obtained from the activation energy in a fully depleted grain (corresponding to a maximum barrier height E_b^{max}) using formula (56) [162]:

$$E_A = E_b^{max} = \frac{e^2 L^2 N_A}{8\varepsilon_R \varepsilon_0} \tag{56}$$

where L is the average grain dimension and ε is the dielectric permittivity. By assuming relative dielectric permittivity of 10, and the grain size of 250nm we get the theoretical doping density of $1.8 \cdot 10^{16} cm^{-3}$. This is in line with the highest observed in this work doping concentration. By using this doping density and substituting it in formula (51) (this time for measurements on partially depleted grains), the concentration of donor defects at the grain boundaries can be calculated from the measured barrier height E_b (57):

$$Q_t = \sqrt{\frac{8\varepsilon\varepsilon_0 N_A E_b}{e^2}} \tag{57}$$

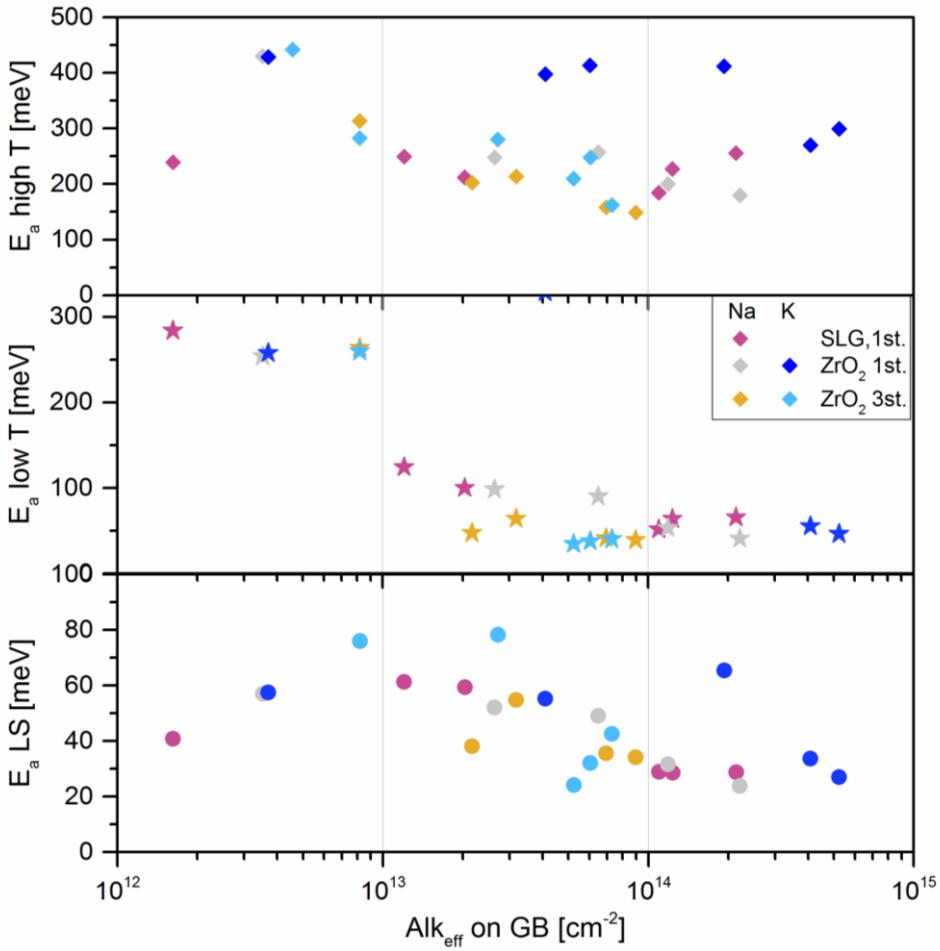

Figure 10.17 Values of the barrier height as a function of effective alkali concentration at the GBs in the relaxed state at high (top) and low temperatures (middle), and in the light-soaked state (bottom)

10.3.1 SCAPS Simulations

To test the hypothesis of reduction of grain boundary barriers with alkali elements being responsible for the change in electrical properties, experimental data was then compared with SCAPS simulations. SCAPS, namely Solar Cell Capacitance Simulator is a 1D solar cell and semiconductor simulation software, developed at the Department of Electronics and Information Systems (ELIS) of the University of Gent, Belgium, widely used to study the behavior of solar cells, including CIGS [163].

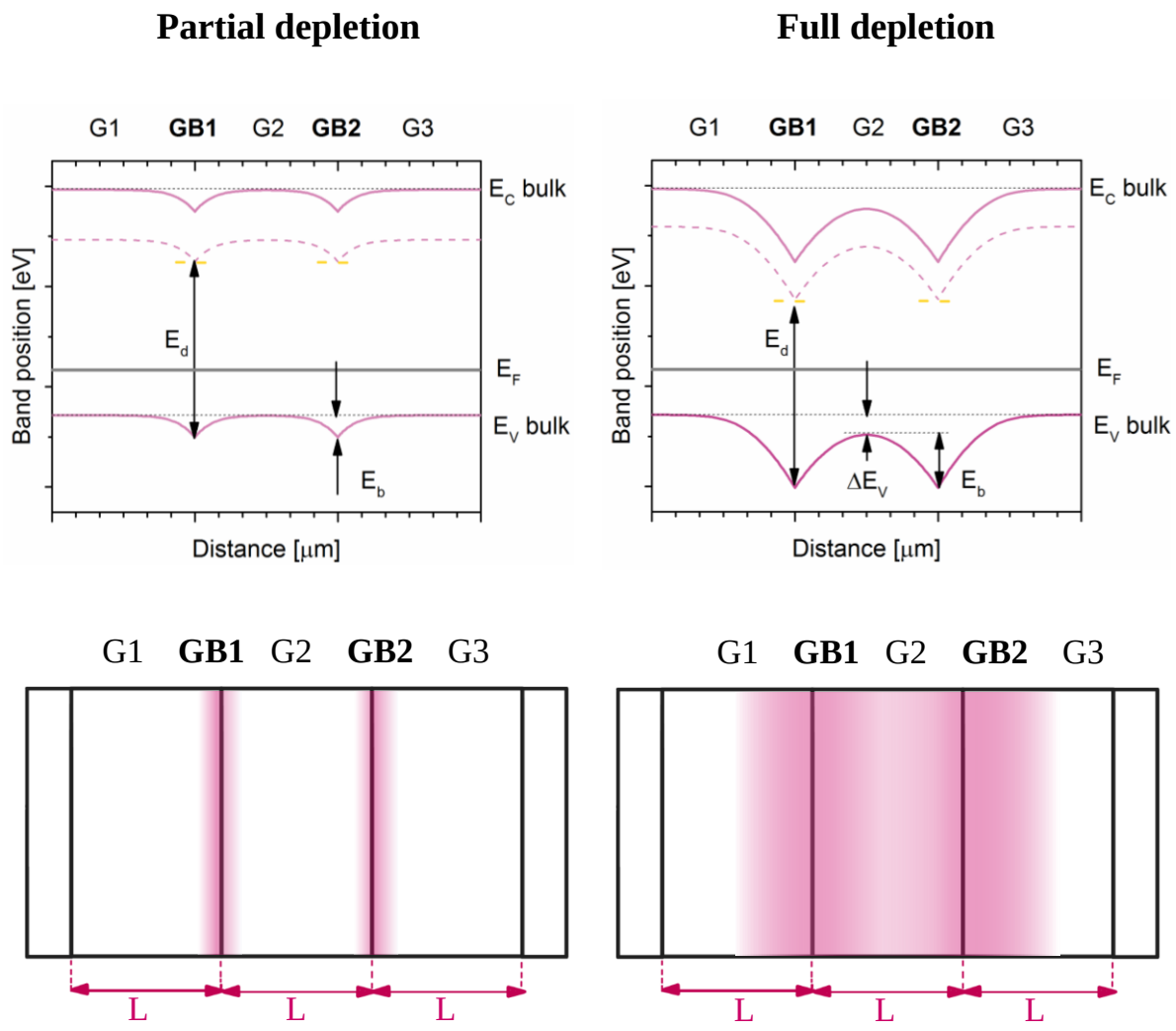

Figure 10.18 Top: Example of simulated band diagrams in case of a partial (top left) and full depletion (top right). E_C and E_V denote conduction and valence band edge, ΔE_V is the shift in the maximum valence band position (in the partially depleted case ΔE_V=0), E_b is the barrier height. Dashed line denotes the donor defect level, the donors are located only on grain boundaries (yellow). Bottom: schematic of a CIGS structure simulated with SCAPS. Purple shading corresponds to the depletion region around the grain boundary. Donor defects are assumed at the GB.

A structure mimicking thin film measurements, consisting of three CIGS grains was assumed (see bottom row in Figure 10.18). The grain width was taken as 250nm, corresponding to the L of single-stage CIGS, with shallow doping density $N_A=1.8\cdot10^{16}cm^{-3}$, as was calculated in previous chapter. On the interfaces between the grains (grain boundaries) a population of donor defects Q_t with the energy E_d relative to E_V equal to 850meV was assumed, which corresponds to the deep donor level calculated in the previous chapter from the experimental data. Such position of the donor level ensures that the amount of positive charge does not depend on the position of the Fermi level in the investigated p-type material. In analysis, only the middle grain was taken into account. A complete list of parameters used can be found in Appendix 1. In the top row, schematics of resulting band diagrams are shown. Donors on the grain boundaries result in a downward band bending, and creation of an energy barrier E_b between the grains. Once concentration of donors at the GBs is high enough, the grain becomes fully depleted and the position of the energy bands becomes affected throughout the whole grain, shifted downward by ΔE_V (see top right).

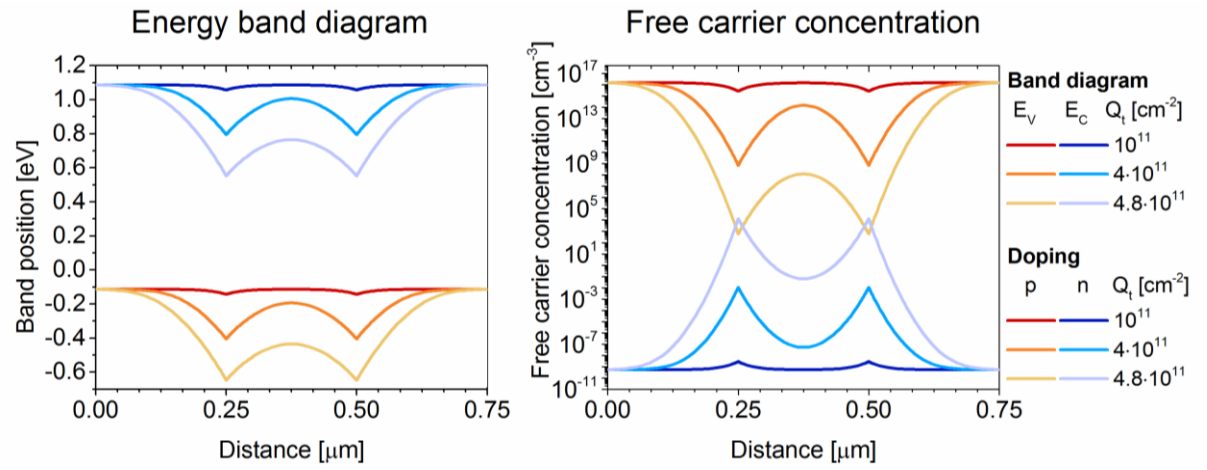

Figure 10.19 SCAPS simulation results for a 250nm CIGS grain with varied concentration of deep donors at the grain boundaries, corresponding to non-depleted grains ($Q_t=10^{11}cm^{-2}$), fully depleted grains ($Q_t=4\cdot10^{11}cm^{-2}$), and to depleted grains with type inversion at the grain boundaries ($Q_t=4.8\cdot10^{11}cm^{-2}$).

In Figure 10.19 a series of three simulations for a 250nm grain is presented. When concentration of donor defects at GBs is equal to $10^{11}cm^{-2}$, the grains are depleted only in the close vicinity of the grain boundaries resulting in small energy barriers E_b. This is reflected in the free hole concentration within the grain, equal to bulk values throughout most of the grain. Once more donors are added ($Q_d=4\cdot10^{11}cm^{-2}$), the grain becomes fully depleted, with barriers reaching their maximum value. The concentration of free holes within the grain is strongly reduced,

while the concentration of free electrons rises. If even more donors are assumed (Q_d=4.8·10^{11}cm^{-2}), the barrier height is constant, but the bands shift even more downwards. In this case, in the close proximity of grain boundaries a type inversion may be displayed, when the population of free electrons surpasses that of free holes. In our solar cells, this scenario is unlikely, as due to the small size of the grains it would require an unrealistically low free hole concentration within the grain bulk.

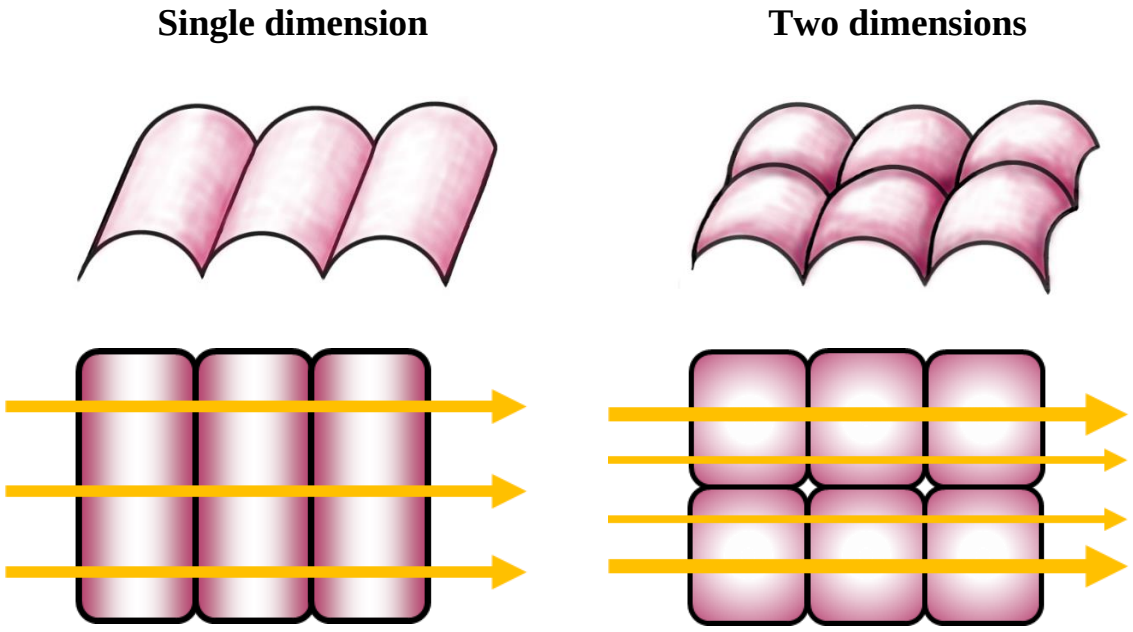

Figure 10.20 Top row – valence band bending due to donor defects at the GBs in 1D and 2D grains. Bottom row – free hole concentration reduction due to depletion regions stretching into the GB (purple) in 1D and 2D. Graphically expressed conductivity due to a difference in p (yellow arrows).

In analysis, barrier height E_b was taken as the difference between the highest and lowest position of the E_V within the middle grain. Free hole concentration within the layer was averaged throughout the middle grain, according to formula:

$$p_{ave}^{1D} = \frac{1}{L}\int_{GB_1}^{GB_2} p(x)dx \tag{58}$$

where L is the grain width, GB1 and GB2 relate to the x location of the 1st and 2nd grain boundary and p(x) is free hole concentration at the position x.

However, the free hole concentration (and, as a consequence, also conductivity) in reality depends on not only the x direction, but also depletion in the y and z directions (see Figure

10.20). Here, as the grains are columnar in shape, free hole concentration used in the comparison was approximated over 2 dimensions:

$$p_{ave}^{2D} = \frac{1}{L^2} \int_{GB_1}^{GB_2} \int_{GB_\alpha}^{GB_\beta} p(x,y)dx\,dy \approx p_{ave}^{1D} \cdot \left(\frac{p_{ave}^{1D}}{N_A}\right) \quad (59)$$

As was already discussed in Chapter 10.1.2, the 3-stage process consists of a Cu-poor and Cu-rich phases and a involves a non-uniform gallium distribution, which all result in a material with not only different grain size distribution, but also different doping density, mobility and grain boundary properties between the layers. And since the barrier height (and therefore – N_A and donor density) is calculated from the σ(T) measurements, where we likely only probe only the most conductive layer, these values might not correspond to the DLCP measurements.

With this in mind, in the later part of the study only single-stage devices will be discussed

10.3.2 Comparison between simulation results and the experimental data

As the barrier height cannot be obtained from the DLCP measurements, to be able to compare the results on thin films and solar cells, a common parameter should be used. Since the results of conductivity and free hole concentration as a function of alkali concentration follow the same trendlines, as discussed in the previous chapters, the concentration of alkali elements could be one such parameter. Here the effective alkali concentration at the GBs, Alk_{GB}^{eff}, will be used.

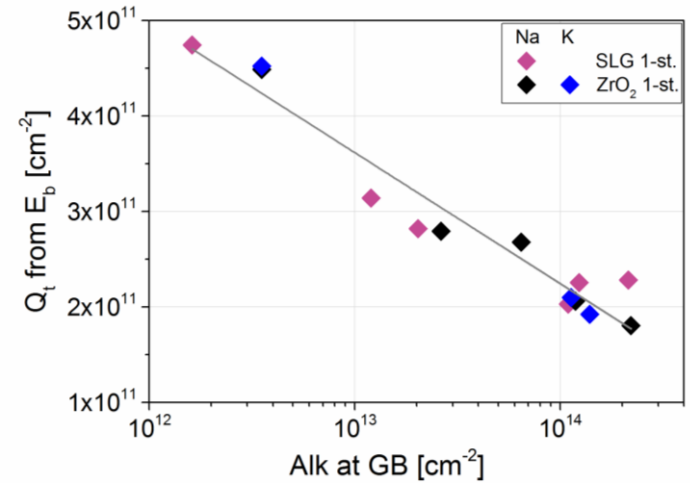

Figure 10.21 Relation between the donor concentration at the GBs calculated from the barrier height and the effective alkali concentration at the GBs calculated from (54).

First, the values of donor concentration Q_t were calculated from the barrier height for the single-stage devices, and plotted as a function of Alk_{GB}^{eff}. Then, through fitting that plot, one can estimate the donor concentration and the barrier height E_b in solar cells as well. These results are presented in Figure 10.22.

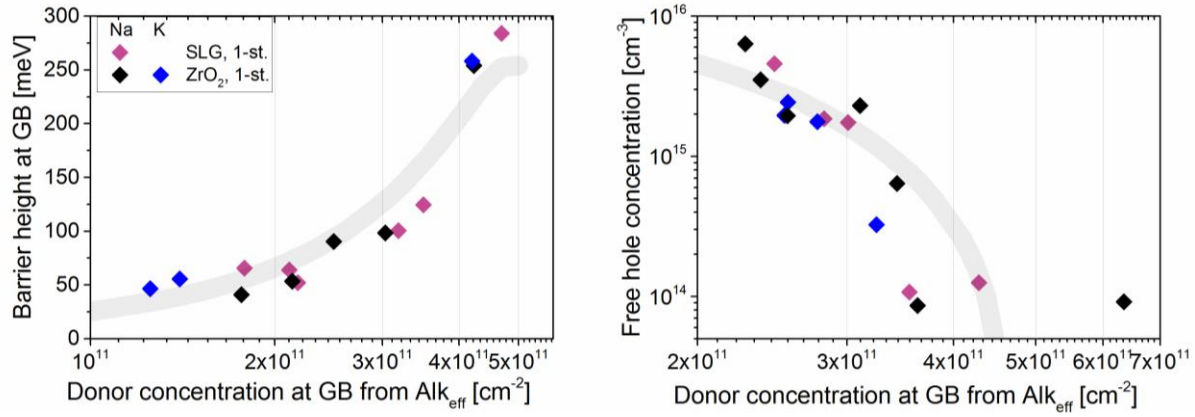

Figure 10.22 Experimental results of barrier height taken from σ(T) measurements (left) and free hole concentration (right) of single-stage thin films and solar cells as a function of the donor concentration at the GBs calculated from effective alkali concentration at the grain boundaries Alk_{eff}^{GB} (diamonds). Comparison with the simulations for a 250nm grains with $1.8 \cdot 10^{16} cm^{-3}$ shallow acceptor density as a function of donor defect concentration at the GBs (grey line).

On the left side of Figure 10.22, the barrier height at the GBs taken from σ(T) measurement on single-stage thin film CIGS is presented as a function of Q_t calculated from the alkali concentration. As can be seen, the assumption of using Q_t estimated from alkali concentration is reasonable, as experimental values of E_b derived from the slopes of conductivity vs temperature curves follow the theoretical relation for 250nm grains with $1.8 \cdot 10^{16} cm^{-3}$ shallow acceptor density calculated using equation (59). The barrier height gets reduced from about

250-280meV, which corresponds to the fully depleted grains, to about 50meV – value often reported as the barrier height in sodium-containing CIGS. In the right part of the graph, the values of free hole concentration obtained from DLCP measurements are presented. Again, experimental data follows the theoretical expectation. As the donor concentration here is a function of alkali concentration, this result confirms validity of the model attributing the apparent decrease of doping to the passivation of grain boundaries by alkali elements. In other words, in this approach the increase of doping is not due to passivation of compensating donors in the bulk of the grains or creation of additional acceptors, but is a consequence of the removal of partial depletion through passivation of defects at GB. It has to be noted that the proposed model is very simple and does not take into account all variations in the observed parameters which might come from other factors than charged grain boundaries.

10.3.3 Simulation of conductivity

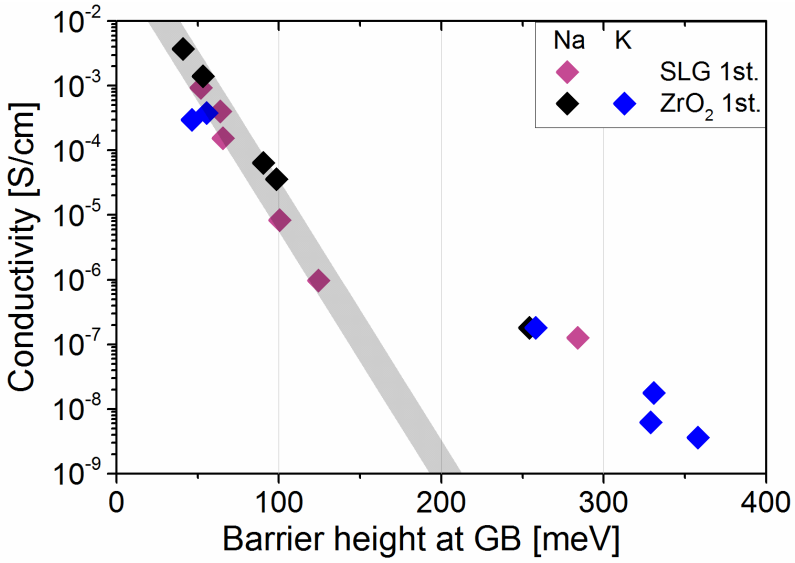

Figure 10.23 Dependence of conductivity at 200K on the barrier height at GBs. Gray line is a fit to data below 200meV. Three points at around 275meV correspond to alkali-free devices, while the 3 blue points above 300meV are the low-potassium devices.

In Figure 10.23, a relation between the conductivity at 200K and the low-temperature barrier height E_b is depicted for single-stage CIGS. In the range below 150meV, an exponential (linear in the graph) dependence of conductivity on E_b is observed, followed by a region of full depletion to about 300meV. The points above 300meV are the low-potassium devices, in which likely some additional effects are observed, and are therefore excluded from the study.

Mobility

By fitting the $\sigma(E_b)$ function, we get the value of conductivity at zero barrier, which is equal to:

$$\sigma_0(200K) \approx 0.06 \frac{S}{cm} \tag{60}$$

From that, assuming the doping density $N_A=1.8\cdot10^{16}cm^{-3}$, the maximum mobility at 200K can be obtained:

$$\mu_0(200K) = \frac{\sigma_0}{eN_A} \approx 23 \frac{cm^2}{Vs} \tag{61}$$

According to formula (50) (page 82) and assuming $m^*=0.7m_e$ the conductivity and mobility at a zero barrier height should be roughly equal to:

$$\sigma = \frac{q^2 L p_0 \nu_c}{k_B T} \approx 10 \frac{S}{cm}, \qquad \mu_0(200K) \approx 350 \frac{cm^2}{Vs} \tag{62}$$

Which are significantly higher values. This is not surprising, as the theory of Baccarani et al. assumes the major transport process to be thermionic emission. According to Kim et al. [165] this can lead to a severe overestimation of mobility. The limited applicability of the thermionic emission model of the transport over grain boundaries and the need to replace it with the diffusion model was also demonstrated in the work of Wiśniewski and Zabierowski on the DLTS signal in CIGS [166]. The influence of limited number of available free holes due to depleted regions around the GBs in 2-3D was also not taken into account in this model.

Free hole concentration

Looking at the left side of Figure 10.24, where $p_{ave}(E_b)$ is presented for different temperatures, it is clear that as long as the grains are only partially depleted, the doping density does not depend on temperature. On the right, the dependence of p_{ave} on barrier height is shown for N_A=1.8·10^{16}cm^{-3} and 3.4·10^{16}cm^{-3} (will be used in Chapter 10.4). For the sake of calculating the theoretical curve, which would take into account partially depleted regions and their dependence on the barrier height, the simulated value of p_{ave} for N_A=1.8·10^{16}cm^3 was fitted to the expression:

$$p_{ave}(E_b) = 1.8 \cdot 10^{16} cm^{-3} \cdot \exp\left(\frac{-E_b}{111meV}\right) \tag{63}$$

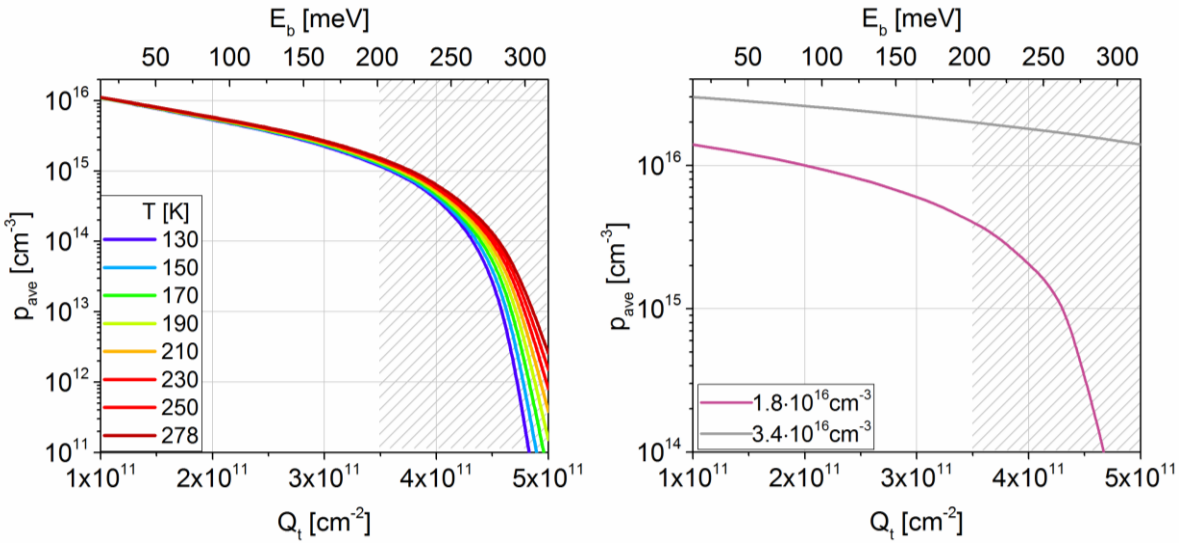

Figure 10.24 Dependence of simulated average free hole concentration within the absorber (p_{ave}) on the barrier height E_b for different temperatures (left). Dependence of p_{ave} on E_b for 1.8·10^{16}cm^{-3} and 3.4·10^{16}cm^{-3} shallow doping density at 200K (right).

Conductivity

The values of μ_0 and p_{ave} approximated using expression (63) can be used further to calculate the theoretical conductivity, plotted in Figure 10.25 as a wide, purple line:

$$\sigma(E_b) = N_A \cdot q \cdot \mu_0 exp\left(\frac{-E_b}{k_B T}\right) \tag{64}$$

Here, T is equal to 200K. As formula (64) is valid in one dimension, it will not take account for the reduced free hole concentration due to depletion in the Y and Z directions. To mitigate it, additional lines (labeled 2D and 3D) representing σ_{2D} and σ_{3D} are plotted alongside, which accommodate such depletion:

$$\sigma_{2D}(E_b) = N_A \cdot \left(\frac{p_{ave}}{N_A}\right) \cdot q \cdot \mu_0 exp\left(\frac{-E_b}{k_B T}\right) \tag{65}$$

$$\sigma_{3D}(E_b) = N_A \cdot \left(\frac{p_{ave}}{N_A}\right)^2 \cdot q \cdot \mu_0 exp\left(\frac{-E_b}{k_B T}\right) \tag{66}$$

The most accurate values should occur for the 3D case. Looking at Figure 10.25, this seems to be the case.

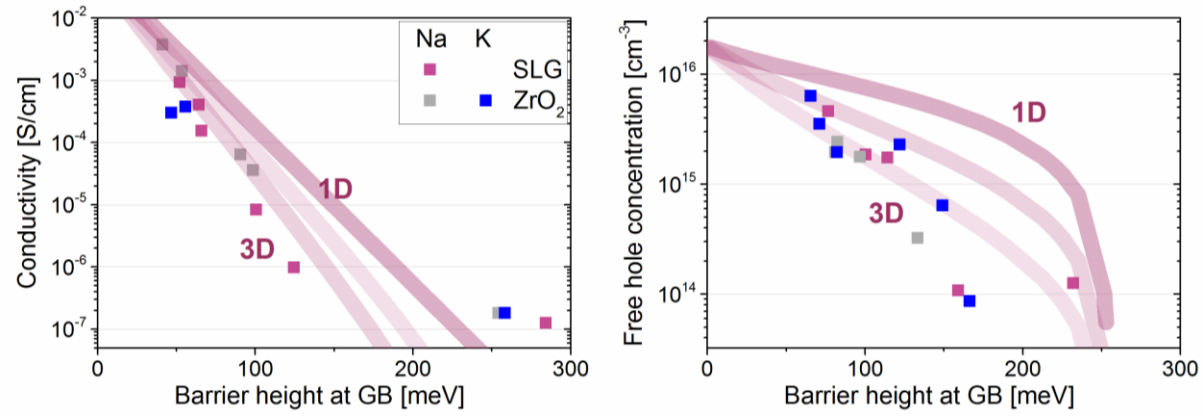

Figure 10.25 Left: values of conductivity at 200K for single-stage thin films doped with sodium and potassium, plotted as a function of measured barrier height (left). Three points at about 280meV correspond to a fully depleted grain, where the barrier height no longer increases. Right: values of free hole concentration at 200K for single-stage solar cells as a function of E_b estimated from alkali concentration.

Additionally, the values of free hole concentration from DLCP were compared with the calculated, theoretical values of p_{ave}, and while the match is not as good as in case of conductivity, the values, as well as the trendline are reasonably close in the 3D prediction. What is important to note, is that both the conductivity and free hole concentration reach a plateau at about 200meV.

The model used here fits well to the experimental data, however there are several assumptions made in it. Some of them include:

- The model assumes uniformly sized grains perpendicular to the direction of the current flow. It does not account for the variation in sizes between grains as well as their orientation.
- The impact of alkali elements on the grain interior is omitted, while APT data show some amounts of Na, in the order of 10-100ppm, within the GI.
- The impact of ionized impurity scattering as well as trapping at defects in the grain interior on the mobility is omitted. It is probable that the barrier height observed for the high-alkali thin films is actually caused by one of this effects.
- Thermionic emission transport over grain boundaries is assumed

Summing up, I showed that passivation of grain boundaries by alkali metals might be held responsible for majority of the observed effects, although additional impact of doping inside the grains cannot be excluded. Specifically, the differences between K and Na doping (see Figure 9.11) can be explained by bulk doping coexisting with grain boundary passivation in case of Na, while K acts only at grain boundaries.

10.4 Grain boundaries and persistent photoconductivity

As in the light-soaked state both the conductivity of thin films and the free hole concentration measured on solar cells are about 10x higher than in the relaxed state, independent on the concentration of alkali elements, persistent photoconductivity is likely an inherent property of the CIGS film. Such processes could be, for instance:

- Free hole concentration being temporarily increased due to amphoteric defect pain V_{Se}-V_{Cu} as proposed by Lany and Zunger [86], while taking into account the impact of barriers at the grain boundaries – limiting both the doping density averaged over the grains and the position of the Fermi level with regards to the transition energy
- Grain Boundary Controlled Transport (GBCT), a model proposed for GaN [167], where upon illumination the photo-generated holes would be swept into the grain interior through the electric field at the GB, and after cooling down would have to cross the barrier using thermal energy, resulting in the PPC.

Since annealing-out of the metastable free hole concentration Δp_{PPC} takes place in temperatures above 200-250K, only the linear part below 200K, far from the characteristic "bump" observed in the $\sigma_{LS}(T)$ curves may be used to assess the barrier height.

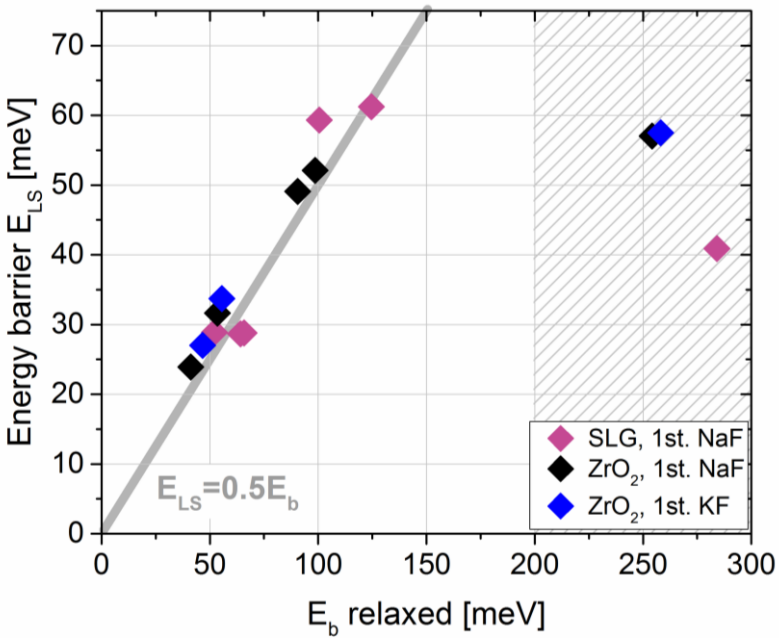

Figure 10.26 Relation between the measured barrier height in the relaxed (low-temperature) and light-soaked state for single-stage devices. Shaded part covers the region of full depletion in the relaxed state, where the relations used in this chapter may no longer hold true.

For thin films that were only partially depleted in the relaxed state (E_b below 200meV) the barrier height in the metastable state is about half of that in the relaxed state. As barrier height is proportional to:

$$E_b \propto \frac{Q_t^2}{N_A} \tag{67}$$

there are three possible cases:

1. PPC does not involve the defect states at grain boundaries, and the barrier height reduction is caused by increasing the doping density N_A within the grain bulk
2. PPC acts at the grain boundaries, passivating defect state and thus reducing Q_t
3. both passivation of the defect states at the GB and bulk doping are involved

In Figure 10.27, experimental values of the conductivity at 200K and barrier height in the relaxed and metastable state are presented for the single-stage thin films. As can be seen, in the samples exhibiting in the relaxed state E_b of 100meV and less, the metastable state falls roughly on the trendline established by the relaxed state. This would point to the 2nd case of PPC, namely the passivation of grain boundaries without the subsequent increase in doping density in the grain bulk.

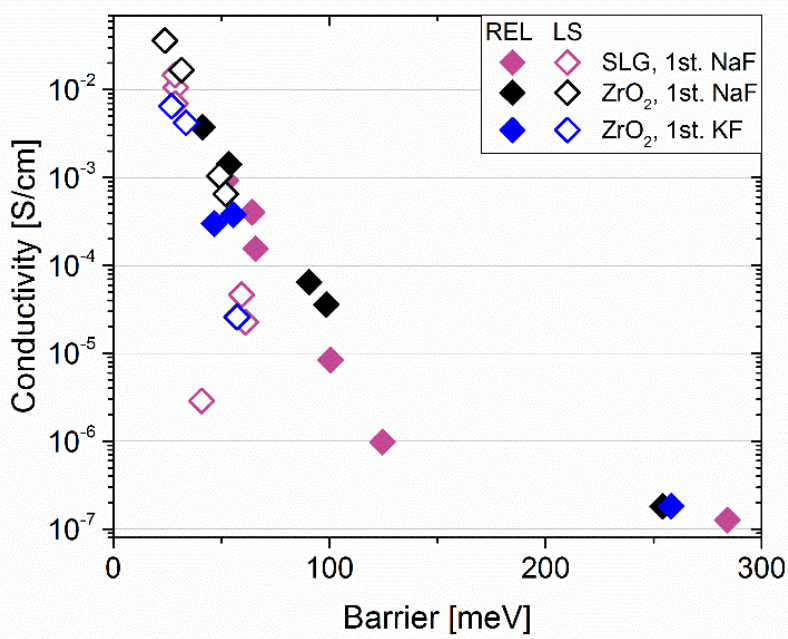

Figure 10.27 Values of conductivity at 200K in the relaxed (solid diamonds) and metastable state (open diamonds) as a function of the barrier height determined from the slope of the σ(T) dependence.

The samples with higher E_b, on the other hand exhibit significant decrease in the barrier height, even below that observed in the low-E_b thin films, while their conductivity seems not to be determined by the E_{LS} but rather σ_{REL}. It is worth noting that the model used here might not work best on the high-barrier devices, as those correspond to a full or nearly full depletion within the grain interior.

In this work, I will not focus on the combined, 3rd case, as the used model may not correctly account for both effects at the same time, and will instead look at the first two options – PPC being caused by a metastable increase in the doping density withing the grain interior (1st), and by passivation of defects at the grain boundaries without the change in the N_A(2nd).

10.4.1 Case 1 – Persistent photoconductivity as a result of increased doping within the grain interior

In case 1, where defect states at GBs remain unaffected, the barrier height is reciprocal to the doping density. Thus, by knowing the barrier height in the relaxed and light-soaked state, the increase in doping Δp_{PPC} can be obtained:

$$\frac{N_A + \Delta \boldsymbol{p_{PPC}}}{N_A} = \frac{E_b^{REL}}{E_{LS}} \tag{68}$$

In the theory of Lany and Zunger, the value of Δp_{PPC} depends on the position of the Fermi level with regards to the transition level ε – when the E_F falls below ε in the relaxed state, most of the metastable defects are found in the donor configuration, leading to higher PPC, while when E_F is above ε, most are already in the acceptor state, leading to lower PPC. As the sodium-rich devices exhibit E_F far below suspected ε[7], one may assume that Δp_{PPC} will be constant between samples (Na-free films are not investigated in this chapter, as a change between a full and partial depletion likely occurs during LS). In Figure 10.28, experimental results are plotted together with a theoretical line for $N_A=1.8\cdot10^{16}cm^{-3}$ and $\Delta p_{PPC}=1.6\cdot10^{16}cm^{-3}$, which was the best fit to data:

[7] About 0.1eV above E_V, while typical values for ε found in the literature span between 0.19eV and 0.25eV

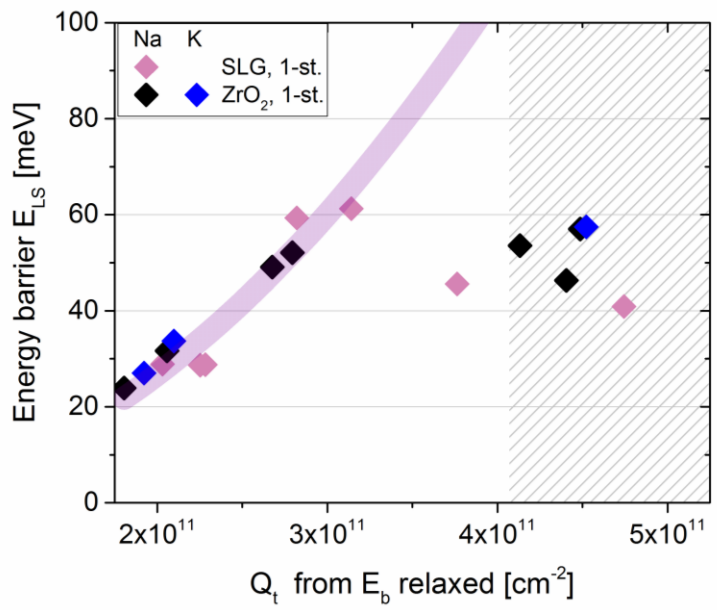

Figure 10.28 Values of the energy barrier in the metastable state E_{LS} plotted as a function of donor defect density at the GBs, together with theoretically calculated curve assuming $\Delta p_{PPC}=1.6\cdot10^{16}cm^{-3}$. Shaded area corresponds to the full depletion region, where such relation does not apply.

In Figure 10.28, experimental values of relaxed and metastable conductivity were plotted as a function of donor concentration Q_t. In the same plot, theoretical dependence of conductivity in the relaxed and LS state on Q_t was presented in the form of solid and dashed lines respectively.

Theoretical σ in the relaxed state was calculated as:

$$\sigma(E_b) = N_A \cdot e \cdot \mu_0 exp\left(\frac{-E_b}{k_B T}\right) \tag{69}$$

for $N_A=1.8\cdot10^{16}cm^{-3}$ and E_b calculated using formula (51). In the LS state:

$$\sigma_{LS}^{THEOR}(Q_t) = (N_A + \Delta p_{PPC}) \cdot q \cdot \mu_0 exp\left(\frac{-E_{LS}(Q_t)}{k_B T}\right) \tag{70}$$

where $N_A=1.8\cdot10^{16}cm^{-3}$, $\Delta p_{PPC}=1.6\cdot10^{16}cm^{-3}$ and:

$$E_{LS}(Q_t) = \frac{Q_t^2}{8\varepsilon\varepsilon_0(N_A + \Delta p_{PPC})} \tag{71}$$

Value of mobility at zero barrier height μ_0 was assumed to be the same in both relaxed and light-soaked state, although in reality it might be slightly different due to i.e. increased ionized impurity scattering at higher doping density. Values of conductivity were also calculated assuming reduction in the free carrier concentration due to depletion at GBs in 1 to 3 dimensions.

As can be seen in Figure 10.29, the experimental and theoretical values are reasonably close:

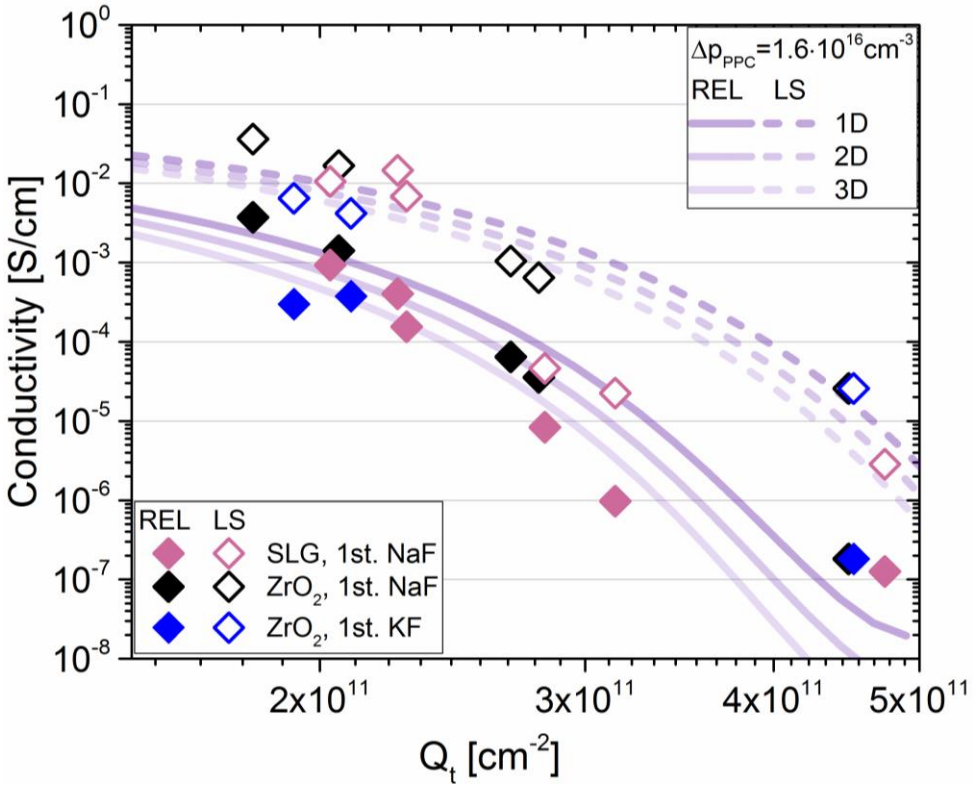

Figure 10.29 Experimental values of conductivity in the relaxed (solid diamonds) and metastable state (open diamonds) as a function of planar concentration of donor defects at the GBs Q_t. Theoretical dependence of conductivity on the Q_t for total doping density of $1.8 \cdot 10^{16} cm^{-3}$ in relaxed (solid line) and $3.4 \cdot 10^{16} cm^{-3}$ in the metastable state (dashed line). Gradually lighter lines correspond to reduction in hole concentration due to depletion regions being considered in 1 to 3 dimensions.

10.4.2 Case 2 – Persistent photoconductivity as a result of passivation of donors at the grain boundaries

The second extreme case assumes that the concentration of shallow acceptors N_A is kept constant before and after LS, and the only change is caused by the light-induced passivation of donor states at the GBs. Then, planar concentration of donor defects in the LS state Q_t^{LS} can be expressed as:

$$Q_t^{LS} = Q_t^{REL} \sqrt{\frac{E_{LS}}{E_b^{REL}}} \tag{72}$$

If we then assume the LS state to be one, where planar defect density was reduced according to formula (72), and plot it as a function of Q_t in the relaxed state, we will observe a higher discrepancy than in case of increase in the doping density (Figure 10.29), but again reasonably close to the experimental results.

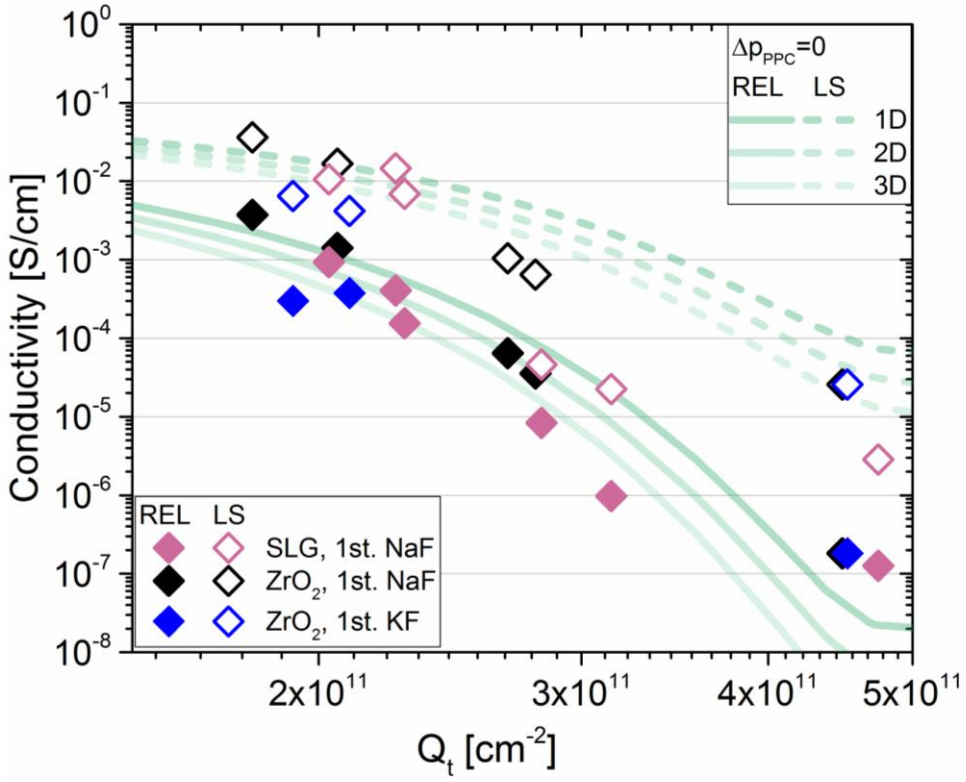

Figure 10.30 Experimental values of conductivity in the relaxed (solid diamonds) and metastable state (open diamonds) as a function of planar concentration of donor defects at the GBs in the relaxed state Q_t. Theoretical dependence of σ on the Q_t in the relaxed state in the relaxed (solid line) and metastable state created by reducing the donor concentration (dashed line). Gradually lighter lines correspond to reduction in hole concentration due to depletion regions being considered in 1 to 3 dimensions.

10.4.3 Comparison

One of the biggest mysteries when it comes to the PPC is the relation between the relaxed and light-soaked conductivity which are proportional to each other across multiple orders of magnitude (Figure 10.31). As can be seen in that figure, neither the theory of passivating grain boundaries (2nd case), nor the one with a metastable increase in the free hole concentration (1st case) by themselves seem to adequately represent that relation, although the theory of an increase of the in-grain doping seems preferable. In both cases slope of the relation is smaller than in the experiment. In order to achieve the same slope, the exponential terms, i.e. the barrier height, should be equal in both the relaxed and metastable state. This, however, is in direct contradiction to the relation shown in Figure 10.26, where E_A in the metastable state is roughly 2x lower than in the relaxed state (even more so for the alkali-free films). Again the simplifications of the thermionic emission transport model might be responsible for this discrepancy. The application of the diffusion transport model introduced by Kim and Khondker [165] should help to solve the puzzle.

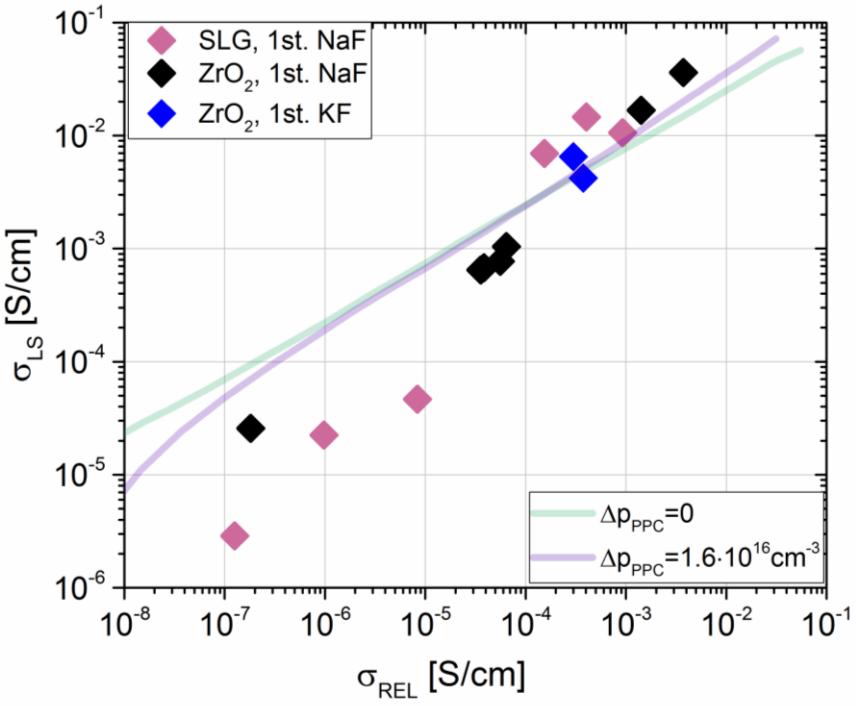

Figure 10.31 Relation between conductivity in the relaxed σ_R and metastable state σ_{LS}, for experimental data on single-stage films (diamonds), as well as theoretical dependence for cases where PPC was created through passivation of defect states at GBs (2nd case, green line) and by introducing additional free carriers into the grain interior (1st case, purple line).

11 Conclusions

11.1 The effect of sodium PDT

The effects of sodium-PDT observed in this work are fairly straightforward and fit well to the literature data. Those include:

- Increase in the free hole concentration observed by DLCP
- Increase in conductivity in thin films
- Reduction of the slope in the σ(T) measurements (influence on mobility)
- Increase in the V_{OC} in devices with increasing sodium content, likely tied to the increased free hole concentration
- Increase in the FF, likely caused by improved front interface properties [126] and reduction in the R_S (increased conductivity)
- Reduction of the secondary barrier observed at forward bias in the JV measurements on solar cells (Appendix 2)

All of the above show a dependence on sodium concentration, which is the same between thin films and solar cells. This points to the impact of sodium being linked to the CIGS layer itself rather than any of the interfaces. Additionally, the increase in conductivity is observed over double the orders of magnitude of free hole concentration increase, pointing to sodium being responsible for both increase in carrier density and their mobility. The important point, for which both experimental and simulation evidence were put forward in this work is: to explain the increase of doping after alkali treatment the creation or removal of point defects within the grain interior is not needed. Passivation of grain boundaries can account for the observed phenomena. This statement does not exclude the possibility that in-grain doping, especially at high PDT temperatures, also contributes somewhat to the overall increase of free hole density and conductivity. However, this effect seems to be minor compared to the GB-related phenomena.

In cases where excessive amount of sodium was used, it led to a reduced conductivity compared with regular Na-rich case (possibly due to neutral Na_{Cu} replacing V_{Cu} acceptors [168]). In extreme cases, it may cause delamination from the substrate, especially in case of Mo-coated glass, as was observed for the SLG/SiO_xN_y/Mo based solar cell with NaF PDT at 400°C.

11.2 Differences and similarities between sodium and potassium effect

In general, both solar cells and thin films with added potassium behaved very similarly to those doped with sodium, albeit 4 more potassium was needed for that effect to take place. This can be either a result of temperature being the dominating factor in PDT (and as KF dissociates easier than NaF, more of it goes into the layer at the same temperature) or potassium being weaker at passivating defects.

The main difference between sodium and potassium effect was that contrary to solely beneficial effect of sodium, devices doped with low amounts of potassium, described in this work as low-K, exhibited drastically reduced conductivity, free hole concentration and efficiency as compared with alkali-free cells and thin films. This is likely a result of an additional phase forming at the grain boundaries at low temperatures.

11.3 Role of alkali elements on the grain boundaries

What we do know is that the effects of potassium and sodium are observed in both solar cells and in thin films.[8] Exploring the results of alkali-doping not only on solar cells but in parallel also on thin films allowed to clearly distinguish the phenomena originating in the CIGS layer, rather than the junction or the back contact. In literature, there are multiple reports linking the K-related improvement with the CdS/CIGS junction, i.e. through depletion of Cu and enrichment of Cd, resulting in the type inversion closer to the junction [107, 108, 135]. And although potassium is indeed most often segregated towards the surface of the CIGS layer, it is likely that it also causes Cu depletion at grain boundaries further away from the junction (as potassium is found mostly on GBs). What further points to the GB effect of potassium is that in CIGSe absorber, potassium is most readily found at grain boundaries, with only a small fraction penetrating into the grain bulk [121, 169, 170]. The same can be said about sodium – it is, as well, mostly found on the grain boundaries and towards the interfaces, although a minuscule amount can be also found within grain bulk.

[8] This may not be immediately obvious as the DLCP measurements for low K are missing. This was caused by very bad quality of the low-K solar cells making the measurements impossible.

One theory that would link the existence of alkali elements at the grain boundaries with an increased conductivity and free hole concentration is a model in which the electrically active defects at the GB's – be in donor defects In_{Cu} or V_{Se} or dangling bonds – get passivated by the alkalis, either directly or through catalyzing a passivating reaction. This model would explain why comparably more potassium is needed for the same beneficial effect – as due to the greater atomic radius of K the formation energies of defects such as K_{Cu} or K_i are considerably higher than their Na counterparts [171]. The GB passivation theory is partially backed up by the study of Raghuwanshi et al. [56][9], where grain boundaries which were detrimental to the device performance were characterized by enriched Cu and low Na concentration, while those which effect was beneficial to the device performance had Cu depletion and high concentration of sodium. It is worth noting here that, unlike the case of silicon solar cells, in CIGS grain boundaries have both a positive and a negative impact, with epitaxial devices showing consistently lower efficiency that this of alkali-doped polycrystalline ones [50, 51, 172]. If we think of the model of defect-related downward band-bending at the GBs, it can be achieved both through electrically active defects (i.e. donors), and through a stoichiometry-induced change in the bandgap (i.e. through Cu depletion), and would result in:

- Creation of a hole barrier related to the band bending, which reduces hole mobility[10]
- Creation of depletion regions, reducing the effective doping within the grain bulk
- Better separation of minority charge carriers and their channeling through GBs into respectable electrodes

Additionally, grain boundaries might help to reduce the overall defect density within the grain interior through segregating defects at the surface [173]. These points suggest that there is an optimum between the lack of grain boundary barriers and big, unpassivated barriers as in case of alkali-free CIGS. Such an optimum could be, for instance, a grain boundary with no electrical charge (alkali-passivated electrically active defects) but with enough Cu depletion to slightly shift the VBM downwards.

---

[9] Partially, because an alternative theory that would fit with the results of Raghuwanshi et al. would be the bandgap widening at the GBs due to a change in stoichiometry, and sodium impacting that stoichiometry

[10] As the grains in commercial-grade CIGS are typically columnar, this would not impact the performance significantly

In this work, this hypothesis was studied using the theory of Baccarani et al. [162], a modified version of Seto's model of grain boundary activity [154]. In it, traps at the GBs lead to a downward band bending, creating a hole barrier (in case of p-type material). By plotting the values of potential barriers at the GB's as a function of alkali concentration (see Figure 10.17) it becomes evident that they are decreasing with an increase in alkali concentration, from about 280meV in the alkali-free case to 50meV in the alkali-rich devices. Those values are consistent between the small-grained, single-stage devices and three-stage, large grained ones.

The shallow doping density was then estimated from the alkali-free devices, and was found to be equal to about $2 \cdot 10^{16} cm^{-3}$, slightly higher than the highest doping density observed in DLCP measurements. By then further using the theory of Baccarani and Seto to estimate the planar density of donor defects at the GBs from the measured barrier height and comparing those with simulations, a good match between the theoretical and experimental conductivity and free hole concentration was found. **This points to barriers at the grain boundaries being responsible, at least in a large part, for the decrease in free hole concentration and conductivity (and as such – also mobility), as well as the role of alkali element in passivating GBs**. Such conclusion for the first time was supported by experimental data on samples with alkali content changing in the wide range in a controlled manner.

Barriers at the grain boundaries are likely to impact the persistent photoconductivity as well, although most likely indirectly, through a reduction in the free carrier density. The observation of the linear relationship between dark conductivity and persistent photoconductivity points to the conductivity in both states, relaxed and metastable, depending on the same factor. Explanation of this behavior by similar impact of grain boundaries in both cases is simple, but not without drawbacks. Most of the available theories point to the effect of PPC being linked to an increased doping within the grain bulk, either directly through a change in charge state of an amphoteric donor, or indirectly through grain-boundary assisted separation of electrons and holes. To the role of grain boundaries in the PPC points the fact that very little PPC is observed in epitaxial solar cells, although it might also be explained by lower concentration of metastable defects in single crystals. There is a possibility that some dislocations might have similar electric properties to grain boundaries [174], but their overall influence on the conductivity should be lower than in case of GB.

12 Further work

12.1 Open questions

There remain a few open questions:

Are the alkali elements acting purely on the grain boundaries, or is there a contribution originating also from the grain interior? This is more likely to occur in NaF-treated devices, due to better diffusion into the grain bulk. Coincidentally, thin films doped with high concentrations of Na exhibit better conductivity than those with K.

Then, the value of around 50meV activation energy/barrier height remains even after addition of high amounts of alkalis. This may point to:

- existence of a defect population that is impossible to passivate using alkalis
- a different grain boundary stoichiometry. In an APT study of Cojocaru-Mirédin et al., the difference in bandgap between grain interior and GBs in alkali-rich devices was equal to 60meV [27]. Similar observations were made by Keller et al. using EELS (20meV [175]) and Stokes et al. through calculations from APT data (79meV [176]).
- band fluctuations
- once barriers become lower and free hole concentration becomes high throughout most of the grain, the reduction of mobility due to scattering becomes non-negligible.

There is also the relation between the conductivity of thin films σ and the hole concentration in solar cells p, where for each order of magnitude of p increase due to alkali incorporation, there is a roughly two-order increase in conductivity. This relation would suggest that the mobility has to rise hand in hand with free hole concentration. This is somewhat consistent with the barrier model, as the GB barriers lead both to a decrease in mobility and cause depletion within the grain bulk, but theoretical explanations tend to show a different rate of increase of p and μ.

Unknown is the type of species responsible for the grain boundary effect. Although bandgap widening probably plays a role in the VBM offset, by itself it should not result in an increased recombination, which was observed in the $V_{OC}(T)$ measurements. Thus it is likely that the culprit is a donor defect. Possible candidates for alkali-induced passivation include In_{Cu} donor being replaced by Na_{Cu}, or the V_{Se} vacancy being oxidized with the help of Na. As oxidation

has been found more on the detrimental GBs, it would point to the In_{Cu} being responsible. There are numerical studies where the formation energy of Na_{Cu} was lower than In_{Cu} [48, 141, 143, 144], but it is still unclear whether Na/K can actually push In out of the already occupied lattice site of Cu during a PDT treatment.

12.2 Further work

In order to better understand the effects outlined in this work and answer some remaining questions (i.e. those from previous chapter), it would be beneficial to further investigate the relationship between grain boundaries and electrical properties of CIGS. While one of the most obvious ways to investigate it would be through measurements on films with different grain sizes, it would likely prove to be impossible as the grain size is directly correlated with evaporation protocols and stoichiometry of the layer [177]. This issue was already visible with the three-stage devices shown in this work, where difference in stoichiometry along the thickness of the layer made comparison between thin films and solar cells not straightforward. Therefore for this type of studies uniform, single-stage films are preferable.

A better way to look into alkalis and the GBs would be to include elements such as cesium and rubidium (heavy alkali). Their effect on solar cells performance is somewhat similar to that of lighter alkalis, and due to a higher ionic radius they tend to diffuse less into the grain interior. As such, their impact should be more on the grain boundary/interface properties. Additionally, as copper depletion at the GBs is typically observed at the GBs, samples with different Cu/(Ga+In) ratios could be measured and compared.

On the simulation side, use of 2D simulation software would be beneficial to study the effect of the grain boundaries perpendicular to the current flow. Moreover, during such simulations layers with ununiform grain sizes and doping density N_A could be introduced, as such variation is observed in SEM and KPFM measurements, and could have a significant impact on the electrical properties of a layer with both partially and fully depleted grains. Lastly, a model using diffusive transport across the GBs could be compared with the one presented here.

References

[1] M. Roser and E. Ortiz-Ospina, “Global Extreme Poverty,” https://ourworldindata.org/extreme-poverty#historical-poverty-around-the-world.

[2] “Price of EU carbon permits,” https://tradingeconomics.com/commodity/carbon.

[3] L. Cozzi and T. Gould, *World Energy Outlook 2021*., 2021.

[4] D.M. Chapin, C.S. Fuller, and G.L. Pearson, “A new silicon p-n junction photocell for converting solar radiation into electrical power.,” *Journal of Applied Physics*. vol. 25, no. 5, pp. 676–677, 1954.

[5] D.M. Chapin, C.S. Fuller, and G.L. Pearson, “Solar energy converting apparatus,” (1957).

[6] A. Sayigh, *Photovoltaics for sustainable electricity and buildings*., 2016.

[7] M. Tao, H. Hamada, T. Druffel, J.-J. Lee, and K. Rajeshwar, “Review—Research Needs for Photovoltaics in the 21st Century.,” *ECS Journal of Solid State Science and Technology*. vol. 9, no. 12, p. 125010, 2020.

[8] Lazard, *Lazards levelized cost of energy version 14.0 - October 2020*., 2020.

[9] *Photovoltaics Report*. , Freiburg, 2021.

[10] L.L. Kazmerski, F.R. White, and G.K. Morgan, “Thin-film CuInSe2/CdS heterojunction solar cells.,” *Applied Physics Letters*. vol. 29, no. 4, pp. 268–270, 1976.

[11] E.T. Efaz, M.M. Rhaman, S. Al Imam, et al., “A review of primary technologies of thin-film solar cells.,” *Engineering Research Express*. vol. 3, no. 3, p. 032001, 2021.

[12] S.-H. Wei and S.B. Zhang, “Defect properties of CuInSe2 and CuGaSe2.,” *Journal of Physics and Chemistry of Solids*. vol. 66, no. 11, pp. 1994–1999, 2005.

[13] S. Siebentritt, L. Gütay, D. Regesch, Y. Aida, and V. Deprédurand, “Why do we make Cu(In,Ga)Se2 solar cells non-stoichiometric?,” *Solar Energy Materials and Solar Cells*. vol. 119, pp. 18–25, 2013.

[14] U. Rau and H.W. Schock, “Electronic properties of Cu(In,Ga)Se2 heterojunction solar cells-recent achievements, current understanding, and future challenges.,” *Applied Physics A: Materials Science and Processing*. vol. 69, no. 2, pp. 131–147, 1999.

[15] A. Zunger, S.B. Zhang, and S.-H. Wei, “Revisiting the defect physics in CuInSe2 and CuGaSe2.,” *Conference Record of the IEEE Photovoltaic Specialists Conference*. no. i, pp. 313–318, 1997.

[16] J. Ramanujam and U.P. Singh, “Copper indium gallium selenide based solar cells - A review.,” *Energy and Environmental Science*. vol. 10, no. 6, pp. 1306–1319, 2017.

[17] W. Shockley and H.J. Queisser, “Detailed Balance Limit of Efficiency of p-n Junction Solar Cells.,” *Journal of Applied Physics*. vol. 32, no. 3, pp. 510–519, 1961.

[18] A. Al-Ashouri, A. Magomedov, M. Roß, et al., “Conformal monolayer contacts with lossless interfaces for perovskite single junction and monolithic tandem solar cells.,” *Energy and Environmental Science*. vol. 12, no. 11, pp. 3356–3369, 2019.

[19] N. Mufti, T. Amrillah, A. Taufiq, et al., “Review of CIGS-based solar cells manufacturing by structural engineering.,” *Solar Energy*. vol. 207, no. April, pp. 1146–1157, 2020.

[20] Zentrum für Sonnenenergie- und Wasserstoff-Forschung Baden-Württemberg, “Manufacture of CIGS thin-film solar cells,” https://www.zsw-bw.de/en/research/photovoltaics/topics/thin-film-solar-cells-and-modules.html#c460.

[21] V. Probst, J. Rimmasch, W. Riedl, et al., “The impact of controlled sodium incorporation on rapid thermal processed Cu(InGa)Se/sub 2/-thin films and devices.,” In: *Proceedings of 1994 IEEE 1st World Conference on Photovoltaic Energy Conversion - WCPEC (A Joint Conference of PVSC, PVSEC and PSEC)*. pp. 144–147. *IEEE* (1994).

[22] K. Granath, L. Stolt, and M. Bodegard, “Growth of Cu(In,Ga)Se2 thin films by coevaporation using alkaline precursors.,” *Thin Solid Films*. vol. 361–362, p. 9, 2000.

[23] I.L. Repins, S. Glynn, T.J. Silverman, et al., “Large metastability in Cu (In,Ga)Se2 devices: The importance of buffer properties.,” *Progress in Photovoltaics: Research and Applications*. vol. 27, no. 9, pp. 749–759, 2019.

[24] D.W. Niles, K. Ramanathan, F.S. Hasoon, R. Noufi, B.J. Tielsch, and J.E. Fulghum, “Na impurity chemistry in photovoltaic CIGS thin films: Investigation with x-ray photoelectron spectroscopy.,” *Journal of Vacuum Science & Technology A: Vacuum, Surfaces, and Films*. vol. 15, no. 6, pp. 3044–3049, 1997.

[25] S. Ishizuka, A. Yamada, K. Matsubara, P.J. Fons, K. Sakurai, and S. Niki, “Alkali incorporation control in Cu (In,Ga) Se2 thin films using silicate thin layers and applications in enhancing flexible solar cell efficiency.,” *Applied Physics Letters*. vol. 93, no. 12, pp. 1–4, 2008.

[26] S. Ishizuka and P.J. Fons, “Role of the Cu-Deficient Interface in Cu (In,Ga)Se2 Thin-Film Photovoltaics with Alkali-Metal Doping.,” *Physical Review Applied*. vol. 15, no. 5, p. 1, 2021.

[27] O. Cojocaru-Mirédin, M. Raghuwanshi, R. Wuerz, and S. Sadewasser, “Grain Boundaries in Cu(In, Ga)Se 2 : A Review of Composition–Electronic Property Relationships by Atom Probe Tomography and Correlative Microscopy.,” *Advanced Functional Materials*. vol. 31, no. 41, p. 2103119, 2021.

[28] T. Satoh, Y. Hashimoto, S. Shimakawa, and T. Negami, “Cu(In,Ga)Se2 Solar Cells on Flexible Stainless-Steel Foils.,” *Solid State Phenomena*. vol. 93, pp. 127–132, 2003.

[29] T. Satoh, Y. Hashimoto, S. Shimakawa, S. Hayashi, and T. Negami, “Cu(In,Ga)Se2 solar cells on stainless steel substrates covered with insulating layers.,” *Solar Energy Materials and Solar Cells*. vol. 75, no. 1–2, pp. 65–71, 2003.

[30] S. Khelifi, A. Belghachi, J. Lauwaert, et al., “Characterization of flexible thin film CIGSe solar cells grown on different metallic foil substrates.,” *Energy Procedia*. vol. 2, no. 1, pp. 109–117, 2010.

[31] J. Chantana, D. Hironiwa, T. Watanabe, S. Teraji, and T. Minemoto, “Physical properties of Cu(In,Ga)Se2 film on flexible stainless steel substrate for solar cell application: A multi-layer precursor method.,” *Solar Energy Materials and Solar Cells*. vol. 143, pp. 510–516, 2015.

[32] R. Caballero, C.A. Kaufmann, T. Eisenbarth, et al., “The effect of NaF precursors on low temperature growth of CIGS thin film solar cells on polyimide substrates.,” *Physica Status Solidi (A) Applications and Materials Science*. vol. 206, no. 5, pp. 1049–1053, 2009.

[33] R. Carron, S. Nishiwaki, T. Feurer, et al., “Advanced Alkali Treatments for High-Efficiency Cu(In,Ga)Se2 Solar Cells on Flexible Substrates.,” *Advanced Energy Materials*. vol. 9, no. 24, p. 2019.

[34] C.H. Huang, H.L. Cheng, W.E. Chang, M.Y. Huang, and Y.J. Chien, “Investigation of sputtered Mo layers on soda-lime glass substrates for CIGS solar cells.,” *Semiconductor Science and Technology*. vol. 27, no. 11, p. 2012.

[35] Z.H. Li, E.S. Cho, and S.J. Kwon, “Molybdenum thin film deposited by in-line DC magnetron sputtering as a back contact for Cu(In,Ga)Se 2 solar cells.,” *Applied Surface Science*. vol. 257, no. 22, pp. 9682–9688, 2011.

[36] F.H. Karg, “Development and manufacturing of CIS thin film solar modules.,” *Solar Energy Materials and Solar Cells*. vol. 66, no. 1–4, pp. 645–653, 2001.

[37] P. Reinhard, S. Buecheler, and A.N. Tiwari, “Technological status of Cu(In,Ga)(Se,S)2-based photovoltaics.,” *Solar Energy Materials and Solar Cells*. vol. 119, pp. 287–290, 2013.

[38] S. Niki, M.A. Contreras, I.L. Repins, et al., “CIGS absorbers and processes.,” *Progress in Photovoltaics: Research and Applications*. vol. 18, no. 6, pp. 453–466, 2010.

[39] K. Matsunaga, T. Komaru, Y. Nakayama, T. Kume, and Y. Suzuki, “Mass-production technology for CIGS modules.,” *Solar Energy Materials and Solar Cells*. vol. 93, no. 6–7, pp. 1134–1138, 2009.

[40] V.M. Fthenakis, “Overview of potential hazards.,” *McEvoy’s Handbook of Photovoltaics: Fundamentals and Applications*. pp. 1195–1212, 2018.

[41] R.A. Mickelsen and W.S. Chen, “High photocurrent polycrystalline thin-film CdS/CuInSe2 solar cell.,” *Applied Physics Letters*. vol. 36, no. 5, pp. 371–373, 1980.

[42] U. Rau and H.W. Schock, “Cu(In,Ga)Se2 solar cells.,” In: *Practical Handbook of Photovoltaics*. pp. 323–371. *Elsevier Ltd.* (2012).

[43] S.-H. Wei, S.B. Zhang, and A. Zunger, “Effects of Ga addition to CuInSe2 on its electronic, structural, and defect properties.,” *Applied Physics Letters*. vol. 72, no. 24, pp. 3199–3201, 1998.

[44] M. Powalla, D. Hariskos, E. Lotter, et al., “Large-area CIGS modules: Processes and properties.,” *Thin Solid Films*. vol. 431–432, no. 03, pp. 523–533, 2003.

[45] M. Powalla and B. Dimmler, “Development of large-area CIGS modules.,” *Solar Energy Materials and Solar Cells*. vol. 75, no. 1–2, pp. 27–34, 2003.

[46] F.A. Kröger and H.J. Vink, “Relations between the Concentrations of Imperfections in Crystalline Solids.,” Presented at the (1956).

[47] J. Yang, H.W. Du, Y. Li, et al., “Structural defects and recombination behavior of excited carriers in Cu(In,Ga)Se2 solar cells.,” *AIP Advances*. vol. 6, no. 8, p. 2016.

[48] L.E. Oikkonen, M.G. Ganchenkova, A.P. Seitsonen, and R.M. Nieminen, “Formation, migration, and clustering of point defects in CuInSe2 from first principles.,” *Journal of Physics Condensed Matter*. vol. 26, no. 34, p. 2014.

[49] C. Spindler, F. Babbe, M.H. Wolter, et al., “Electronic defects in Cu(In,Ga)Se2 : Towards a comprehensive model.,” *Physical Review Materials*. vol. 3, no. 9, p. 090302, 2019.

[50] C. Persson and A. Zunger, “Anomalous Grain Boundary Physics in Polycrystalline CuInSe2: The Existence of a Hole Barrier.,” *Physical Review Letters*. vol. 91, no. 26, p. 266401, 2003.

[51] W.K. Metzger and M. Gloeckler, “The impact of charged grain boundaries on thin-film solar cells and characterization.,” *Journal of Applied Physics*. vol. 98, no. 6, p. 2005.

[52] J. Kim, S. Kim, C.S. Jiang, K. Ramanathan, and M.M. Al-Jassim, “Direct imaging of enhanced current collection on grain boundaries of Cu(In,Ga)Se2 solar cells.,” *Applied Physics Letters*. vol. 104, no. 6, p. 2014.

[53] H. Yong, T. Minemoto, and T. Takahashi, “Photovoltage Decay Measurements by Photo-Assisted Kelvin Probe Force Microscopy on Cu(In,Ga)Se 2 Solar Cells.,” *IEEE Journal of Photovoltaics*. vol. 9, no. 2, pp. 483–491, 2019.

[54] M. Raghuwanshi, B. Thöner, P. Soni, M. Wuttig, R. Wuerz, and O. Cojocaru-Mirédin, “Evidence of Enhanced Carrier Collection in Cu(In,Ga)Se2 Grain Boundaries: Correlation with Microstructure.,” *ACS Applied Materials and Interfaces*. vol. 10, no. 17, pp. 14759–14766, 2018.

[55] H. Mirhosseini, J. Kiss, and C. Felser, “Behavior of σ3 Grain Boundaries in CuInSe2 and CuGaSe2 Photovoltaic Absorbers Revealed by First-Principles Hybrid Functional Calculations.,” *Physical Review Applied*. vol. 4, no. 6, pp. 1–6, 2015.

[56] M. Raghuwanshi, R. Wuerz, and O. Cojocaru-Mirédin, “Interconnection between Trait, Structure, and Composition of Grain Boundaries in Cu(In,Ga)Se 2 Thin-Film Solar Cells.,” *Advanced Functional Materials*. vol. 2001046, p. 2001046, 2020.

[57] Y. Yan, C.S. Jiang, R. Noufi, S.-H. Wei, H.R. Moutinho, and M.M. Al-Jassim, “Electrically benign behavior of grain boundaries in polycrystalline CuInSe2 films.,” *Physical Review Letters*. vol. 99, no. 23, pp. 2–5, 2007.

[58] C.-S. Jiang, R. Noufi, J.A.M. AbuShama, et al., “Local built-in potential on grain boundary of Cu(In,Ga)Se2 thin films.,” *Applied Physics Letters*. vol. 84, no. 18, pp. 3477–3479, 2004.

[59] C.S. Jiang, R. Noufi, K. Ramanathan, J.A.M. AbuShama, H.R. Moutinho, and M.M. Al-Jassim, “Does the local built-in potential on grain boundaries of Cu(In,Ga)Se 2 thin films

benefit photovoltaic performance of the device?," *Applied Physics Letters*. vol. 85, no. 13, pp. 2625–2627, 2004.

[60] U. Rau, K. Taretto, and S. Siebentritt, "Grain boundaries in Cu(In,Ga)(Se,S)2 thin-film solar cells.," *Applied Physics A: Materials Science and Processing*. vol. 96, no. 1, pp. 221–234, 2009.

[61] R. V. Forest, E. Eser, B.E. McCandless, J.G. Chen, and R.W. Birkmire, "Reversibility of (Ag,Cu)(In,Ga)Se2 electrical properties with the addition and removal of Na: Role of grain boundaries.," *Journal of Applied Physics*. vol. 117, no. 11, p. 2015.

[62] A. Urbaniak, M. Igalson, F. Pianezzi, et al., "Effects of Na incorporation on electrical properties of Cu(In,Ga)Se2-based photovoltaic devices on polyimide substrates.," *Solar Energy Materials and Solar Cells*. vol. 128, pp. 52–56, 2014.

[63] K. Taretto and U. Rau, "Numerical simulation of carrier collection and recombination at grain boundaries in Cu (In,Ga) Se2 solar cells.," *Journal of Applied Physics*. vol. 103, no. 9, p. 2008.

[64] M. Gloeckler, J.R. Sites, and W.K. Metzger, "Grain-boundary recombination in Cu (In,Ga) Se2 solar cells.," *Journal of Applied Physics*. vol. 98, no. 11, p. 2005.

[65] M. Igalson, "Photoconductivity of p-type CuInSe2.," *Physica Status Solidi (A) Applications and Materials Science*. vol. 139, no. 2, pp. 481–487, 1993.

[66] K. Macielak, M. Maciaszek, M. Igalson, P. Zabierowski, and N. Barreau, "Persistent photoconductivity in polycrystalline Cu(In,Ga)Se2 thin films: Experiment versus theoretical predictions.," *IEEE Journal of Photovoltaics*. vol. 5, no. 4, pp. 1206–1211, 2015.

[67] P. Zabierowski, U. Rau, and M. Igalson, "Classification of metastabilities in the electrical characteristics of ZnO/CdS/Cu(In,Ga)Se2 solar cells.," *Thin Solid Films*. vol. 387, no. 1–2, pp. 147–150, 2001.

[68] K. Macielak, M. Igalson, A. Urbaniak, P. Zabierowski, and N. Barreau, "Dependence of defect signature on conductivity of polycrystalline Cu(In,Ga)Se2 layers by photocurrent spectroscopy.," In: *2015 IEEE 42nd Photovoltaic Specialist Conference (PVSC)*. pp. 1–4. *IEEE* (2015).

[69] J.T. Heath, J.D. Cohen, and W.N. Shafarman, "Bulk and metastable defects in CuIn1-xGaxSe2 thin films using drive-level capacitance profiling.," *Journal of Applied Physics*. vol. 95, pp. 1000–1010, 2004.

[70] M. Maciaszek and P. Zabierowski, "Modeling of the magnitude of the persistent photoconductivity effect in Cu(In,Ga)Se2.," *Thin Solid Films*. vol. 633, pp. 45–48, 2017.

[71] A. Urbaniak and M. Igalson, "Creation and relaxation of light- and bias-induced metastabilities in Cu(In,Ga)Se2.," *Journal of Applied Physics*. vol. 106, no. 6, p. 063720, 2009.

[72] T. Meyer, M. Schmidt, F. Engelhardt, J. Parisi, and U. Rau, "Model for the open circuit voltage relaxation in Cu(In,Ga)Se2 heterojunction solar cells.," *EPJ Applied Physics*. vol. 8, no. 1, pp. 43–52, 1999.

[73] T.P. Weiss, F. Ehré, V. Serrano-Escalante, T. Wang, and S. Siebentritt, "Understanding Performance Limitations of Cu(In,Ga)Se 2 Solar Cells due to Metastable Defects—A Route toward Higher Efficiencies.," *Solar RRL*. vol. 5, no. 7, p. 2100063, 2021.

[74] T.P. Weiss, O. Ramírez, S. Paetel, et al., "Metastable Defects Decrease the Fill Factor of Solar Cells.," *Physical Review Applied*. vol. 19, no. 2, p. 024052, 2023.

[75] J.H. Schön and E. Bucher, "Persistent photoconductivity in n- and p-type CuGaSe 2.," *Journal of Physics D: Applied Physics*. vol. 34, no. 1, pp. 25–29, 2001.

[76] M. Igalson, M. Cwil, and M. Edoff, "Metastabilities in the electrical characteristics of CIGS devices: Experimental results vs theoretical predictions.," *Thin Solid Films*. vol. 515, no. 15, pp. 6142–6146, 2007.

[77] S. Chaisitsak, A. Yamada, and M. Konagai, "Comprehensive study of light-soaking effect in ZnO/Cu(InGa)Se2 solar cells with Zn-based buffer layers.," *Materials Research Society Symposium Proceedings*. vol. 668, pp. 1–6, 2001.

[78] K. Macielak, M. Igalson, and S. Spiering, “Comparison of metastabilities in CIGS solar cells with In2S3and CdS buffer layers.,” In: *2011 37th IEEE Photovoltaic Specialists Conference*. pp. 002763–002767. *IEEE* (2011).

[79] P.T. Erslev, J.W. Lee, W.N. Shafarman, and J.D. Cohen, “The influence of Na on metastable defect kinetics in CIGS materials.,” *Thin Solid Films*. vol. 517, no. 7, pp. 2277–2281, 2009.

[80] M. Maciaszek and P. Zabierowski, “On the magnitude of the persistent photoconductivity (PPC) effect in CIGS layers with and without sodium.,” *2015 IEEE 42nd Photovoltaic Specialist Conference, PVSC 2015*. pp. 15–17, 2015.

[81] P.T. Erslev, W.N. Shafarman, and J.D. Cohen, “Metastable properties of Cu(In1−xGax)Se2 with and without sodium.,” *Applied Physics Letters*. vol. 98, no. 6, p. 062105, 2011.

[82] D.E. Theodorou and H.J. Queisser, “Illumination-dose dependence of persistent photoconductivity of n-GaAs epitaxial layers.,” *Applied Physics*. vol. 23, no. 2, pp. 121–126, 1980.

[83] H.J. Queisser and D.E. Theodorou, “Hall-effect analysis of persistent photocurrents in n-GaAs layers.,” *Physical Review Letters*. vol. 43, no. 5, pp. 401–404, 1979.

[84] L. Chernyak, K. Gartsman, D. Cahen, and O.M. Stafsudd, “Electronic effects of ion mobility in semiconductors: Semionic behaviour of CuInSe2.,” *Journal of Physics and Chemistry of Solids*. vol. 56, no. 9, pp. 1165–1191, 1995.

[85] M. Burgelman, F. Engelhardt, J.F. Guillemoles, et al., “Defects in Cu(In, Ga) Se 2 semiconductors and their role in the device performance of thin-film solar cells.,” *Progress in Photovoltaics: Research and Applications*. vol. 5, no. 2, pp. 121–130, 1997.

[86] S. Lany and A. Zunger, “Anion vacancies as a source of persistent photoconductivity in II-VI and chalcopyrite semiconductors.,” *Physical Review B - Condensed Matter and Materials Physics*. vol. 72, p. 035215, 2005.

[87] S. Lany and A. Zunger, “Light- and bias-induced metastabilities in Cu(In,Ga)Se2 based solar cells caused by the (VSe-VCu) vacancy complex.,” *Journal of Applied Physics*. vol. 100, no. 11, p. 113725, 2006.

[88] M. Maciaszek and P. Zabierowski, “Quantitative analysis of the persistent photoconductivity effect in Cu(In,Ga)Se2.,” *Journal of Applied Physics*. vol. 123, no. 16, p. 2018.

[89] J. Hedström, H. Ohlsen, M. Bodegard, et al., “ZnO/CdS/Cu(In,Ga)Se thin film solar cells with improved performance.,” In: *Proceedings of the 23rd IEEE PVSC Conference* (1993).

[90] L. Stolt, J. Hedström, J. Kessler, M. Ruckh, K. Velthaus, and H. Schock, “ZnO/CdS/CuInSe 2 thin-film solar cells with improved performance.,” *Applied Physics Letters*. vol. 62, no. 6, pp. 597–599, 1993.

[91] G.M. Wilson, M.M. Al-Jassim, W.K. Metzger, et al., “The 2020 photovoltaic technologies roadmap.,” *Journal of Physics D: Applied Physics*. vol. 53, no. 49, p. 2020.

[92] P. Jackson, D. Hariskos, R. Wuerz, W. Wischmann, and M. Powalla, “Compositional investigation of potassium doped Cu(In,Ga)Se 2 solar cells with efficiencies up to 20.8%.,” *physica status solidi (RRL) - Rapid Research Letters*. vol. 8, no. 3, pp. 219–222, 2014.

[93] P. Jackson, R. Wuerz, D. Hariskos, E. Lotter, W. Witte, and M. Powalla, “Effects of heavy alkali elements in Cu(In,Ga)Se2 solar cells with efficiencies up to 22.6%.,” *Physica Status Solidi - Rapid Research Letters*. vol. 10, no. 8, pp. 583–586, 2016.

[94] NREL, *Best Research-Cell Efficiencies: Rev. 04-06-2020.*, 2020.

[95] P.M.P. Salomé, A. Hultqvist, V. Fjällström, et al., “Incorporation of Na in Cu(In,Ga)Se2 thin-film solar cells: A statistical comparison between Na from soda-lime glass and from a precursor layer of NaF.,” *IEEE Journal of Photovoltaics*. vol. 4, no. 6, pp. 1659–1664, 2014.

[96] M. Ruckh, D. Schmid, M. Kaiser, R. Schäffler, T. Walter, and H.W. Schock, “Influence

of substrates on the electrical properties of Cu(In,Ga)Se2 thin films.," *Solar Energy Materials and Solar Cells*. vol. 41–42, pp. 335–343, 1996.

[97] C.P. Muzzillo, S. Glynn, P. Hacke, et al., "Potential-Induced Degradation of Cu(In,Ga)Se2 Solar Cells: Alkali Metal Drift and Diffusion Effects.," *IEEE Journal of Photovoltaics*. vol. 8, no. 5, pp. 1337–1342, 2018.

[98] L.M. Mansfield, I.L. Repins, S. Glynn, et al., "Sodium-doped molybdenum targets for controllable sodium incorporation in CIGS solar cells.," In: *2011 37th IEEE Photovoltaic Specialists Conference*. pp. 003636–003641. *IEEE* (2011).

[99] A. Laemmle, R. Wuerz, and M. Powalla, "Efficiency enhancement of Cu(In,Ga)Se2 thin-film solar cells by a post-deposition treatment with potassium fluoride.," *Physica Status Solidi - Rapid Research Letters*. vol. 7, no. 9, pp. 631–634, 2013.

[100] L. Zhang, F.-F. Liu, F.-Y. Li, et al., "Developments of High-Efficiency Flexible Cu(In,Ga)Se 2 Thin Film Solar Cells on a Polyimide Sheet by Sodium Incorporation.," *Chinese Physics Letters*. vol. 31, no. 6, p. 068402, 2014.

[101] R. Caballero, C.A. Kaufmann, T. Eisenbarth, et al., "The influence of Na on low temperature growth of CIGS thin film solar cells on polyimide substrates.," *Thin Solid Films*. vol. 517, no. 7, pp. 2187–2190, 2009.

[102] J.H. Yun, K.H. Kim, M.S. Kim, et al., "Fabrication of CIGS solar cells with a Na-doped Molayer on a Na-free substrate.," *Thin Solid Films*. vol. 515, no. 15 SPEC. ISS., pp. 5876–5879, 2007.

[103] W.-J. Lee, D.-H. Cho, J.-H. Wi, W.S. Han, J. Kim, and Y.-D. Chung, "Na effect on flexible Cu(In,Ga)Se2 photovoltaic cell depending on diffusion barriers (SiOx, i-ZnO) on stainless steel.," *Materials Chemistry and Physics*. vol. 147, no. 3, pp. 783–787, 2014.

[104] D. Rudmann, G. Bilger, M. Kaelin, F.-J. Haug, H. Zogg, and A.N. Tiwari, "Effects of NaF coevaporation on structural properties of Cu(In,Ga)Se2 thin films.," *Thin Solid Films*. vol. 431–432, pp. 37–40, 2003.

[105] D. Rudmann, A.F. Da Cunha, M. Kaelin, et al., "Efficiency enhancement of Cu(In,Ga)Se2 solar cells due to post-deposition Na incorporation.," *Applied Physics Letters*. vol. 84, no. 7, pp. 1129–1131, 2004.

[106] D. Rudmann, D.J.L. Brémaud, H. Zogg, and A.N. Tiwari, "Na incorporation into Cu (In,Ga) Se2 for high-efficiency flexible solar cells on polymer foils.," *Journal of Applied Physics*. vol. 97, no. 8, pp. 10–15, 2005.

[107] F. Pianezzi, P. Reinhard, A. Chirilă, et al., "Unveiling the effects of post-deposition treatment with different alkaline elements on the electronic properties of CIGS thin film solar cells.," *Physical Chemistry Chemical Physics*. vol. 16, no. 19, pp. 8843–8851, 2014.

[108] P. Reinhard, B. Bissig, F. Pianezzi, et al., "Features of KF and NaF Postdeposition Treatments of Cu(In,Ga)Se2 Absorbers for High Efficiency Thin Film Solar Cells.," *Chemistry of Materials*. vol. 27, no. 16, pp. 5755–5764, 2015.

[109] H. Lee, Y. Jang, S.W. Nam, et al., "Passivation of Deep-Level Defects by Cesium Fluoride Post-Deposition Treatment for Improved Device Performance of Cu(In,Ga)Se2 Solar Cells.," *ACS Applied Materials and Interfaces*. vol. 11, no. 39, pp. 35653–35660, 2019.

[110] E. Avancini, R. Carron, T.P. Weiss, et al., "Effects of Rubidium Fluoride and Potassium Fluoride Postdeposition Treatments on Cu(In,Ga)Se2 Thin Films and Solar Cell Performance.," *Chemistry of Materials*. vol. 29, no. 22, pp. 9695–9704, 2017.

[111] H. Guthrey, J. Moseley, J. Nishinaga, H. Shibata, H. Takahashi, and M.M. Al-Jassim, "Spatially resolved recombination analysis of CuInxGa1-xSe2 absorbers with alkali postdeposition treatments.," *IEEE Journal of Photovoltaics*. vol. 8, no. 6, pp. 1833–1840, 2018.

[112] S. Ishizuka, A. Yamada, M.M. Islam, et al., "Na-induced variations in the structural, optical, and electrical properties of Cu (In,Ga) Se2 thin films.," *Journal of Applied Physics*. vol. 106, no. 3, p. 034908, 2009.

[113] C.K. Kim, S.H. Lee, J.H. In, H.J. Lee, and S. Jeong, "Depth profiling analysis of CuIn_1-xGa_xSe_2 absorber layer by laser induced breakdown spectroscopy in atmospheric conditions.," *Optics Express*. vol. 21, no. S6, p. A1018, 2013.

[114] P.-P. Choi, O. Cojocaru-Mirédin, R. Wuerz, and D. Raabe, "Comparative atom probe study of Cu(In,Ga)Se 2 thin-film solar cells deposited on soda-lime glass and mild steel substrates.," *Journal of Applied Physics*. vol. 110, p. 124513, 2011.

[115] P.M.P. Salomé, A. Hultqvist, V. Fjällström, et al., "Cu(In,Ga)Se2 Solar Cells With Varying Na Content Prepared on Nominally Alkali-Free Glass Substrates.," *IEEE Journal of Photovoltaics*. vol. 3, no. 2, pp. 852–858, 2013.

[116] B. Bissig, P. Reinhard, F. Pianezzi, et al., "Effects of NaF evaporation during low temperature Cu(In,Ga)Se2growth.," *Thin Solid Films*. vol. 582, pp. 56–59, 2015.

[117] R. Wuerz, A. Eicke, F. Kessler, S. Paetel, S. Efimenko, and C. Schlegel, "CIGS thin-film solar cells and modules on enamelled steel substrates.," *Solar Energy Materials and Solar Cells*. vol. 100, pp. 132–137, 2012.

[118] M. Theelen, N. Barreau, V. Hans, H. Steijvers, Z. Vroon, and M. Zeman, "Degradation of CIGS solar cells due to the migration of alkali-elements.," *2015 IEEE 42nd Photovoltaic Specialist Conference, PVSC 2015*. pp. 1–6, 2015.

[119] F. Couzinié-Devy, E. Cadel, N. Barreau, P. Pareige, and J. Kettle, "Atom probe contribution to the characterisation of CIGSe grain boundaries.," *Conference Record of the IEEE Photovoltaic Specialists Conference*. no. 1, pp. 001966–001971, 2011.

[120] K. Kim, J. Kim, M.G. Gang, et al., "A simple and robust route toward flexible CIGS photovoltaic devices on polymer substrates: Atomic level microstructural analysis and local opto-electronic investigation.," *Solar Energy Materials and Solar Cells*. vol. 195, no. November 2018, pp. 280–290, 2019.

[121] K. Kim, I. Jeong, Y. Cho, et al., "Mechanisms of extrinsic alkali incorporation in CIGS solar cells on flexible polyimide elucidated by nanoscale and quantitative analyses.," *Nano Energy*. vol. 67, no. October 2019, p. 104201, 2020.

[122] F. Couzinié-Devy, E. Cadel, N. Barreau, L. Arzel, and P. Pareige, "Na distribution in Cu(In,Ga)Se2 thin films: Investigation by atom probe tomography.," *Scripta Materialia*. vol. 104, pp. 83–86, 2015.

[123] E. Cadel, N. Barreau, J. Kettle, and P. Pareige, "Atom probe study of sodium distribution in polycrystalline Cu(In,Ga)Se2 thin film.," *Acta Materialia*. vol. 58, no. 7, pp. 2634–2637, 2010.

[124] Y.M. Shin, D.H. Shin, J.H. Kim, and B.T. Ahn, "Effect of Na doping using Na2S on the structure and photovoltaic properties of CIGS solar cells.," *Current Applied Physics*. vol. 11, no. 1 SUPPL., pp. S59–S64, 2011.

[125] O. Cojocaru-Mirédin, P. Choi, R. Wuerz, and D. Raabe, "Atomic-scale distribution of impurities in cuinse2-based thin-film solar cells.," *Ultramicroscopy*. vol. 111, no. 6, pp. 552–556, 2011.

[126] A. Czudek, A. Eslam, A. Urbaniak, P. Zabierowski, R. Wuerz, and M. Igalson, "Evolution of the electrical characteristics of Cu(In,Ga)Se 2 devices with sodium content.," *Journal of Applied Physics*. vol. 128, no. 17, p. 173102, 2020.

[127] A. Eslam, R. Wuerz, D. Hauschild, et al., "Impact of substrate temperature during NaF and KF post-deposition treatments on chemical and optoelectronic properties of alkali-free Cu(In,Ga)Se2 thin film solar cell absorbers.," *Thin Solid Films*. vol. 739, no. June, p. 138979, 2021.

[128] S. Ye, X. Tan, M. Jiang, B. Fan, K. Tang, and S. Zhuang, "Impact of different Na-incorporating methods on Cu(In,Ga)Se_2 thin film solar cells with a low-Na substrate.," *Applied Optics*. vol. 49, no. 9, p. 1662, 2010.

[129] S. Puttnins, S. Levcenco, K. Schwarzburg, et al., "Effect of sodium on material and device quality in low temperature deposited Cu(In,Ga)Se2.," *Solar Energy Materials and Solar Cells*. vol. 119, pp. 281–286, 2013.

[130] M.A. Contreras, B. Egaas, P. Dippo, et al., "On the role of Na and modifications to

Cu(In,Ga)Se2 absorber materials using thin-MF (M = Na, K, Cs) precursor layers.," *Conference Record of the IEEE Photovoltaic Specialists Conference*. vol. 96, pp. 359–362, 1997.

[131] A.A. Rockett, J.S. Britt, T. Gillespie, et al., "Na in selenized Cu(In,Ga)Se2 on Na-containing and Na-free glasses: Distribution, grain structure, and device performances.," *Thin Solid Films*. vol. 372, no. 1, pp. 212–217, 2000.

[132] Y. Kamikawa, J. Nishinaga, S. Ishizuka, et al., "Effect of thermal annealing on the redistribution of alkali metals in Cu(In,Ga)Se 2 solar cells on glass substrate.," *Journal of Applied Physics*. vol. 123, no. 9, p. 093101, 2018.

[133] S. Puttnins, M.S. Hammer, J. Neerken, et al., "Impact of sodium on the device characteristics of low temperature-deposited Cu(In,Ga)Se2-solar cells.," *Thin Solid Films*. vol. 582, pp. 85–90, 2015.

[134] P. Bommersbach, L. Arzel, M. Tomassini, et al., "Influence of Mo back contact porosity on co-evaporated Cu(In,Ga)Se2 thin film properties and related solar cell.," *Progress in Photovoltaics: Research and Applications*. vol. 21, pp. 332–343, 2013.

[135] A. Chirilă, P. Reinhard, F. Pianezzi, et al., "Potassium-induced surface modification of Cu(In,Ga)Se2 thin films for high-efficiency solar cells.," *Nature Materials*. vol. 12, no. 12, pp. 1107–1111, 2013.

[136] A. Stokes, M.M. Al-Jassim, D. Diercks, and B. Gorman, "Alkali segregation and matrix concentrations in thin film Cu(In,Ga)Se2 at targeted interfaces characterized in 3-D at the nanoscale.," *2015 IEEE 42nd Photovoltaic Specialist Conference, PVSC 2015*. pp. 1–4, 2015.

[137] S. Karki, P.K. Paul, G. Rajan, et al., "In situ and ex situ investigations of KF postdeposition treatment effects on CIGS solar cells.," *IEEE Journal of Photovoltaics*. vol. 7, no. 2, pp. 665–669, 2017.

[138] C.-H. Hsu, W.H. Ho, S.-Y. Wei, and C.H. Lai, "Over 14% Efficiency of Directly Sputtered Cu(In,Ga)Se2 Absorbers without Postselenization by Post-Treatment of Alkali Metals.," *Advanced Energy Materials*. vol. 7, no. 13, p. 1602571, 2017.

[139] J.M. Raguse, C.P. Muzzillo, J.R. Sites, and L.M. Mansfield, "Effects of Sodium and Potassium on the Photovoltaic Performance of CIGS Solar Cells.," *IEEE Journal of Photovoltaics*. vol. 7, no. 1, pp. 303–306, 2017.

[140] A. Laemmle, R. Wuerz, and M. Powalla, "Investigation of the effect of potassium on Cu(In,Ga)Se2layers and solar cells.," *Thin Solid Films*. vol. 582, pp. 27–30, 2015.

[141] S.-H. Wei, S.B. Zhang, and A. Zunger, "Effects of Na on the electrical and structural properties of CuInSe2.," *Journal of Applied Physics*. vol. 85, no. 10, pp. 7214–7218, 1999.

[142] Z.K. Yuan, S. Chen, Y. Xie, et al., "Na-Diffusion Enhanced p-type Conductivity in Cu(In,Ga)Se2: A New Mechanism for Efficient Doping in Semiconductors.," *Advanced Energy Materials*. p. 1601191, 2016.

[143] L.E. Oikkonen, M.G. Ganchenkova, A.P. Seitsonen, and R.M. Nieminen, "Effect of sodium incorporation into CuInSe2 from first principles.," *Journal of Applied Physics*. vol. 114, no. 8, p. 2013.

[144] R. Saniz, J. Bekaert, B. Partoens, and D. Lamoen, "Structural and electronic properties of defects at grain boundaries in CuInSe2.," *Physical Chemistry Chemical Physics*. vol. 19, no. 22, pp. 14770–14780, 2017.

[145] L. Kronik, D. Cahen, and H.W. Schock, "Effects of Sodium on Polycrystalline Cu(In,Ga)Se2 and Its Solar Cell Performance.," *Advanced Materials*. vol. 10, no. 1, pp. 31–36, 1998.

[146] L. Kronik, U. Rau, J.F. Guillemoles, D. Braunger, H.W. Schock, and D. Cahen, "Interface redox engineering of Cu(In,Ga)Se2-based solar cells: Oxygen, sodium, and chemical bath effects.," *Thin Solid Films*. vol. 361, pp. 353–359, 2000.

[147] X. Lyu, D. Zhuang, M. Zhao, et al., "An investigation on performance enhancement for KF post deposition treated CIGS solar cells fabricated by sputtering CIGS quaternary

targets.," *Vacuum*. vol. 151, pp. 233–236, 2018.

[148] E. Handick, P. Reinhard, R.G. Wilks, et al., "NaF/KF post-deposition treatments and their influence on the structure of Cu(In,Ga)Se2 absorber surfaces.," In: *2016 IEEE 43rd Photovoltaic Specialists Conference (PVSC)*. pp. 0017–0021. *IEEE* (2016).

[149] E. Handick, P. Reinhard, J.H. Alsmeier, et al., "Potassium Postdeposition Treatment-Induced Band Gap Widening at Cu(In,Ga)Se2 Surfaces - Reason for Performance Leap?," *ACS Applied Materials and Interfaces*. vol. 7, no. 49, pp. 27414–27420, 2015.

[150] J.A. Aguiar, A. Stokes, C.-S. Jiang, et al., "Revealing Surface Modifications of Potassium-Fluoride-Treated Cu(In,Ga)Se 2 : A Study of Material Structure, Chemistry, and Photovoltaic Performance.," *Advanced Materials Interfaces*. vol. 3, no. 17, p. 1600013, 2016.

[151] H. Ibach and H. Lüth, *Solid-State Physics*. *Springer Berlin Heidelberg*, Berlin, Heidelberg, 2009.

[152] M. Grundmann, *The Physics of Semiconductors*. *Springer Berlin Heidelberg*, Berlin, Heidelberg, 2010.

[153] K.W. Böer and U.W. Pohl, *Semiconductor Physics*. *Springer International Publishing*, Cham, 2018.

[154] J.Y.W. Seto, "The electrical properties of polycrystalline silicon films.," *Journal of Applied Physics*. vol. 46, no. 12, pp. 5247–5254, 1975.

[155] C.E. Michelson, A. V. Gelatos, and J.D. Cohen, "Drive-level capacitance profiling: Its application to determining gap state densities in hydrogenated amorphous silicon films.," *Applied Physics Letters*. vol. 47, no. 4, pp. 412–414, 1985.

[156] M. Cwil, M. Igalson, P. Zabierowski, and S. Siebentritt, "Charge and doping distributions by capacitance profiling in Cu(In,Ga)Se2 solar cells.," *Journal of Applied Physics*. vol. 103, no. 6, p. 063701, 2008.

[157] *HP 4284A Precision LCR Meter Operation Manual*., 1996.

[158] A. Urbaniak, M. Igalson, N. Barreau, and M. Tomassini, "Capacitance spectroscopy of Cu(In,Ga)Se2-based solar cells with a Pt back electrode.," *Thin Solid Films*. vol. 574, pp. 120–124, 2015.

[159] R. Farshchi, B. Hickey, G. Zapalac, J. Bailey, D. Spaulding, and D. Poplavskyy, "Mechanisms for light-soaking induced carrier concentration changes in the absorber layer of Cu(In, Ga)Se2 solar cells.," *Conference Record of the IEEE Photovoltaic Specialists Conference*. vol. 2016-Novem, pp. 2157–2160, 2016.

[160] S.A. Dinca, E.A. Schiff, B. Egaas, R. Noufi, D.L. Young, and W.N. Shafarman, "Hole drift mobility measurements in polycrystalline CuIn1-xGaxSe2.," *Physical Review B - Condensed Matter and Materials Physics*. vol. 80, no. 23, p. 235201, 2009.

[161] F. Werner, T. Bertram, J. Mengozzi, and S. Siebentritt, "What is the dopant concentration in polycrystalline thin-film Cu(In,Ga)Se 2 ?," *Thin Solid Films*. vol. 633, pp. 222–226, 2017.

[162] G. Baccarani, B. Riccò, and G. Spadini, "Transport properties of polycrystalline silicon films.," *Journal of Applied Physics*. vol. 49, no. 11, pp. 5565–5570, 1978.

[163] A. Niemegeers, M. Burgelman, K. Decock, S. Degrave, and J. Verschraegen, "Simulation programme SCAPS-1D for thin film solar cells developed at ELIS, University of Gent," https://scaps.elis.ugent.be/.

[164] O. Cojocaru-Mirédin, T. Schwarz, and D. Abou-Ras, "Assessment of elemental distributions at line and planar defects in Cu(In,Ga)Se2 thin films by atom probe tomography.," *Scripta Materialia*. vol. 148, pp. 106–114, 2018.

[165] D.M. Kim, A.N. Khondker, and S.S. Ahmed, "Theory of Conduction in Polysilicon: Drift-Diffusion Approach in Crystalline-Amorphous-Crystalline Semiconductor System--Part I: Small Signal Theory.," *IEEE Transactions on Electron Devices*. vol. 31, no. 4, pp. 480–493, 1984.

[166] K. Wiśniewski and P. Zabierowski, "Diffusion transport over grain-boundary barriers as

the origin of N1 deep level transient spectroscopy signal in Cu(In,Ga)Se2 solar cells.," *Thin Solid Films*. vol. 721, no. May 2020, p. 138540, 2021.

[167] J. Salzman, C. Uzan-Saguy, B. Meyler, and R. Kalish, "Effect of grain boundaries on electrical conductivity in thin GaN layers.," *Physica Status Solidi (A) Applied Research*. vol. 176, no. 1, pp. 683–687, 1999.

[168] R. V. Forest, B.E. McCandless, X. He, et al., "Diffusion of sodium in single crystal CuInSe 2.," *Journal of Applied Physics*. vol. 121, no. 24, p. 2017.

[169] C.P. Muzzillo, "Review of grain interior, grain boundary, and interface effects of K in CIGS solar cells: Mechanisms for performance enhancement.," *Solar Energy Materials and Solar Cells*. vol. 172, pp. 18–24, 2017.

[170] H. Aboulfadl, K. V. Sopiha, J. Keller, et al., "Alkali Dispersion in (Ag,Cu)(In,Ga)Se 2 Thin Film Solar Cells—Insight from Theory and Experiment.," *ACS Applied Materials & Interfaces*. p. 2021.

[171] M. Tsuyoshi, K. Atsuhito, and W. Takahiro, "First-principles study on alkali-metal effect of Li, Na, and K in CuInSe 2 and CuGaSe 2.," *Japanese Journal of Applied Physics*. vol. 54, no. 8S1, p. 08KC20, 2015.

[172] H. Guthrey, A. Norman, J. Nishinaga, S. Niki, and M.M. Al-Jassim, "Optical and Structural Properties of High-E ffi ciency Epitaxial Cu (In , Ga) Se 2 Grown on GaAs.," *ACS Applied Materials & Interfaces*. vol. 12, pp. 3150–3160, 2019.

[173] I. Visoly-Fisher, S.R. Cohen, A. Ruzin, and D. Cahen, "How polycrystalline devices can outperform single-crystal ones: Thin film CdTe/CdS solar cells.," *Advanced Materials*. vol. 16, no. 11, pp. 879–883, 2004.

[174] J. Dietrich, D. Abou-Ras, S.S. Schmidt, et al., "Origins of electrostatic potential wells at dislocations in polycrystalline Cu(In,Ga)Se2 thin films.," *Journal of Applied Physics*. vol. 115, no. 10, p. 2014.

[175] D. Keller, S. Buecheler, P. Reinhard, et al., "Band gap widening at random CIGS grain boundary detected by valence electron energy loss spectroscopy.," *Applied Physics Letters*. vol. 109, no. 15, p. 2016.

[176] A. Stokes, M. Al-Jassim, D. DIercks, A. Clarke, and B. Gorman, "Impact of Wide-Ranging Nanoscale Chemistry on Band Structure at Cu(In, Ga)Se2 Grain Boundaries.," *Scientific Reports*. vol. 7, no. 1, pp. 1–11, 2017.

[177] M.Y. Kim, G. Kim, J. Kim, J.H. Park, and D. Lim, "Structural and electrical properties of co-evaporated Cu(In,Ga)Se 2 thin films with varied Cu contents.," *Thin Solid Films*. vol. 546, pp. 308–311, 2013.

[178] A. Kumar and P. Ranjan, "Impact of light soaking on absorber and buffer layer in thin film solar cells.," *Applied Physics A: Materials Science and Processing*. vol. 126, no. 6, pp. 1–8, 2020.

List of Publications and Projects

Publications

Book chapters

2020 E. Unger, A. Czudek, H-S Kim, W. Tress „*Current-voltage analysis: lessons learned from hysteresis*" in „Characterization Techniques for Perovskite Solar Cell Materials" editors: M. Pazoki, T. Hagfeldt, T. Edvinsson, 2020 Elsevier

Journal papers

2023 A. Urbaniak, A. Czudek, A. Eslam, R. Wuerz, M. Igalson, "*Consequences of grain boundary barriers on electrical characteristics of CIGS solar cells*" Solar Energy Materials and Solar Cells, 253, 112252 (2023)

2022 M. Igalson, A. Czudek "*Electrical spectroscopy methods for the characterization of defects in thin-film compound solar cells*" Journal of Applied Physics, 131, 240901 (2022)

2022 A. Urbaniak, A. Czudek, J. Dagar, E. L. Unger, "*Capacitance spectroscopy of thin-film formamidinium lead iodide based perovskite solar cells*" Solar Energy Materials & Solar Cells 238, 111618, (2022)

2022 A. Czudek, A. Urbaniak, A. Eslam, R. Wuerz, M. Igalson, "*Potassium vs sodium in Cu(In,Ga)Se_2 – similarities and differences in the electrical characteristics of solar cells and thin films after NaF or KF post-deposition treatment*" Physica Status Solidi Rapid Research Letters, 16, 2100459 (2022)

2020 A. Czudek, A. Eslam, A. Urbaniak, P. Zabierowski, R. Wuerz, M. Igalson „*Evolution of the electrical characteristics of Cu(In,Ga)Se_2 devices with sodium content*" Journal of Applied Physics 128, 173102 (2020)

2020 A. Czudek, A. Urbaniak, A. Eslam, R. Wuerz, M. Igalson, "*Dependence of the Magnitude of Persistent Photoconductivity on Sodium Content in Cu(In,Ga)Se_2 Solar Cells and Thin Films*," IEEE Journal of Photovoltaics, vol. 10, no. 6, pp. 1926-1930, (2020)

2019 M. Igalson, M. Maciaszek, K. Macielak, A. Czudek, M. Edoff, N. Barreau: „*Concentration of defects responsible for persistent photoconductivity in Cu(In,Ga)Se_2: Dependence on material composition*." Thin Solid Films 669, 600 (2019)

2019 J. Dagar, K. Hirselandt, A. Merdasa, A. Czudek, R. Munir, F. Zu, N. Koch, T. Dittrich, E.L. Unger, „*Alkali Salts as Interface Modifiers in n-i-p Hybrid Perovskite Solar Cells*." Solar RRL, 3: 1900088, (2019)

Disseminations

Oral presentations

2023 A. Czudek, A. Urbaniak, A. Eslam, R. Wuerz, M. Igalson, "*Influence of Alkali Doping on the Grain Boundaries in CIGS Studied by Electrical and Capacitive Methods*", Materials Research Society Spring Meeting, San Francisco, USA, April 2023

2020 A. Czudek, A. Urbaniak, A. Eslam, R. Wuerz, M. Igalson, *Influence of sodium concentration on the magnitude of persistent photoconductivity in Cu(In,Ga)Se_2 solar cells*, 1st Virtual Chalcogenide PV Conference (replacement for EMRS Spring Meeting), online, May 2020

2018 A. Czudek, K. Hirselandt, L. Kegelmann, A. Al Ashouri, S. Albrecht, E. Unger, *Dynamic maximum power point tracking algorithm as a mean for quantitative comparison of lead-halide perovskite solar cells*, European Materials Research Society Fall Meeting, Warsaw, Poland, September 2018

Poster presentations

2021 A. Czudek, A. Urbaniak, P. Zabierowski, A. Eslam, R. Wuerz, M. Igalson, *Impact of alkali metals on persistent photoconductivity in Cu(In,Ga)Se_2*, European Materials Research Society Spring Meeting 2021, online

2019 A. Czudek, M. Igalson, A. Urbaniak, R. Wurz, *Persistent photoconductivity vs sodium content in Cu(In,Ga)Se_2 thin films*, 48th International School & Conference on the Physics of Semiconductors "Jaszowiec 2019", Szczyrk, Poland, June 2019

2018 A. Czudek, L. Kegelmann, A. Al.-Ashouri, S. Albrecht, E. Unger, *Measurement development for hysteresis characterization of perovskite solar cells*, DPG-Frühjahrstagung und EPS-CMD27, Berlin, Germany, March 2018

2017 A. Czudek, L. Kegelmann, M. Jost, K. Hirselandt, P. Tockhorn, E. Unger, *Quantifying hysteresis: developing tools to characterize the transient response of metal halide perovskite devices on different time scales*., Solar Energy in Israel, Rehovot, Israel, October.2017

Involvement in projects

2020-2022 Contractor, WUT POB Energy Tech "*Defekty w perowskitowych ogniwach słonecznych*"

2020-2023 Contractor, WUT POB Energy Tech "*Migracja jonów w cienkowarstwowych ogniwach słonecznych*"

2018-2022 Contractor, Beethoven II project - "AlkaCIGS" (NCN, DFG) in collaboration with Zentrum für Sonnenenergie- und Wasserstoff-Forschung Baden-Württemberg (ZSW), "*Effects of alkali elements in Cu(In,Ga)Se2 thin films and solar cells*"

List of Figures

List of Tables

List of Abbreviations and Symbols

AFM	atomic force microscopy
Alk_{eff}^{GB}	effective alkali concentration at the grain boundary
APT	atom probe tomography
AR	anti-reflection (coating)
BSG	borosilicate glass
C	capacitance
c(x)	concentration of element x
CB	conduction band
CBD	chemical bath deposition
CBM	conduction band minimum
CGI	Copper to gallium and indium ratio, CGI=[Cu]/([Ga]+[In])
CGS	$CuGaSe_2$
CIGS	$Cu(In,Ga)Se_2$
CIS	$CuInSe_2$
CV	capacitance-voltage measurement
d_{In-In}	distance between two In atoms in the Lany-Zunger model
D_p, D_n	diffusion coefficient of free holes / free electrons
DLCP	drive-level capacitance profiling
DOS	density of states
e	electron charge
EBIC	electron beam induced current
E_A	activation energy
E_B	barrier height at the grain boundary
E_C	conduction band edge energy
E_d	defect/dopant level energy
E_F	Fermi energy
E_g	bandgap energy
E_{sub}	substitution energy needed to replace In_{Cu} with Na_{Cu} (arbitrary)
E_t	energy of a donor defect state/trap at the grain boundary
E_V	valence band edge energy
f_A	proportion of the acceptor configuration of the (V_{Se}-V_{Cu}) in the relaxed state

FF	fill factor
G1, G2	grain 1, grain 2
GB	grain boundary
GGI	gallium to gallium and indium ratio, $GGI = [Ga]/([Ga] + [In])$
GI	grain interior
h	hole
i	interstitial
J_{mpp}	current density at maximum power point
J_{SC}	short-circuit current density
JV	current-voltage
k_B	Boltzmann constant
L	grain size dimension in 1D
LS	light-soaking
MPP	maximum power point
n	concentration of free electrons
N_A	concentration of acceptors
N_D	concentration of donors
N_{DL}	concentration of charge carriers obtained from DLCP
N_M	concentration of metastable defects / defect pairs
p	concentration of free holes
PDT	post-deposition treatment
p_{LS}	free hole concentration in the metastable state
Δp_{PPC}	metastable increase in hole concentration, $\Delta p_{PPC} = p_{LS} - p_R$
PPC	persistent photoconductivity
ppm	particles per million
p_R	free hole concentration in the relaxed state
q	(carrier) charge
Q_t	surface concentration of donors at the grain boundary [cm^{-2}]
RF	radio frequency
RHAGB	random high-angle grain boundary
S_{grain}	surface area of a grain
SCR	space-charge region
SIMS	Secondary Ion Mass Spectrometry

SLG	soda-lime glass
SQ	Shockley-Queisser (limit)
TCO	transparent conductive oxide
V	vacancy
V_{grain}	volume of a single grain
VB	valence band
VBM	valence band maximum
V_{mpp}	maximum power point voltage
V_{OC}	open-circuit voltage
W	space-charge region width
XRF	X-ray Fluorescence Spectrometry
ε_0	dielectric permittivity of vacuum
ε_R	relative dielectric permittivity
ε	defect transition energy
η	solar cell efficiency
μ	mobility
ξ	parameter, 1 for sodium, 0.25 for potassium
σ	conductivity
σ_{LS}	conductivity in the metastable state
$\Delta\sigma_{PPC}$	metastable increase in conductivity, $\Delta\sigma_{PPC} = \sigma_{LS} - \sigma_R$
σ_R	conductivity in the relaxed state
τ_p, τ_n	lifetime of free holes / free electrons

Appendices

Appendix 1 SCAPS parameters used to simulate grain boundary barriers

CIGS bulk	
E_g	1.2 eV
μ_e	100 cm^2/Vs
μ_h	50 cm^2/Vs
ε_R	10
N_c	$2 \cdot 10^{18}\ cm^{-3}$
N_v	$2 \cdot 10^{19}\ cm^{-3}$
T	200 K
Grain size	250 / 350 nm
N_A	$1.8 \cdot 10^{16}\ cm^{-3}$

Interface	
Defect type	donor
E_c-E_t	0.35 eV
σ_e	$10^{-13}\ cm^2$
σ_h	$10^{-13}\ cm^2$
Distribution	Gauss
Char. Energy	0.05 eV
Q_t	varied

Table A1. SCAPS parameters used for the simulation of thin films. Values that were not explicitly calculated in this work were taken from [51, 178]

Simulations of the impact of charged defects at the grain boundaries were performed in SCAPS, 1-dimensional simulation software [163]. In Table A1, parameters used in the simulations are presented. The doping density, $N_A=1.8\cdot10^{16}\ cm^{-3}$, calculated from the highest barrier height, is slightly above the highest relaxed free hole concentration measured in this work, but stays withing the range typically used in simulations, ranging between $0.75\cdot10^{16}\ cm^{-3}$ and $3\cdot10^{16}\ cm^{-3}$. Hole mobility within the grain bulk was set to be 50 cm^2/Vs, which is a value estimated by dividing the highest obtained conductivity and free hole concentration, and if higher than the literature results on polycrystalline films, but it still considerably lower than the values measured on single crystals in literature, about 100-500 cm^2/Vs. As the grain size, the width in the horizontal direction was taken – 250nm for the single-stage and 350nm for the three-stage CIGS.

As the three-stage process involves both Cu-poor and Cu-rich phases, and may not result in a uniform Cu distribution (resulting in different doping density, mobility and defect concentrations in lateral direction of the film), the simulations might be less accurate.

Appendix 2 JV characteristics used for the $V_{OC}(T)$ plot

IV(T) measurements used to determine the $V_{OC}(T)$ relation were performed on 50mm^2 solar cells in a nitrogen cryostat using a two-point probe method in vacuum, with temperature ranging between 80K and 330K in 10K increments. The measurement setup consisted of a custom-made voltammeter and a LakeShore temperature controller. As a light source, a white LED was used. To achieve an illumination intensity of AM1.5g the light intensity was adjusted so that resulting J_{SC} would be equal to that measured on each cell at ZSW under STC. The measurement protocol was as follows: after each temperature step, a dark IV curve was measured, followed by a series of IVs with illumination intensity increasing from 10 to 100% in 10%-point increments.

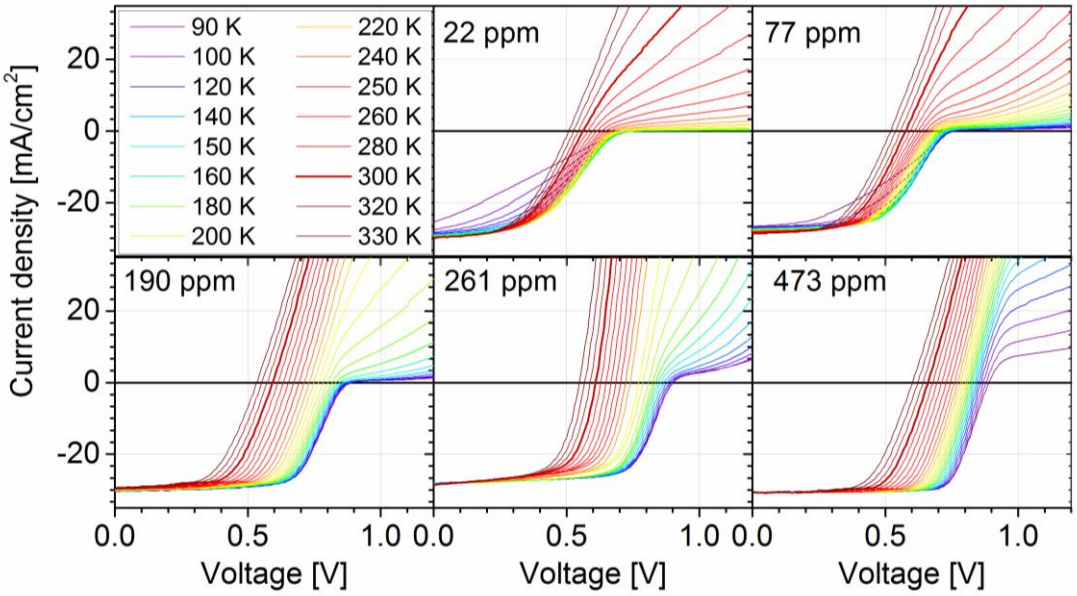

Figure A2 Current-voltage measurements taken as a function of temperature of solar cells from the SLG/SiO_xNy-1st.-NaF series illuminated with white LED diode with intensity corresponding to AM1.5g. As the setup is not very precise, for the exact values of J_{SC} and V_{OC} at STC please refer to the parameters listed in Chapter 8.2. IV measurements taken at 300K were emphasized with a thicker line.

The alkali-free device at low temperatures exhibits very poor fill factor, characterized by an almost linear IV dependence in the 0V-V_{OC} range. This behavior persists in the low-Na device (77ppm), although less pronounced and resolved at lower temperatures than in case of the alkali-free cell. Another fingerprint of the alkali-free CIGS cells is the double-diode behavior, where a barrier is visible above the V_{OC}. This can be seen as the almost horizontal part of the IV curve above V_{OC}. For the alkali-free cell it can be seen up to about 250K until the barrier starts to get reduced and the IV dependence becomes gradually more typical. Upon addition of sodium, the curves lift up faster – around 180K for 77ppm and 120K for 190ppm. This behavior continues with the further addition of sodium and the IV characteristics becoming more and more similar to a normal, single-diode dependence.